

NO-A191 274

LASER CLADDING OF NI NB AND MG ALLOYS FOR IMPROVED
ENVIRONMENTAL RESISTAN. (U) ILLINOIS UNIV AT URBANA
LASER AIDED MATERIALS PROCESSING LAB. J HAZUNDER

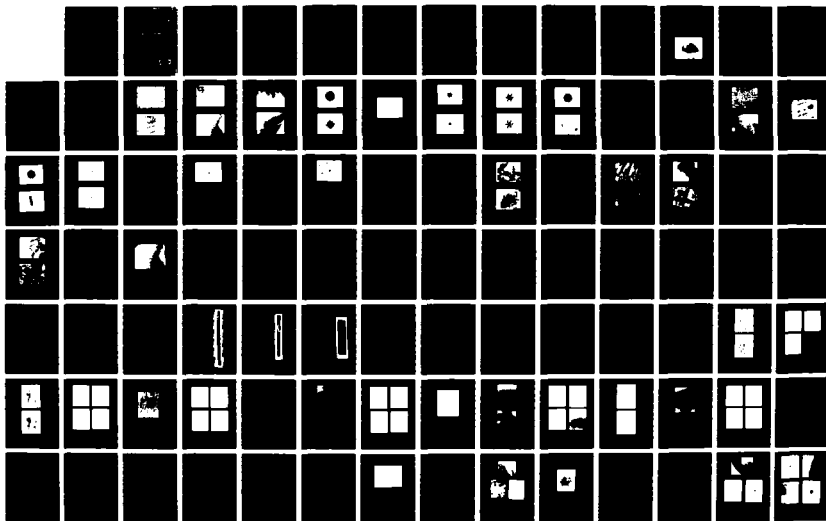
1/3

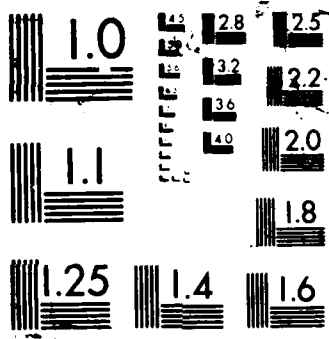
UNCLASSIFIED

OCT 07 AFOSR-TR-87-1856 AFOSR-85-8333

F/G 11/6.1

NL





29

AD-A191 274

Laser Aided Materials Processing Laboratory
Department of Mechanical and Industrial Engineering
University of Illinois at Urbana-Champaign
Urbana, IL 61801



DTIC FILE COPY

Annual Progress Report
(November 1986 through October 1987)

LASER CLADDING OF Ni, Nb, AND Mg ALLOYS FOR IMPROVED ENVIRONMENTAL RESISTANCE AT HIGH TEMPERATURE

Approved for public release;
distribution unlimited.

Contract No. AFOSR 85-0333
submitted to
Air Force Office of Scientific Research
Building 410
ATTN: Dr. A. Rosenstein
Bolling Air Force Base
Washington, DC 20332

submitted by

J. MAZUMDER, A. KAR, S. SIRCAR,
C. RIBAUDO, AND R. SUBRAMANIAN

AIR FORCE OFFICE OF SCIENTIFIC RESEARCH (AFOSR)
NOTICE OF TRANSMITTAL TO DTIC
This technical report has been reviewed and is approved for public release (AW AFR 190-12).
DISTRIBUTION IS UNLIMITED.
MATTHEW J. KERPER
Chief, Technical Information Division

DTIC ELECTE
S JAN 11 1988 D
E

UNCLASSIFIED

SECURITY CLASSIFICATION OF THIS PAGE

A191 274

REPORT DOCUMENTATION PAGE

1a. REPORT SECURITY CLASSIFICATION UNCLASSIFIED		1b. RESTRICTIVE MARKINGS	
2a. SECURITY CLASSIFICATION AUTHORITY		3. DISTRIBUTION/AVAILABILITY OF REPORT Approved for public release; distribution unlimited.	
2b. DECLASSIFICATION/DOWNGRADING SCHEDULE		4. PERFORMING ORGANIZATION REPORT NUMBER(S)	
4. PERFORMING ORGANIZATION REPORT NUMBER(S)		5. MONITORING ORGANIZATION REPORT NUMBER(S) AFOSR-TR- 87-1856	
6a. NAME OF PERFORMING ORGANIZATION University of Illinois	6b. OFFICE SYMBOL (If applicable)	7a. NAME OF MONITORING ORGANIZATION AFOSR/NE	
6c. ADDRESS (City, State and ZIP Code) Urbana-Champaign Urbana, IL 61801		7b. ADDRESS (City, State and ZIP Code) Bldg 410 Bolling AFB, DC 20332-6448	
8a. NAME OF FUNDING/SPONSORING ORGANIZATION Same as 7a	8b. OFFICE SYMBOL (If applicable) NE	9. PROCUREMENT INSTRUMENT IDENTIFICATION NUMBER AFOSR-85-0333	
8c. ADDRESS (City, State and ZIP Code) Same as 7b		10. SOURCE OF FUNDING NOS.	
		PROGRAM ELEMENT NO. 61102F	PROJECT NO. 2306
		TASK NO. A2	WORK UNIT NO.
11. TITLE (Include Security Classification) Laser Cladding of Ni, Nb and Mg Alloys for improved environmental resistance at High Temperatures			
12. PERSONAL AUTHOR(S) J. Mazumder			
13a. TYPE OF REPORT Annual	13b. TIME COVERED FROM Nov 86 TO Oct 87	14. DATE OF REPORT (Yr., Mo., Day) 1987 OCT	15. PAGE COUNT 201
16. SUPPLEMENTARY NOTATION			
17. COSATI CODES		18. SUBJECT TERMS (Continue on reverse if necessary and identify by block number)	
FIELD	GROUP	SUB. GR.	
19. ABSTRACT (Continue on reverse if necessary and identify by block number) This report summarizes experimental and theoretical studies carried out during the period of Nov 1986 to Oct 1987 on laser cladding of Ni and Nb alloys for improved environmental resistance at high temperature. Major emphasis has been on Ni-Cr-Al-Hf system. Micro-structural evolution and oxidation properties of these alloys were examined. For Nb alloys microstructural characterization and differential thermal analysis were carried out. One-dimensional diffusion model for finite domain to examine the extended solid solubility in laser cladding was also developed. (Nickel, Chromium, Aluminum, Hafnium)			
20. DISTRIBUTION/AVAILABILITY OF ABSTRACT UNCLASSIFIED/UNLIMITED <input checked="" type="checkbox"/> SAME AS RPT. <input type="checkbox"/> DTIC USERS <input type="checkbox"/>		21. ABSTRACT SECURITY CLASSIFICATION UNCLASSIFIED	
22a. NAME OF RESPONSIBLE INDIVIDUAL Dr Alan Rosenstein		22b. TELEPHONE NUMBER (Include Area Code) 202/767-4933	22c. OFFICE SYMBOL NE

ANNUAL PROGRESS REPORT

(November 1986 through October 1987)

LASER CLADDING OF Ni, Nb, AND Mg ALLOYS FOR IMPROVED
ENVIRONMENTAL RESISTANCE AT HIGH TEMPERATURE

Contract No. AFOSR 85-0333

Submitted to

Air Force Office of Scientific Research
Building 410
Attn. Dr. A. Rosenstein
Bolling Air Force Base
Washington, DC 20332

J. Mazumder, Principal Investigator
A. Kar and S. Sircar, Research Associates
Carl Ribaud, and R. Subramanian, Graduate Research Assistants
Department of Mechanical and Industrial Engineering
University of Illinois at Urbana-Champaign
1206 West Green Street
Urbana, IL 61801



Accession For	
NTIS CRA&I	<input checked="" type="checkbox"/>
DTIC TAB	<input type="checkbox"/>
Unannounced	<input type="checkbox"/>
Justification	
By	
Distribution	
Availability Codes	
Date	
A-1	

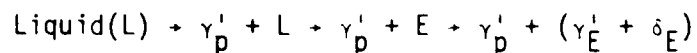
TABLE OF CONTENTS

	Page
EXECUTIVE SUMMARY.....	iii
1. INTRODUCTION.....	1
2. LASER CLADDING OF NICKEL-Cr-Al-Hf SYSTEM.....	1
2.1 Microstructure Evolution.....	1
2.1.1 Experimental Procedure.....	1
2.1.2 Results and Discussion.....	5
2.2 Oxidation Properties.....	39
2.2.1 Experimental Procedure.....	39
2.2.2 Results.....	44
2.2.3 Discussion.....	76
2.3 Conclusion.....	78
2.4 Future Work.....	79
3. LASER CLADDING OF Nb-Ti SYSTEM.....	80
3.1 Experimental Procedure.....	80
3.2 Results and Discussion.....	82
3.3 Conclusion.....	98
3.4 Future Work.....	101
4. MATHEMATICAL MODELING OF EXTENDED SOLID SOLUTION IN LASER CLADDING.....	103
4.1 Current Work.....	103
4.2 Future Work.....	104
5. REFERENCES.....	106
APPENDIX A: ONE-DIMENSIONAL MODEL FOR FINITE-MEDIUM DIFFUSION MODEL FOR EXTENDED SOLID SOLUTION IN LASER CLADDING OF Hf IN NICKEL.....	108
APPENDIX B: EXTENDED SOLID SOLUTION AND NONEQUILIBRIUM PHASE DIAGRAM FOR Ni-Al ALLOY FORMED DURING LASER CLADDING..	157

EXECUTIVE SUMMARY

This report summarizes experimental and theoretical studies carried out during the period of November 1986 to October 1987 on laser cladding of Ni and Nb alloys for improved environmental resistance at high temperature. Major emphasis has been on Ni-Cr-Al-Hf system. Microstructural evolution and oxidation properties of these alloys were examined. For Nb alloys microstructural characterization and differential thermal analysis were carried out. One-dimensional diffusion model for finite domain to examine the extended solid solubility in laser cladding was also developed.

Laser cladding of Ni-Cr-Al-Hf for various compositions were carried out including one close to stoichiometric Ni_3Al with chromium and Hf. Microstructure of these alloys were characterized using optical, scanning and transmission electron microscopic techniques. Convergent beam techniques were applied in TEM to identify small phases. X-ray analysis with SEM and TEM and Auger Spectroscopy were carried out to determine the microchemistry and crystal structure. Differential thermal analysis (DTA) was also performed to obtain the γ' dissolution temperature. Previous report discussed the microstructure evolution of Ni-Cr-Al-Hf with 58 at% Ni. This report mainly discusses the microstructure evolution for Ni-Cr-Al-Hf with 70 at% Ni (near stoichiometric Ni_3Al). The microstructure of these alloys mainly consists of dendritic zone full of γ' (Ni_3Al) and Hf rich interdendritic eutectics. Aluminum in Ni_3Al was often found to be partially replaced by Cr and Hf. Although there were some subtle differences in cell spacing, composition and other minor features between the samples depending on the process parameters but within the range of experimental parameters no radical differences were observed. Based on the observations made the possible phase transformation sequence of this group of laser clad Ni-Cr-Al-Hf are suggested below.



where γ'_p is primary γ' phase with ordered f.c.c. structure ($L1_2$), γ'_E is eutectic γ' phase with ordered f.c.c structure, E is eutectic phase and δ_E is the other eutectic phase with heavily faulted f.c.c structure.

Antiphase boundaries (APBs), in the γ' (ordered f.c.c) phase and the effect of process parameters on their morphology was also discussed. Initial DTA work indicated that γ' -dissolution temperature is at least as high as Rene 80 if not higher. More work is needed in this area.

Thermogravimetric analysis for the evaluation of oxidation resistance were carried out. Initial studies indicated that 58 at.% Ni+Cr+Al+Hf clad alloy lead to marginal improvement of oxidation resistance over Rene 80 whereas 70 at.% Ni Cr+Al+Hf promised far superior oxidation resistance.

Laser cladding of Ti on Nb was carried out to improve high temperature oxidation properties. The microstructure characterization revealed considerable amount of amorphous phase in this system. Also the clad region consisted of heavily faulted martensitic plates. Differential scanning calorimetry revealed the lower temperature of onset for $\alpha \rightarrow \beta$ transformation (860.2°C), indicating the extended solubility of Nb in titanium. However, during this reporting period very little work was done for Mg alloys and a proper powder delivery system is now being calibrated for this study.

In addition to the experimental work theoretical modeling of diffusion was also carried out to estimate the extent of the extended solid solution in laser cladding. By incorporating non-equilibrium partition coefficient for dilute solution the model was used to determine non-equilibrium phase diagram

for Ni-Hf and Ni-Al systems. The theoretical prediction reasonably agreed with the experimental data. Presently, we are developing a mathematical model for non-equilibrium partition coefficient for concentrated solution which will further improve our understanding of the process.

1. INTRODUCTION

The objectives of this project is fundamental investigation of laser cladding process for Ni-Cr-Al-Hf, Nb and Mg alloys for improved environmental resistance. Ni and Nb alloys are main candidate alloys for high temperature oxidation resistance. Rationale for the process and composition was already discussed in the previous report and publications. Dual theoretical and experimental approach is followed to develop the understanding of the extended solid solution formation in this process and its effect on microstructure and properties.

2. LASER CLADDING OF NI-CR-AL-HF SYSTEM

2.1 MICROSTRUCTURAL EVOLUTION

2.1.1 EXPERIMENTAL PROCEDURES

Elemental powders of various sizes and weight ratios were mixed in order to obtain a powder mixture for the desired composition of the cladding.

Sizes of the metal powders and their nominal compositions are:

Table 2.1-1

Element	Size	Purity
Ni Powder	3-7 microns	99.9 Purity (wt%)
Al Powder	20 microns	99% Purity (wt%)
Cr Powder	2 microns	99.5% Purity (wt%)
Hf Powder	<44 microns	99.6% pure containing 2.2 wt% Zr

The powders were mixed in various proportions and then tests were run on clad samples in order to determine the optimal composition for the purpose of improved high temperature properties.

Table 2.1-2

Element	wt.%				at.%			
	Comp. 1	Comp. 2	Comp. 3	Comp. 4	Comp. 1	Comp. 2	Comp. 3	Comp. 4
Ni	62.5	58.8	74.1	77.6	58.8	58.4	70.0	70.0
Cr	25.0	23.5	6.6	8.8	26.6	26.1	7.0	9.0
Al	6.25	5.9	9.7	10.2	12.8	12.6	20.0	20.0
Hf	6.25	11.8	9.6	3.4	1.8	2.9	3.0	1.0
					58-26-2-13 Series	58-26-4-12 Series	70-7-3-20 Series	70-9-1-20 Series

The powders are initially mixed and then mechanically stirred before drying. The drying process is carried out by heating the powders in an open boat in a tube furnace at 200°C with a steady flow of argon, for about 8 hours followed by slow cooling to room temperature.

The experimental apparatus for laser cladding consists of two units working simultaneously. The laser system, first unit, produces a beam that interacts with the substrate and powder to form the clad. The cladding process was carried out using an AVCO HPL 10 kW continuous wave CO₂ laser with F7 Cassegrain optics as shown in Fig. 2.1-1.

The laser was operated at a TEM₀₁* mode‡. The beam that was produced by the optics mentioned above was focussed downwards by substrate by a flat mirror. Cladding was typically done under an argon gas shield, at about 14 mm below the focal point and 3 mm beam diameter.

The powder delivery system, the second unit, delivers powder to the substrate. It consists of an Accu-Rate™ powder dispenser, funnel and an argon gas inlet. The powder dispenser is a pneumatic screw feed system with a feed

‡Donut shaped beam with Gaussian power distribution in the outer ring and none at the hole of the donut.

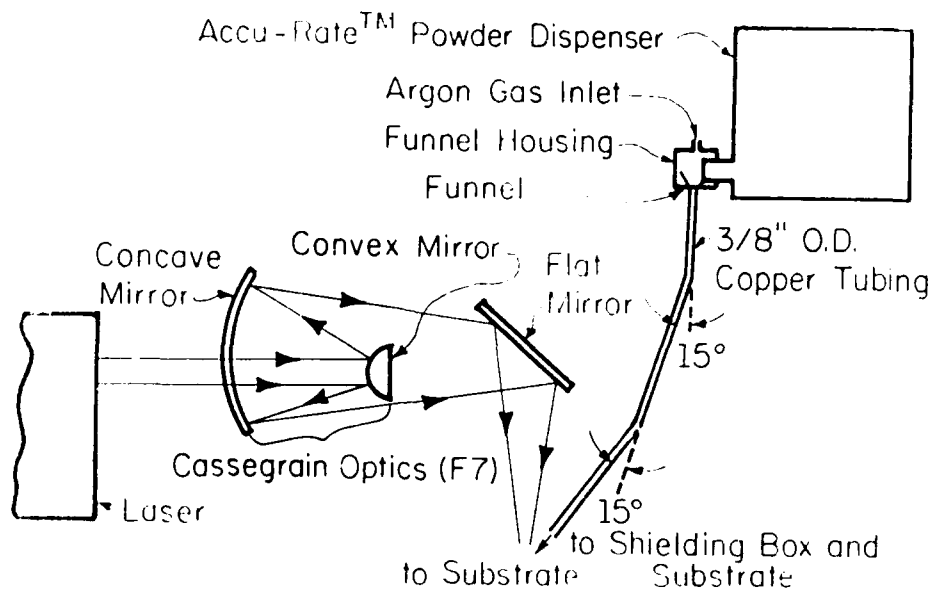


Figure 2.1-1 Optics used for laser cladding.

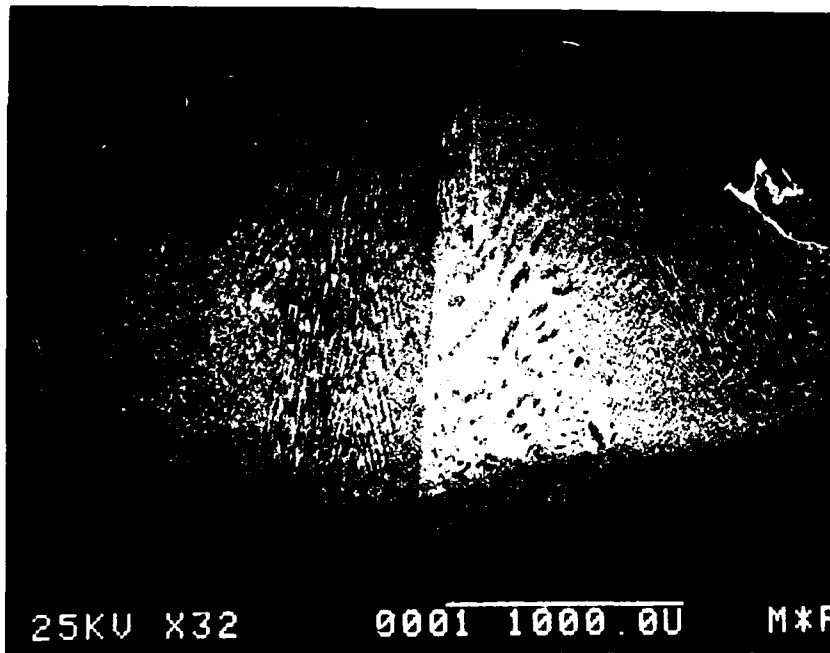


Figure 2.1-2 Scanning electron micrograph of sample L cross section showing the clad and the substrate material and the diffusion zone.

rate which was varied between 2.7 gm/sec to 1.7 gm/sec. (for Ni-Cr-Al-Hf system). Powder falls from the screw into a funnel and flows to the substrate. A small amount of argon gas flows in the tube along with the powder flow in order to make the powder flow uniform. This in situ (direct powder placement) cladding process is known to have advantages over the preplaced powder cladding procedure [1]. Since it requires lower specific energy input leading to finer microstructure. An argon gas shield was also provided with the help of a shielding box so as to obtain an oxide free clad and also to reduce the clad porosity.

For the present investigation the laser was operated at 3 to 9 kW. Specimens of substrate material of thickness 10 mm and surface preparation as milled, were traversed relative to the laser beam at speeds varying from 10.6 to 25.4 mm per second. The substrate material was a nickel based superalloy, trade named Rene 80.

Microstructural characterization, which is the main scope of this part of the report, of the clad material was performed using optical microscope, scanning electron microscope, (JOEL 35C, HITACHI S-800) transmission electron microscopes (Phillips 400, 420, and 430T) and scanning transmission electron microscope (HB-5). the substrate material is abraded off the cladding and then finally thinned mechanically to a thickness of 0.3 mm. 3 mm discs are punched out from this thinned material. Twin jet chemical polishing technique (Fischione) is utilized for sample preparation for observation in the TEM.

Electrolyte: 200 cc. of butoxyethanol
400 cc. of methanol
50 cc. of perchloric acid

Conditions: 35 V, - 15°C

Cross sections of the original clad samples were polished for observation in the SEM and optical microscopes.

Differential thermal analysis (DTA) was also performed in order to obtain the γ' dissolution temperature of the clad and the substrate material. The DTA used was Perkin Elmer system 4/7, with a high temperature cell attachment. Sample preparation is much simpler for DTA work. Small pieces of the clad material weighing between 10.0 through 70.0 mgm are put into a sample cup and then it is filled with Al_2O_3 . The reference cup is filled to approximately the same level with only Al_2O_3 before the DTA runs are made. The heating rate is $20^\circ C/min$, and argon gas at about 40 mls/min was used as the atmosphere.

Thermogravimetric tests and Auger spectrometry of the samples have also been done to understand the oxidation behavior of the clads. Detailed discussion of the procedure and results will appear elsewhere in this report.

2.1.2 RESULTS AND DISCUSSION

The focus of this entire research project has been to obtain through experimental and theoretical research efforts some materials which would be very strong candidates for laser cladding of nickel based superalloys. The properties which are of importance to our sponsors have been various, although, most of these are closely related. Of prime importance is the high temperature ($1200^\circ C$) oxidation property of the clad material in comparison to the oxidation response of the nickel base superalloys which are to be clad. There is also a strong and purposeful effort to minimize the Cr content in these clad materials, thus leading to savings of a strategic material.

A thorough characterization of the microstructure of laser clad materials using electron and optical microscopy and x-ray spectroscopy is also of importance as there is always a direct correlation between material property and its microstructure. This part of the project report, therefore, deals with the microstructural evolution of certain laser clad materials and the relationship of the process parameters with these microstructures.

Since composition 1 (58-26-2-13 series) and 2 (58-26-4-12 series) (partially) have been discussed in detail in our previous years report and work by Singh and Mazumder [2] we would deal with composition 3 (70-7-3-20 series) mainly for the purpose of this report. Composition 4 (70-9-1-20 series) is only a small modification of composition 3 in that the Cr and Hf compositions are varied slightly. The results of this modification is being studied at present. The table below shows the process parameters used with powder mixture of composition 3 during the laser cladding operation.

Table 2.1-3

Sample	Laser Power	Powder Feed Rate	Traverse Speed
L	9 kW	2.2 gm/sec	19 mm/sec
K	7 kW	2.2 gm/sec	19 mm/sec
J	5 kW	2.2 gm/sec	19 mm/sec

Figure 2.1-2 shows a scanning electron micrograph of a cross section of the cladding for sample L. The left part of this micrograph represents a region in the sample which was etched, whereas the right part of the micrograph represents the unetched region of the sample. As can be seen from the micrograph, the entire cladding area has a much finer microstructure as compared to the substrate material. At the magnification of the micrograph it is extremely difficult to see any of the undissolved or partially dissolved Hf

particles. The clad region forms a small hemispherical bead on the surface of the substrate. The interface between the clad and the substrate appears to be an extremely thin well diffused zone. A high magnification picture taken from the sample L dendritic clad area is shown in the next micrograph (Fig. 2.1-3).

This micrograph shows the dendritic cell formation in the sample L. Use of X-ray spectroscopy indicates that the white regions are Hf rich regions, whereas the dark regions are Hf depleted, Ni rich regions. Closer observation of the micrograph would also indicate that there are a lot of partially dissolved hafnium particles in the clad.

At this point, it is important to note that the microstructural characteristics of the other clads of the same composition (samples J, L, etc.) are very much similar. However, there are very subtle differences in terms of dendritic cell sizes, compositions of the cell interior, structures of the cell interior and also the relative amount of phases formed..

Figures 2.1-4 and 2.1-5 are scanning electron micrographs of the clad areas in sample J at higher magnification. The white Hf rich regions are partially resolved in these micrographs. Investigation indicates that these regions undergo a certain eutectic transformation, as can be evidenced by the lamellar structure. On the basis of the micrographs presented earlier and further work which will be presented later in this report, one can safely make some conclusions on the evolution of microstructure in laser cladding process in this system. The dendrites are initially formed from the super saturated solid solution of Hf in Ni-Cr-Al. Due to the quick cooling process associated with the laser cladding process, metastable solute segregation takes place in the system. A higher amount of Hf, as compared to equilibrium solid solution in the dendrites (terminal solid solution) is observed. Exact compositional data will be presented in a later part of the report. The excess of the Hf is

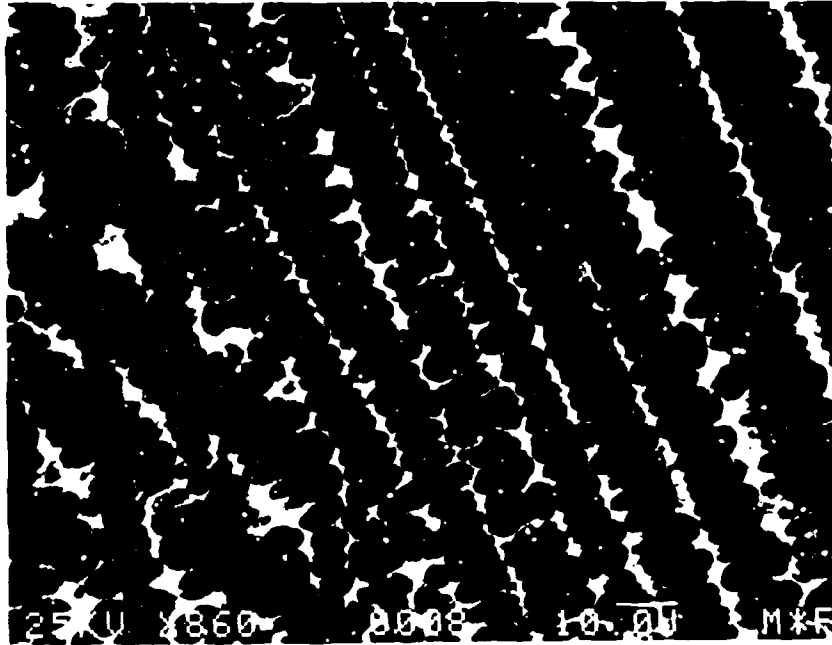


Figure 2.1-3 Scanning electron micrograph of sample L, showing dendrites in the clad material.

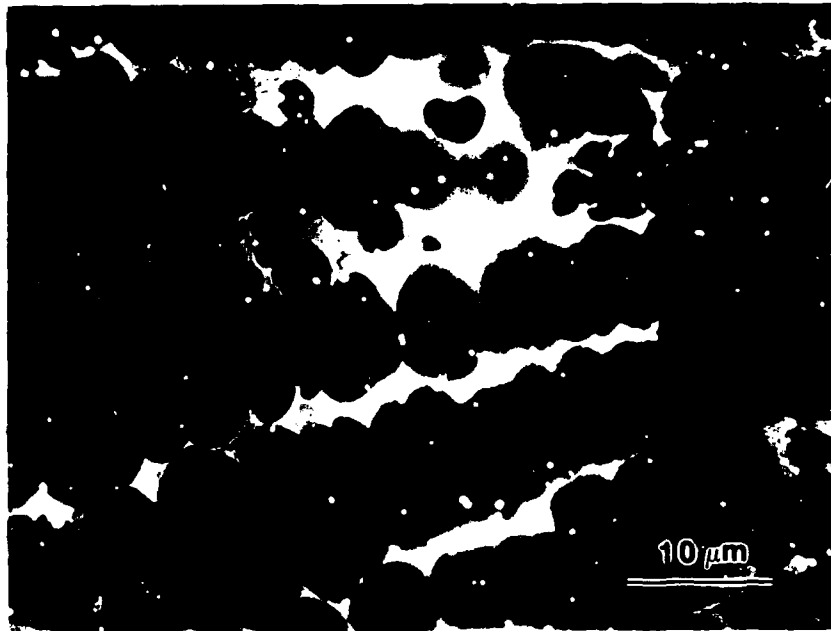


Figure 2.1-4 Scanning electron micrograph of sample J, showing dendrites, and partially dissolved hafnium particles.



Figure 2.1-5 Scanning electron micrograph of sample J, showing dendrites, eutectic structure and partially dissolved hafnium particles as indicated by arrows.

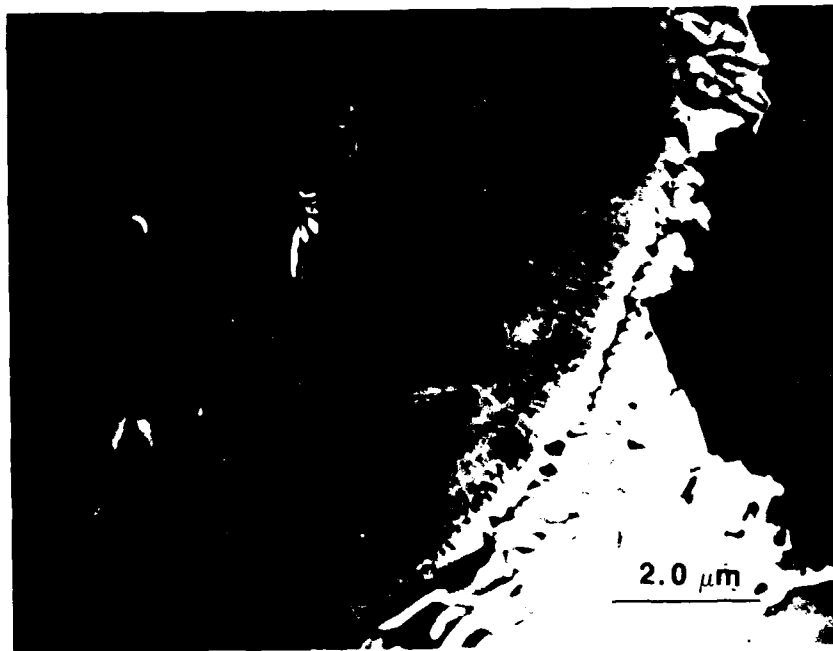


Figure 2.1-6 Dark field scanning transmission electron micrograph of sample L, showing one dendritic cell and the eutectic structure.

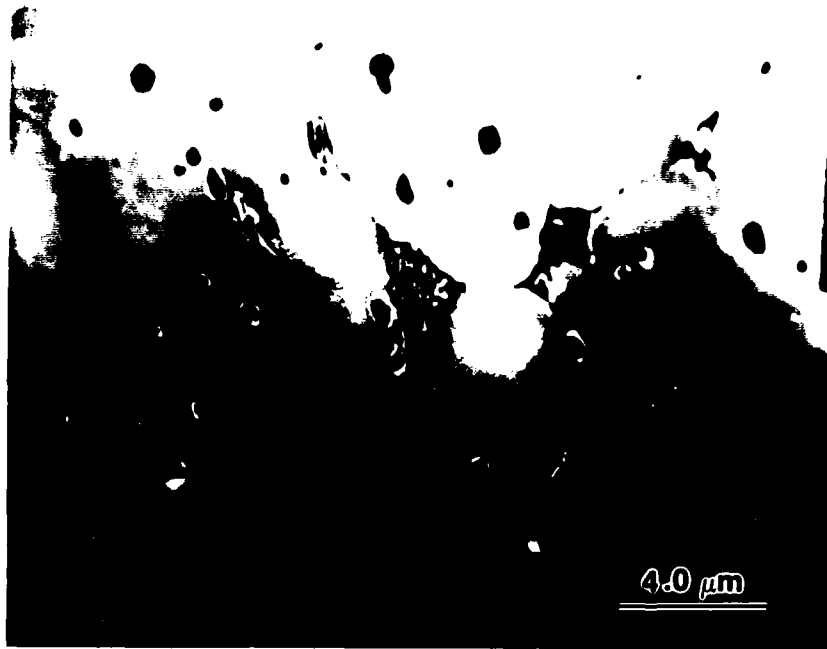


Figure 2.1-7 Dark field scanning transmission electron micrograph of sample K, showing dendrites, eutectic structure and partially dissolved hafnium particles.

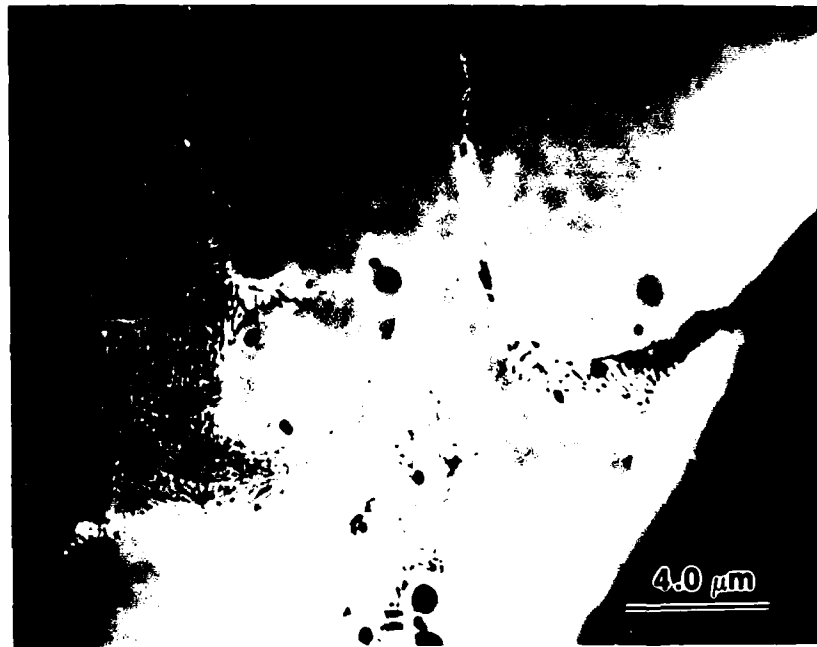


Figure 2.1-8 Dark field scanning transmission electron micrograph of sample J, showing dendrites, eutectic structure and partially dissolved hafnium particles.

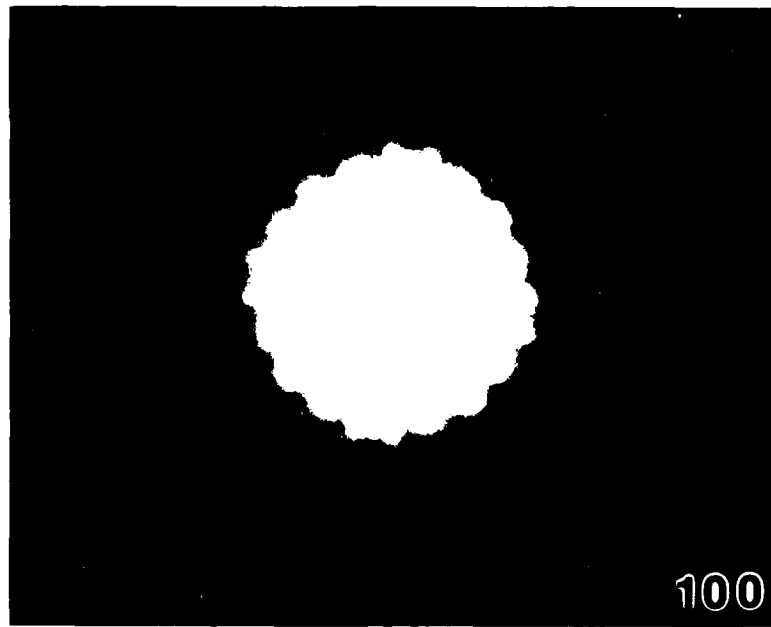


Figure 2.1-9 CBED pattern for [100] zone axis of the γ' at C.L. = 290 mm.

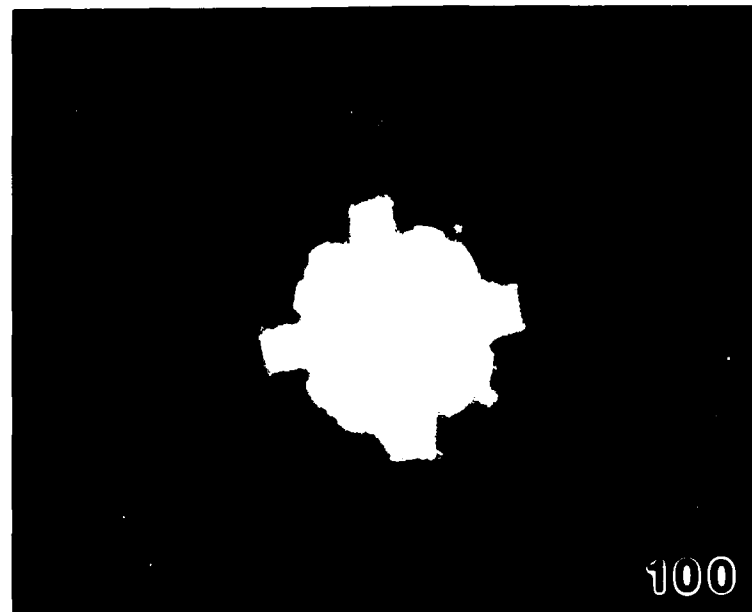


Figure 2.1-10 CBED pattern for [100] zone axis of the γ' at C.L. = 800 mm.

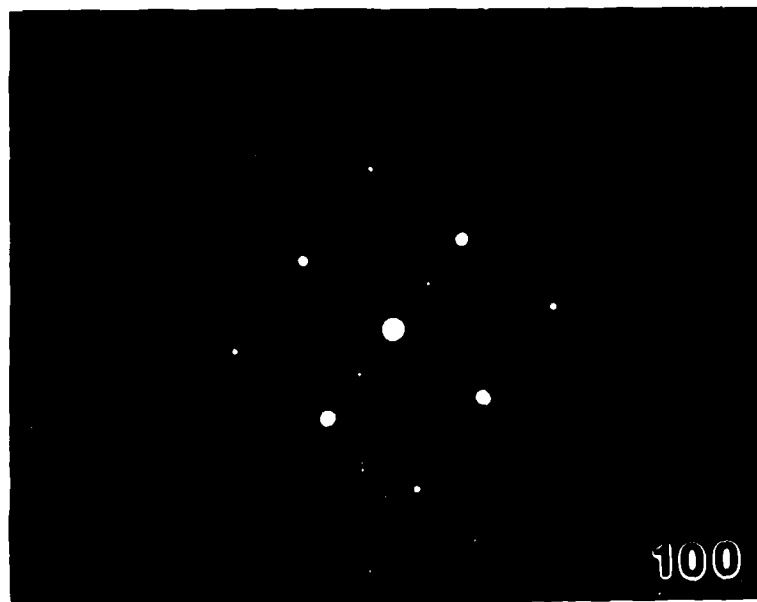


Figure 2.1-11 SADP for the $[100]$ zone axis of γ' at C.L. = 800 mm., showing superlattice reflection.

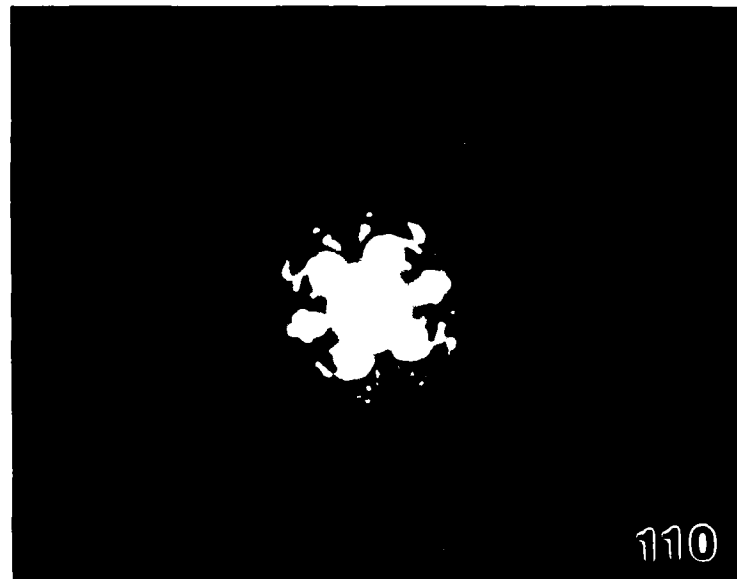


Figure 2.1-12 CBED pattern for [110] zone axis of γ' at C.L. = 575 mm.

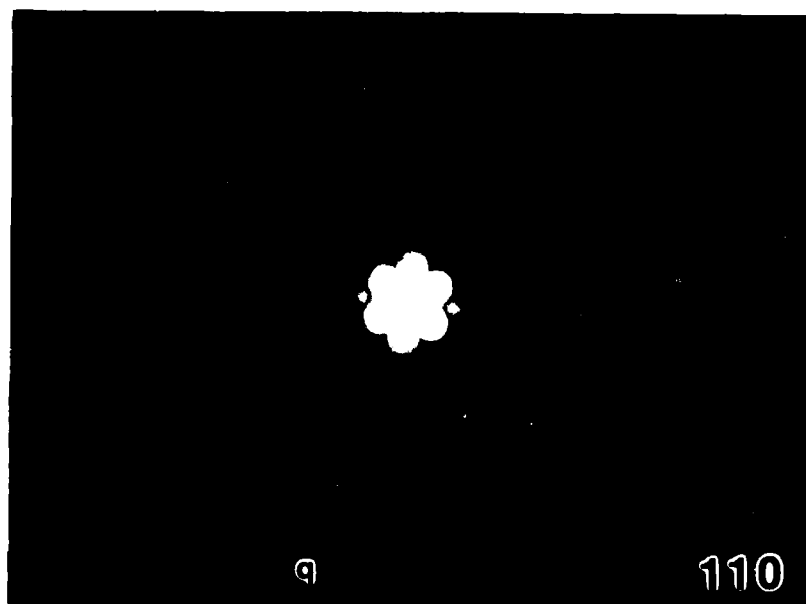


Figure 2.1-13 CBED pattern for [110] zone axis of γ' at C.L. = 290 mm.

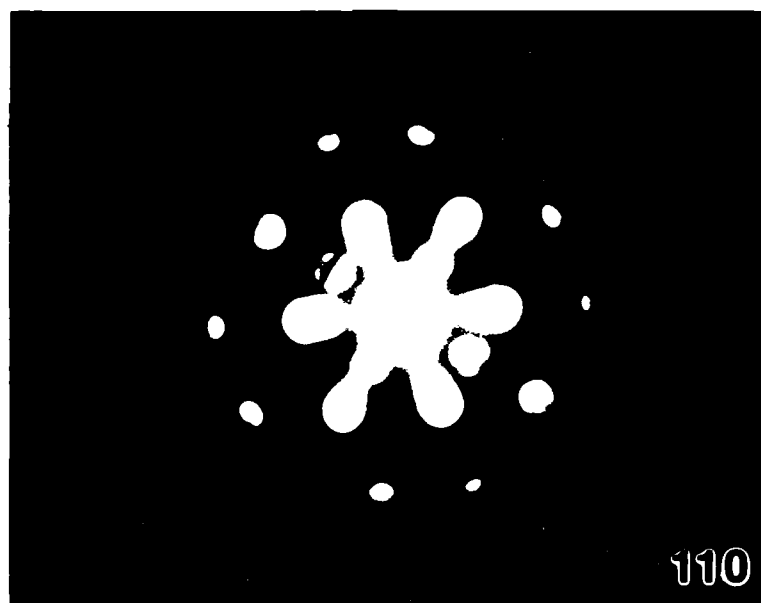


Figure 2.1-14 CBED pattern for [110] zone axis of γ' using a smaller condenser aperture showing the superlattice discs at C.L. = 800 mm.

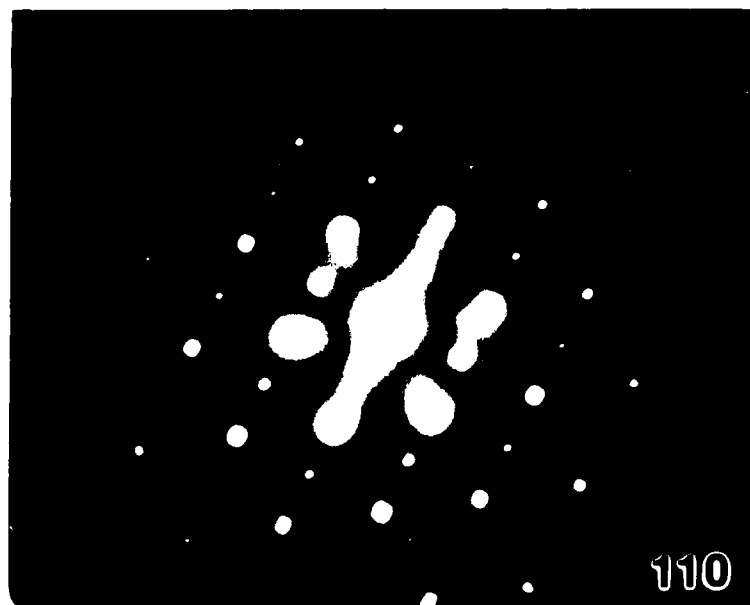


Figure 2.1-15 SADP pattern for the [110] zone axis of γ' at C.L. = 800 mm. showing superlattice reflections

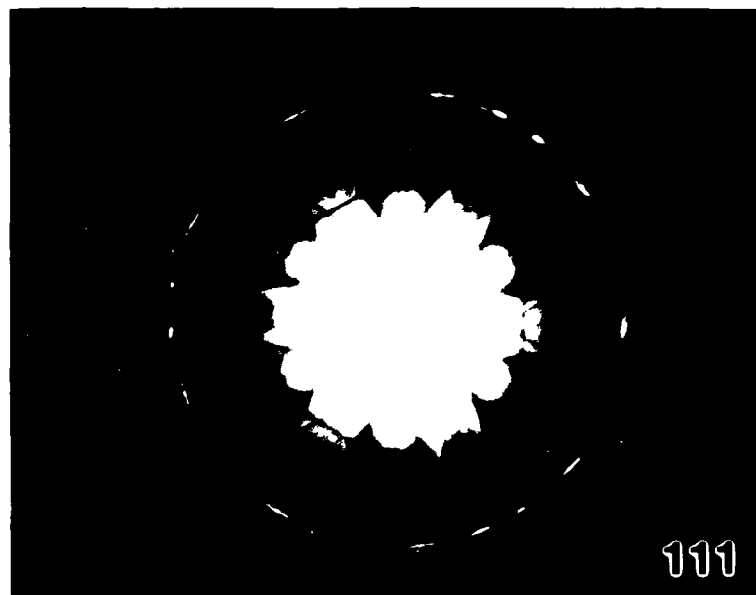


Figure 2.1-16 CBED pattern for $[111]$ zone axis of γ' at C.L. = 290 mm.

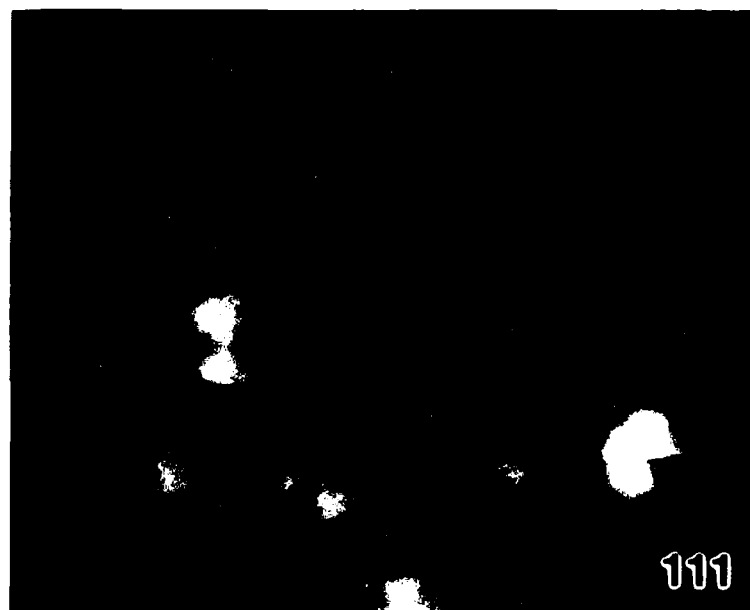


Figure 2.1-17 CBED pattern for $[111]$ zone axis of γ' at C.L. = 800 mm.

On the basis of the above patterns in Figs. 2.1-16 and 2.1-17, the following two tables (Tables 2.1-4 and 2.1-5) are made up to indicate the symmetries observed. Phase identification of the dendritic cells formed during laser cladding of nickel based superalloys.

Table 2.1-4 Observed Symmetries and Deduced Diffraction Groups

Zone Axis	Observed Symmetry		Deduced Diffraction Groups
	Zero Order Zone	Whole Pattern	
[001]	4 mm	4 mm	4 mm or 4 mm 1_R
[011]	2 mm	2 mm	2 mm or 2 mm 1_R
[111]	6 mm	3 mm	6_R mm_R

Table 2.1-5
Possible Point Groups Corresponding to the Deduced Diffraction Groups

Deduced Diffraction Group	Possible Point Groups
4 mm	4 mm
4 mm 1_R	4/mmm $m3m$
2 mm	$mm2$ $\bar{6}m2$
2 mm 1_R	mmm 4/mmm 6/mmm $m3$ $m3m$
6_R mm_R	$\bar{3}m$ $m3m$

These tables are obtained using Table 2.1-3 of Buxton, et al. [3]. From the tables above, it can be established that the point group of the dendritic cells is $m3m$. From the SADPs it can also be analyzed that the crystal structure is ordered f.c.c ($L1_2$) with a lattice parameter $a_0 \approx 3.458 \text{ \AA}$.

In the bright field mode in the TEM the eutectic zone appears as mixture of two phases, one bright and the other dark, both of which are lamellar in morphology—one placed next to the other. The next three micrographs (Figs. 2.1-18 through 2.1-20) depict this eutectic structure very clearly. It is important to remember that this eutectic structure actually forms in the region between two dendritic cells. The dark regions of the eutectic shows extremely fine lines as part of the microstructure indicative of either a heavily faulted structure or an internally twinned structure. Some further TEM experiments need to be performed in order to determine whether this is a faulted or a twinned structure. The bright regions of the eutectic are interconnected all through the region and also tend to show the same crystal orientation in one area.

Convergent Beam Electron Diffraction (CBED) patterns were recorded for the bright area of the eutectic. The following figures (Figs. 2.1-21 through 2.1-24) depict the [013] and the [110] zone axis patterns (ZAPS) at different camera lengths. On the basis of the above patterns, the following two tables (Tables 2.1-6 and 2.1-7) are written up to indicate the observed symmetries and the point groups of the bright area of the eutectic.

Table 2.1-6 Observed Symmetries and Deduced Diffraction Group

Zone Axis	Observed Symmetry		Deduced Diffraction Groups
	Zero order zone	whole pattern	
[013]	2 m	m	$2_R m m_R$
[110]	m	m	m or $m 1_R$
[111]	3 m	3 m	3 m

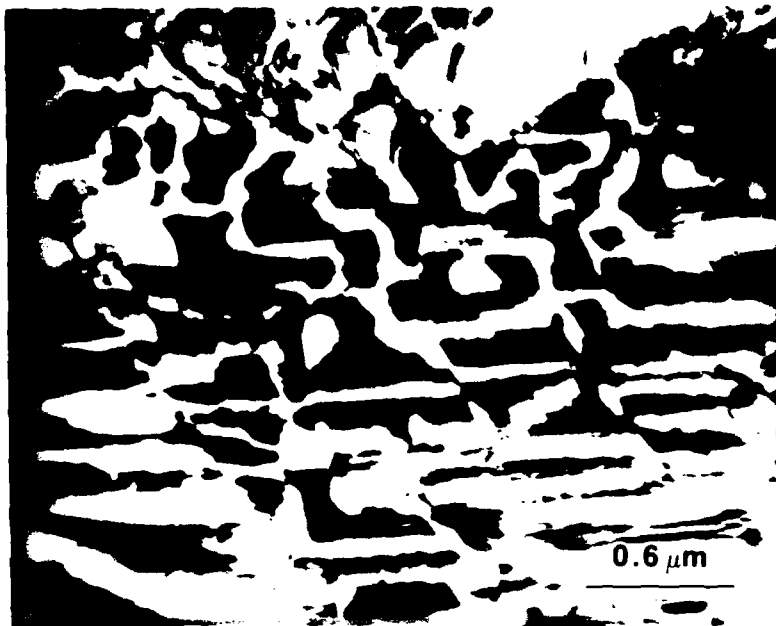


Figure 2.1-18 Bright field TEM image of γ' + eutectic region ($\gamma'_E + \delta_E$). Striations in one of the eutectic phases (δ_E) is visible.



Figure 2.1-19 Bright field TEM image of γ' + eutectic region. The lamellar eutectic structure is visible.



Figure 2.1-20 Bright field TEM of eutectic region showing fine lines in the δ_E phase indicative of faulted structure.

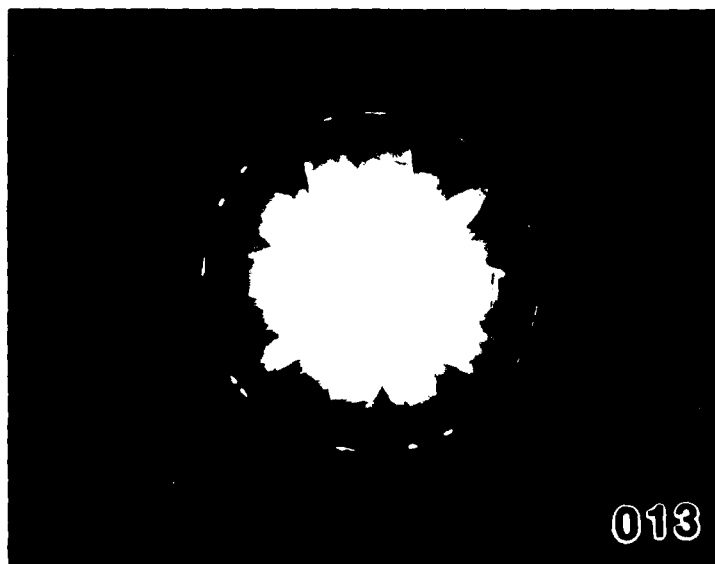


Figure 2.1-21 CBED patterns for [013] zone axis of the γ'_E phase at C.L. = 210 mm.

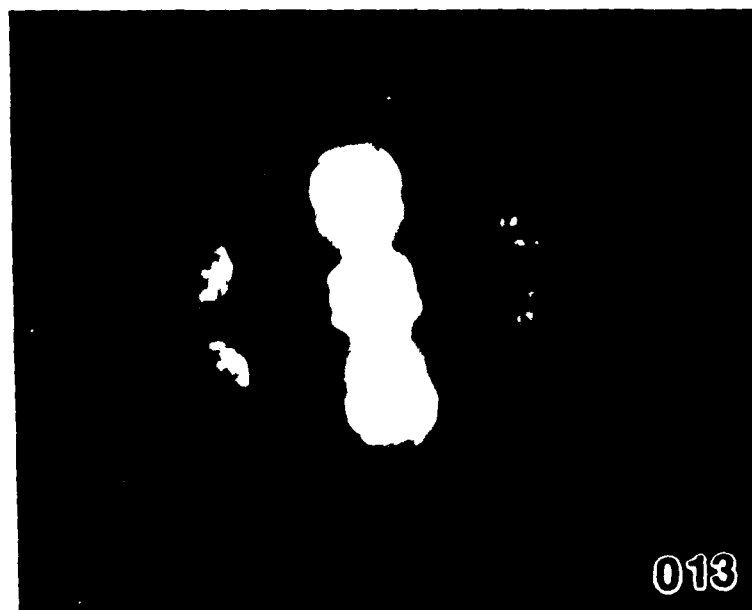


Figure 2.1-22 CBED patterns for [013] zone axis of the γ'_E phase at C.L. = 800 mm.

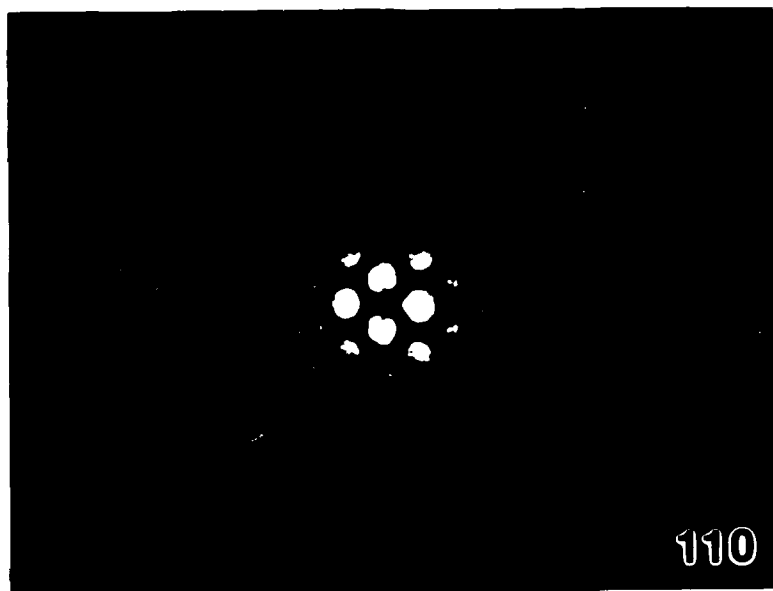


Figure 2.1-23 CBED patterns for $[110]$ zone axis of the γ'_E phase at C.L. = 350 mm.

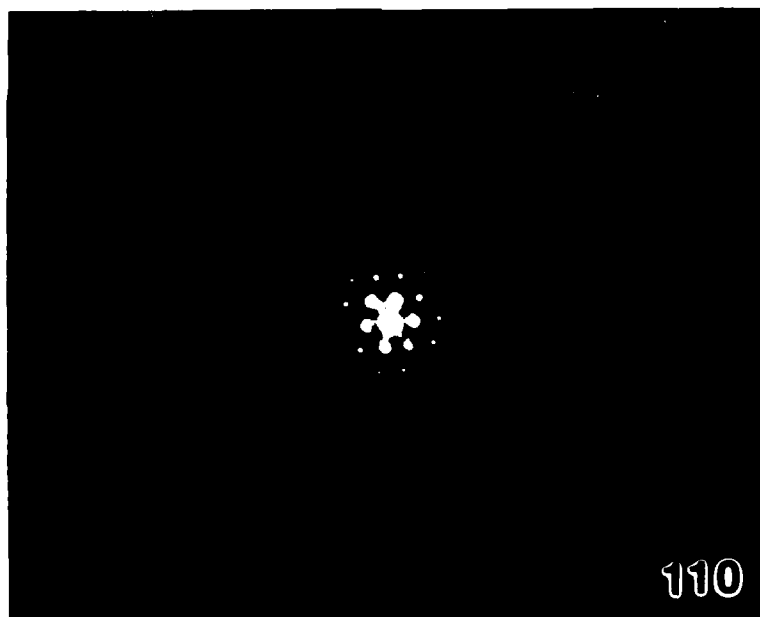


Figure 2.1-24 CBED patterns for $[110]$ zone axis of the γ'_E phase at C.L. = 210 mm.

Table 2.1-7
Possible Point Groups Corresponding to the Deduced Diffraction Groups

Deduced Diffraction Groups	Possible Point Groups									
2_R mm_R	$2/m$	mmm	$4/m$	$4/mmm$	$\bar{3}m$	$6/m$	$6/mmm$	$m\bar{3}$	$m\bar{3}m$	
m	m	$mm2$	$4mm$	$\bar{4}2m$	$3m$	$\bar{6}$	$6mm$	$\bar{6}m2$	$\bar{4}3m$	
$m\bar{1}_R$	$mm2$	$3mm$	$\bar{4}2m$				$6mm$	$\bar{6}m2$	$\bar{4}3m$	
$3m$				$3m$					$\bar{4}3m$	

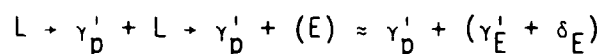
Based on the above studies, and microdiffraction results in the STEM, we conclude that the point group of the bright region in the eutectic is $\bar{4}3m$ and the crystal structure is an ordered f.c.c. In fact, the spots pattern shown in Fig. 2.1-24 exhibits the superlattice reflections indicative of ordering. This phase from now on would be referred to as the eutectic γ' phase. Lattice parameter of eutectic $\gamma' \approx 3.62 \text{ \AA}$.

The determination of the crystal structure of the other eutectic phase (dark region in a bright field TEM micrograph), here to referred to as δ phase, is extremely difficult due to the internal defect structure of the phase. Specifically, the CBED method could not be applied. However, SADP of the γ' phase along with a small part of the δ phase was taken for [011] and [001] orientation of the γ' phase. Figure 2.1-25(a) and (b) show the [011] orientation of the γ' phase superimposed with the [132] orientation of the δ phase. The $\langle 33\bar{3} \rangle_{\delta}$ was approximately parallel to $\langle 11\bar{1} \rangle_{\gamma'}$. The δ spots appear at every $1/3 \langle 11\bar{1} \rangle_{\gamma'}$ spots approximately. The crystal structure of the δ phase is f.c.c, but it is extremely faulted internally. The lattice parameter of the δ phase on the basis of this indexing, $a_0 \approx 10.96 \text{ \AA}$. The quick cool down process, which is inherent to the laser cladding process could give rise to the high internal defect structure to accommodate the high

thermal and phase transition stresses in the system. Proper orientation of the image with respect to the bright field images in Figs. 2.1-18, 2.1-19, and 2.1-20 indicates that the streaks in the diffraction pattern are perpendicular to the fine lines observed in the δ phase.

Figures 2.1-26(a) and 2.1-26(b) are the SADP and analysis, respectively from a part of the γ' and the δ phase. The orientation of γ' is [011] and that of the δ phase is $[\bar{1}22]_{f.c.c}$. The $\langle 2\bar{2}0 \rangle$ of the γ' is parallel approximately to the $\langle 066 \rangle$ of the δ phase and the $\langle 0\bar{2}0 \rangle_{\gamma'}$ is approximately parallel to $\langle 442 \rangle_{\delta}$. From this analysis also, it appears that the δ diffraction spots appear at every $1/3 \langle 2\bar{2}0 \rangle_{\gamma'}$ positions. The crystal structure can be reaffirmed to be f.c.c with lattice parameter $a_0 \approx 10.96 \text{ \AA}$.

Based on the previous discussion it is possible to make a suggestion on the microstructure evolution process in this system. The possible phase transformation sequence could be presented as follows.



where

L = liquid phase

E = eutectic phase

γ'_p = primary γ' phase (ordered f.c.c) $L1_2$

γ'_E = eutectic γ' phase (ordered f.c.c)

$\delta_E = \delta$ = other eutectic phase (heavily faulted, f.c.c)

δ_p = primary δ phase

Energy dispersive X-ray microanalysis of these phases to determine chemistry of these phases will be presented elsewhere in this report.

A pseudo metastable binary eutectic phase diagram can be constructed based on the microstructural analysis presented earlier. A tentative sketch for the system is given in Fig. 2.1-27. However, further DTA work has to be carried out to develop the diagram.

Anti-Phase Boundaries (APBs) in the γ' (ordered f.c.c) Phase and their Morphology Dependences Based on Processing Parameters

Studies of APBs in $L1_2$ structure have been performed by various authors [4,5]. The shape or morphology of the APBs is a function of the APB energy of the system with respect to the crystal structure of the system. If the APB energy for a particular system is isotropic then the morphology of the APBs are extremely round (no sharp faceted features) and there is no preferred orientation of the APBs.

The antiphase boundary energy in $L1_2$ alloys has been calculated to be anisotropic, with the lowest energy in $\{100\}$ planes, taking into account the first nearest neighbor interactions only [4]. Accordingly, there is a driving force for an APB to be on cube planes in these alloys. When this occurs, the electron microscope shows "maze" pattern (as in Cu_3Au and Cu_3Pt) rather than the "swirl" pattern that is associated with superlattices having isotropic domain networks and APB energy (as in Ni_3Fe , Ni_3Mn , Fe_3Al). However, it is important to note that, although the APB energy may be anisotropic, there is finite time lag required for the APBs to align themselves in the direction of low APB energy. Prior to this happening, it would therefore appear that the APBs are a mixture of "maze" and "swirl" type of pattern. Hence, the laser processing parameters would definitely have an influence on the shape of the APBs in this system depending on the cooling rate achieved during the process.

Figure 2.1-28 is a bright field TEM image of a conglomeration of a number of dendritic cell of γ' in sample J. This low magnification shot provides an

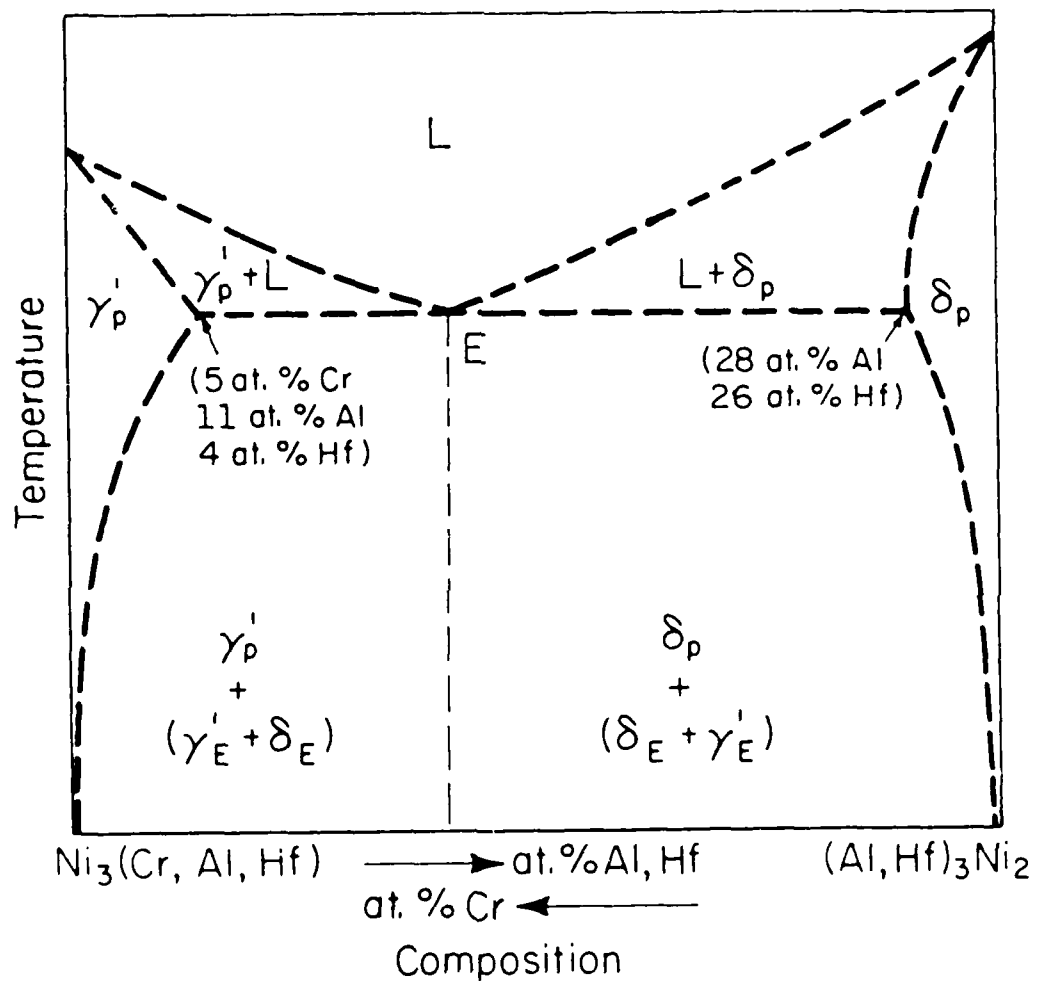


Figure 2.1-27 Tentative sketch of the pseudo metastable binary phase diagram drawn on the basis of microstructural and microchemical analysis.

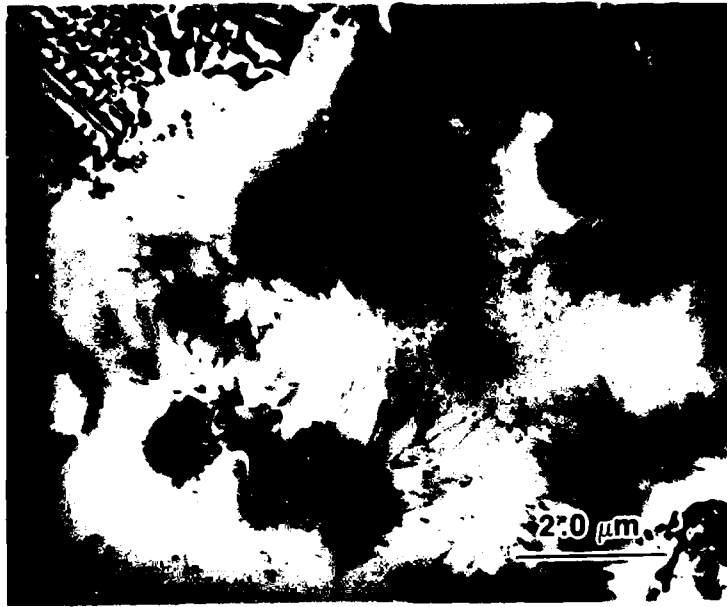


Figure 2.1-28 Bright field TEM image of sample J showing the antiphase domain structure in the γ' dendritic region.

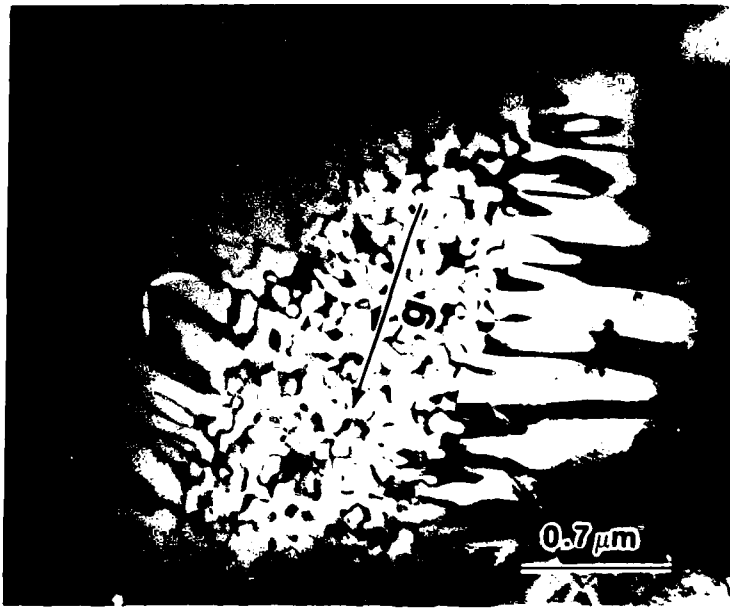


Figure 2.1-29 Dark field TEM image of sample J showing the different morphologies of the antiphase domains.

excellent in-depth insight into the morphology of the APBs inside the dendritic cells. Towards the edge of the dendritic cells, the APBs are columnar, with the width of the columns decreasing towards the interior of the grains. However, as the interior of the cell regions are reached, large number of extremely small polygonal APBs are observed. This structure is extremely analogous to the type of structure observed in cast ingots. The process of heat extraction could also be quite analogous to that observed in the case of cast ingots. The external boundary of the dendritic cells may form at a very early stage and then the heat extraction preferably would take place through the dendrite boundary forming columnar APBs perpendicular to the boundary surface. The last, relatively slow, stage of heat extraction then takes place at the interior of the dendritic cells, giving rise to polygonal APB. The black dots seen in this figure (Fig. 2.1-28) represents the partially dissolved Hf particles in the matrix.

Figures (2.1-29 and 2.1-30) show a higher magnification dark field image of the region where the columnar and polygonal APBs meet. Close examination of the polygonal APBs indicate that these are a mixture of both the "maze" and "swirl" types of patterns. There are some rounded edges mixed with some which have sharp faceted edges. The next figure (Fig. 2.1-31) explains this aspect even more explicitly. All these dark field images were taken with (100) superlattice reflection of the γ' structure. Similar sets of micrographs taken from sample L (higher laser power used during cladding, Table 2.1-3) provide some very interesting contrasts.

Figure 2.1-32 shows a low magnification TEM dark field micrograph for sample L. The sharp long columnar grains are no longer visible. They are replaced by large faceted APBs which lead up from the edge of the dendrites to the cell interior.



Figure 2.1-30 Dark field TEM image of sample J showing the different morphologies of the antiphase domains.

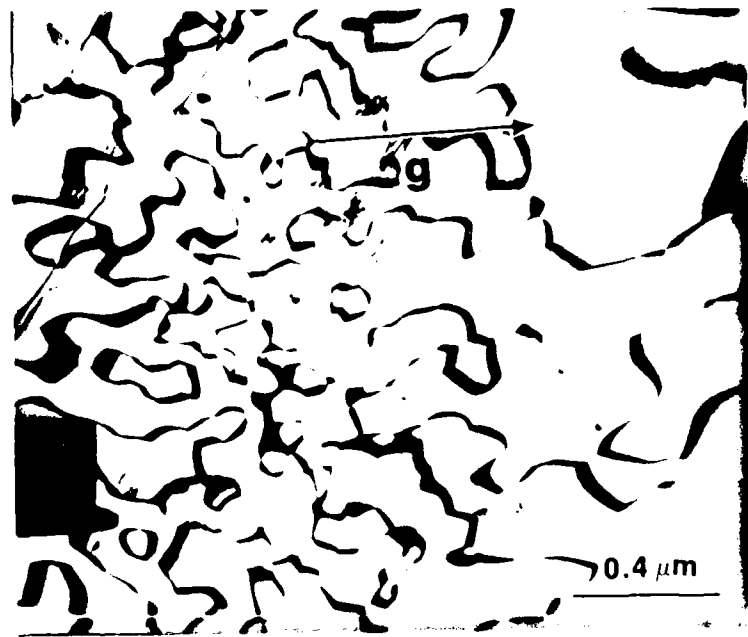


Figure 2.1-31 Dark field TEM image of sample J showing "swirl" type APB boundaries.



Figure 2.1-32 Dark field TEM image of sample L showing the antiphase domain structure in the γ' dendritic region.



Figure 2.1-33 Dark field TEM image of sample L showing the "mace" type APBs in the γ' interior indicative of anisotropic APB energy associated with the system.

The APBs which are located towards the interior of the dendrite cell are nearly all cuboid in shape. This means that the APBs are lined up on a particular direction, [100] in this case. This characteristic of the APBs can be observed even more vividly in the next (100) dark field micrograph, Fig. 2.1-33.

This difference in microstructural behavior between sample J and sample L may be explained in terms of laser processing parameters and specific energy input during the process. For constant traverse speed and powder feed rate, increased power leads to higher specific energy input, thereby leading to a slower cooling rate. Slower cooling rate would mean that there is more time available for the reorganizing of the APBs, and also higher temperatures available for the facilitation of the same. Hence, if the APB energy for a particular system is anisotropic, i.e., varies with difference in crystallographic planes, there is more possibility of the same to show up microstructurally at higher laser powers, due to the reasons mentioned above.

APB contrast occurs when α , the phase angle, given by $\alpha = 2\pi\bar{g}\cdot\bar{R}$ takes a non-zero value. \bar{g} is the operating reflection and R is the boundary displacement vector. The two types of APB displacement vectors possible for $L1_2$ type structure are the $1/2a_0\langle 110 \rangle$ type and the $1/6a_0\langle 112 \rangle$ type [8]. Table 2.1-8 [4] lists the antiphase angles associated with $(1/2)a_0\langle 110 \rangle$ and $(1/6)a_0\langle 112 \rangle$ type antiphase vectors in $L1_2$ crystal structure. $\pm\pi$ value of the phase angle is generally known as the π contrast condition. Under this diffracting condition the bright field and the dark field image in the TEM shows symmetrical contrast reversal.

Table 2.1-8 $L1_2$ Type Superlattices

Antiphase angles α associated with $(1/2)a_0\langle 110 \rangle$ and $(1/6)a_0\langle 112 \rangle$ type antiphase vectors in the $L1_2$ type superlattice.

hkl	Type of reflection	Antiphase angle α associated with $(1/2)a_0\langle 110 \rangle$ type antiphase vector	Antiphase angle α associated with $(1/6)a_0\langle 112 \rangle$ type antiphase vector
100	S	$\pm\pi$ or 0	$\pm \frac{\pi}{3}$ or $\pm \frac{2\pi}{3}$
110	S	$\pm\pi$ or 0	$\pm \frac{\pi}{3}$, $\pm \frac{2\pi}{3}$, $\pm\pi$ or 0
111	F	0	$\pm \frac{2\pi}{3}$ or 0
200	F	0	$\pm \frac{2\pi}{3}$ or 0
210	S	$\pm\pi$ or 0	$\pm \frac{\pi}{3}$, $\pm \frac{2\pi}{3}$, $\pm\pi$ or 0

Figures 2.1-34 and 2.1-35 are bright and dark field micrographs for sample L, taken from the central region of a dendritic cell. The dark field micrograph was taken with $(100)_s$ reflection, where s represents the superlattice reflection. As can be seen from the comparison of the two micrographs (Figs. 2.1-34 and 2.1-35), there is a complete symmetrical contrast reversal. Similar contrast reversal was also obtained using $(100)_s$ reflection. Various dendritic cell regions were examined, and the same results were obtained with regards to the symmetrical contrast reversal. This result leads one to believe that the $(1/2)a_0\langle 110 \rangle$ type of APB vector occurs almost exclusively in this system. Similar results were also obtained using samples J and K. Whether the quick cooling rate associated with the laser cladding process has any influence on this kind of behavior is a matter of interest and needs further experimentation.

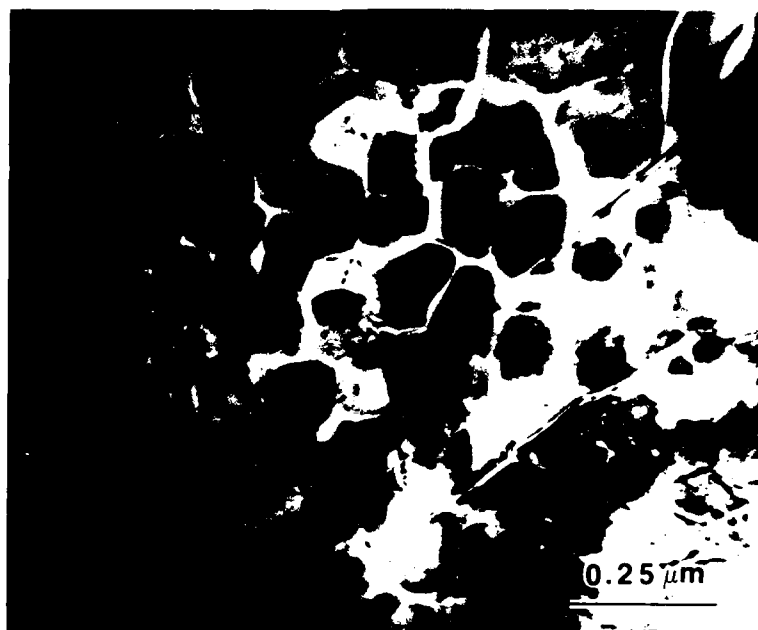


Figure 2.1-34 Bright field TEM image of sample L, showing the "maze" type APBs in the γ' interior.

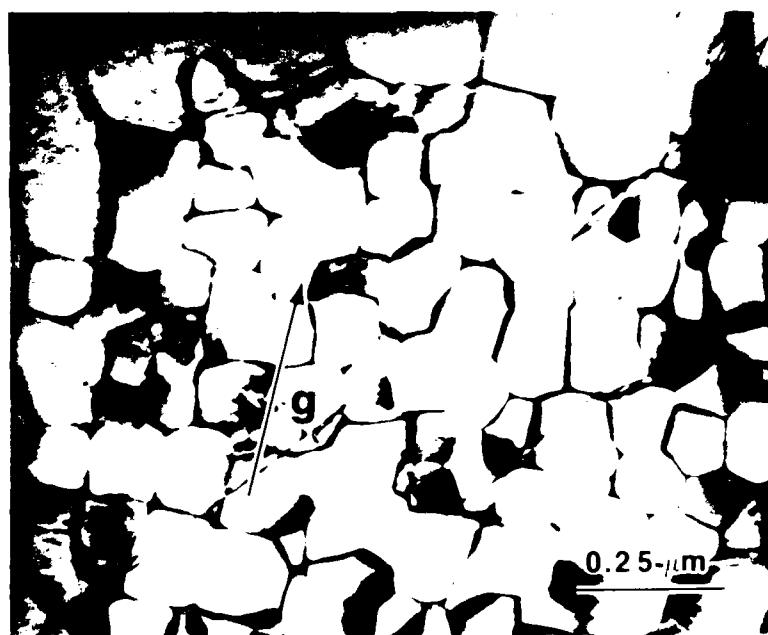


Figure 2.1-35 Dark field TEM image of the same region in sample L as that of Fig. 2.1-34, using (101) superlattice reflection, showing symmetrical contrast reversal.

Microchemistry Studies on Laser Clad Ni-Cr-Al-Hf Alloy

The energy dispersive X-ray analysis work was performed in the HB-5 scanning transmission electron microscope with a beam probe diameter of $\approx 10 \text{ \AA}$. The table below (Table 2.1-9) shows the micro-chemistry values for different regions in the dendrite and the eutectic phases for sample L. The regions from which the chemistry has been obtained is shown in Fig. 2.1-36. Based on the compositional analysis, there are few inferences which can be made, which in turn, further helps one to understand the evolution of microstructure in this system.

At the center of this dendrite the Hf concentration is about 13 wt%, but as one approaches the tip of the dendrite the Hf concentration increases up to about 20 to 25 wt%. This characteristic very clearly depicts the fact that the dendritic cell is formed by rejection of Hf towards the tip of the cell. Similar growth characteristics are also observed towards the thickness of dendritic cell. This type of behavior has also been observed in samples J and K, respectively. At this time we are performing more tests in order to determine the influence of laser processing parameters on this type of segregation. We believe that this influence (if any) would have a profound effect on some of the important properties of the clad material.

The dark and bright areas of the eutectic region also shows some micro-segregation of importance. The Hf which is rejected by the dendrite with the remaining liquid matrix as has been mentioned before during this eutectic formation the dark area become enriched in Hf (up to $\approx 58 \text{ wt.}\%$) and aluminum ($\approx 9.5 \text{ wt.}\%$), and is depleted of Ni and Cr. The bright region, on the other hand, contains nearly negligible amount of Hf, but is high in Cr ($\approx 31 \text{ wt.}\%$) and Ni ($\approx 60 \text{ wt.}\%$). Further work needs to be done to understand this segregation behavior in this system.

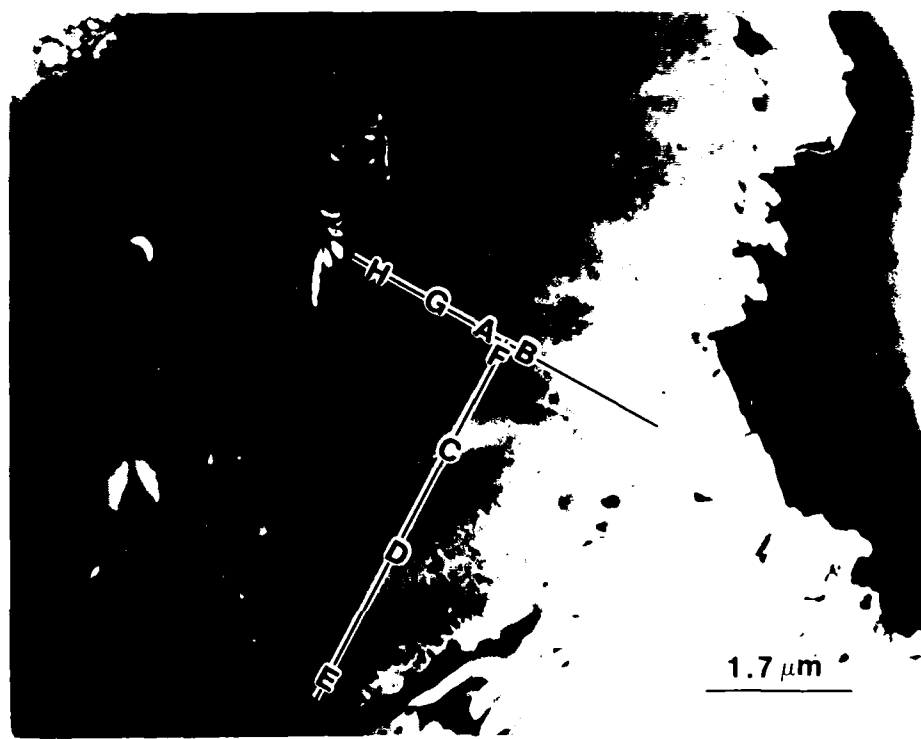


Figure 2.1-36 Dark field STEM image of a dendrite (γ') showing probe positions from where microchemistry results were obtained. Please refer to Table 2.1-9.

Table 2.1-9

Probe Position	Comments	wt. %						at. %					
		Ni	Cr	Al	Hf	Ti	Co	Ni	Cr	Al	Hf	Ti	Co
A	See Fig. 2.1-36	75.5	4.64	4.33	12.56	1.10	1.92	77.4	5.40	9.7	4.24	1.38	1.96
B	See Fig. 2.1-36	72.8	4.56	6.08	13.55	1.01	2.01	73.6	5.20	13.4	4.51	1.25	2.02
C	See Fig. 2.1-36	74.34	4.79	4.22	13.43	1.23	1.98	76.76	5.59	9.49	4.56	1.56	2.04
D	See Fig. 2.1-36	70.49	10.51	5.34	10.40	0.79	2.46	69.91	11.77	11.53	3.39	0.96	2.43
E	See Fig. 2.1-36	63.78	4.54	3.72	24.85	1.23	1.88	72.03	5.79	9.13	9.23	1.71	2.11
F	See Fig. 2.1-36	73.98	4.58	6.08	12.30	1.15	1.91	74.18	5.19	13.26	4.06	1.41	1.91
G	See Fig. 2.1-36	70.92	4.87	6.09	14.87	1.12	2.13	72.32	5.61	13.51	4.99	1.40	2.17
H	See Fig. 2.1-36	64.27	9.57	6.21	16.98	0.74	2.22	66.04	11.11	13.90	5.74	0.94	2.27
L14	Dark area	29.45	1.48	9.62	57.90	0.25	1.30	40.51	2.30	28.79	26.2	0.41	1.79
L15	of eutectic	29.21	1.67	9.40	58.08	0.27	1.37	40.37	2.61	28.28	26.4	0.46	1.88
L16	Bright area	59.83	30.97	5.61	0.01	0.68	2.89	54.03	31.58	11.03	0.00	0.76	2.60
L17	of eutectic	59.69	30.83	5.26	1.08	--	3.14	54.54	31.81	10.47	0.32	--	2.85

DTA

Some differential thermal analysis work has been done on the substrate material (Rene 80) and the clad material. Preliminary results indicate that the γ' dissolution temperatures for the substrate and the cladding are very comparable. Further composition optimization needs to be done in order to enhance the γ' dissolution temperature of the clad material as compared to the substrate. Figures 2.1-37 and 2.1-38 are the two DTA runs for the substrate material and the clad material (sample L), respectively. Both the samples show two distinct endothermic peaks as is typical for nickel base superalloys.

At present, we are in the process of testing the γ' transformation temperature of clad materials for different composition and different laser processing parameters. These results will be presented in the next report.

2.2 OXIDATION PROPERTIES

2.2.1 EXPERIMENTAL PROCEDURE

Thermogravimetric Analysis (TGA)

Oxidation resistance of the claddings and the substrate was measured using a Perkin-Elmer TGA-7 analyzer with computerized system control and data acquisition capability (Fig. 2.2-1). The change in the mass of the sample is measured dynamically as a function of oxidation time. The analyzer itself during operation consists of a furnace surrounding a Pt sample pan suspended from a microbalance by a Pt wire. Samples are stood up on their width and held in place between two Pt retaining wires. 0.3 ml/s of dry air flows past the sample and 0.6 ml/s of Ar is used to protect the microbalance during operation. The sample is heated from ambient at 100°C/min to 1200°C and held at 1200°C for 8 hours. In situ cooling is then performed at a rate of 10°C/min to 950°C before cooling to ambient at a rate of 25°C/min.

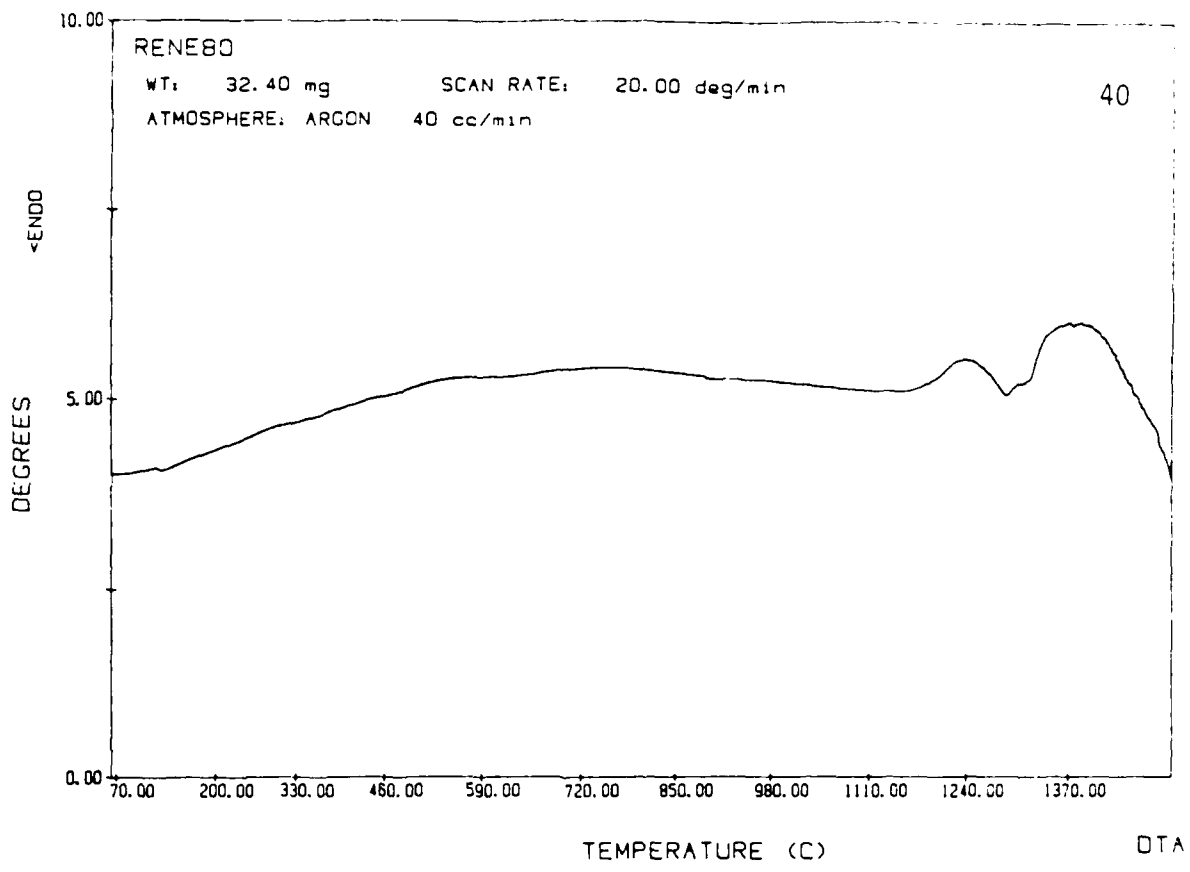


Figure 2.1-37 DTA trace for substrate sample (Rene 80) up to 1500°C at 20°C/minute.

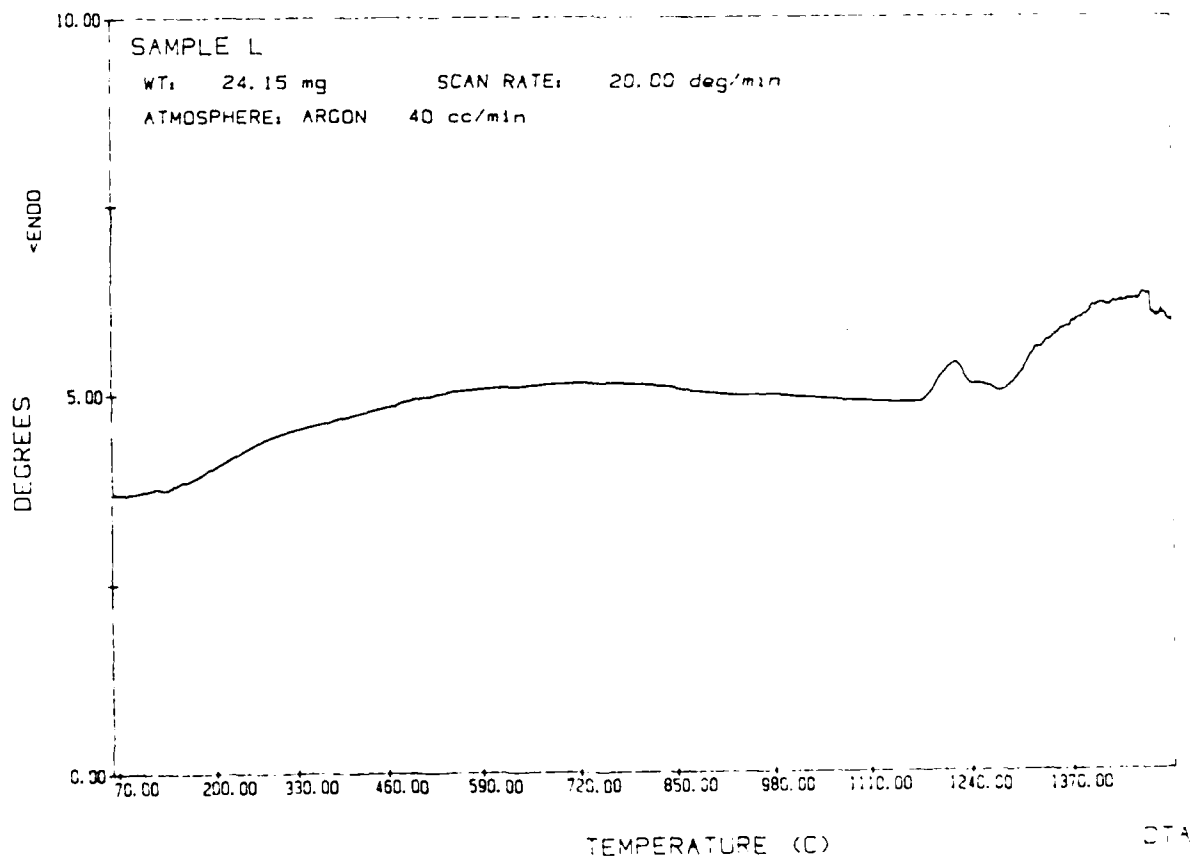


Figure 2.1-38 DTA trace for cladding (sample L) up to 1500°C and 20°C/minute.

The samples are sectioned from the cladding using a low speed saw with a SiN blade (Fig. 2.2-2). Following sectioning, all of the faces of the sample are progressively abraded through 600 grit using SiC paper with water as the lubricant. The dimensions of the samples are measured with caliper and micrometer prior to a final cleaning with (1) acetone and (2) trichloroethane. Some variation in the sample dimensions was required to test all of the claddings.

Laser process parameters and alloy powder and substrate composition are given in Table 2.2-1. Samples J, K, L1, and L2 will be referred to as the "70-7-3-20" series and samples 2RE1, 2RE3B, and 2RE5 will be designated as the "58-26-4-12" series based upon their respective powder compositions.

Auger Electron Spectroscopy (AES) and Optical Microscopy

The surfaces and cross sections of the TGA samples were examined using the Physical Electronics model 595 Auger Microprobe of the Materials Research Laboratory (MRL) at UIUC. The surface of an as-oxidized broad face is scanned both to prior and after approximately 10 minutes of sputtering with Ar ions at 3 kV. A cross section was taken perpendicular to the cladding direction at a distance of 1 1/4 mm from one end of the oxidized sample. (A sputtering time of 30 minutes at 3 kV was required to clean the cross-sectional samples because of the presence of the epoxy mounting material.) The amplitude of the counting peak for a characteristic electron energy is proportional to the concentration of the corresponding element. By dividing the amplitude by the appropriate sensitivity factor, the relative amounts of different element can be found. Photomicrographs of the entire cross section exposed were taken on an optical microscope at 250x to allow measurement of the thickness of unoxidized material.

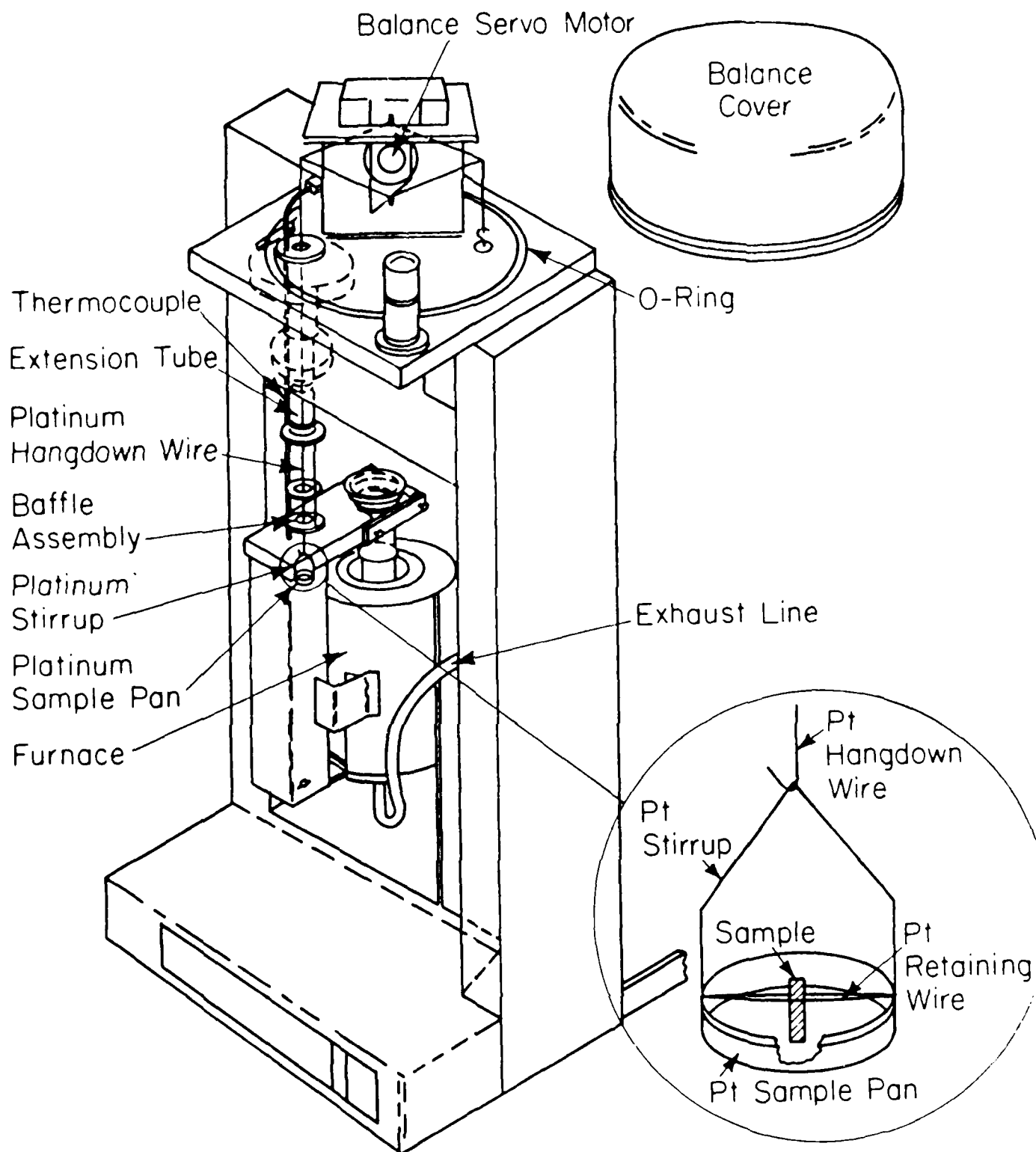


Figure 2.2-1 TGA-7 Schematic (Furnace Positioned for Clarity)

Table 2.2-1
Powder Composition by Atomic Percent

Sample	Ni	Cr	Hf	Al	Laser Power (kW)	Traverse Speed (mm/s)
J	70	7	3	20	5	19
K	70	7	3	20	7	19
L1	70	7	3	20	8.75	19
L2	70	7	3	20	8.75	19
2RE1	58	26	4	12	7	19
2RE1	58	26	4	12	7	25
2RE5	58	26	4	12	7	15

Rene 80 Substrate: (w/o)

C	Cr	Co	Mo	W	Ti	Al	Zr	B	Ni
.16	14	9.5	4	3.8	5.00	3.00	.03 Max	.015 Max	BAL

(Nominal Composition) a/o (Approx.)

C	Cr	Co	Mo	W	Ti	Al	Zr	B	Ni
.76	15.4	9.2	2.4	1.2	6.0	6.3	.02	.08	58.8

2.2.2 RESULTS

TGA

The plot of sample mass per unit sample surface area as a function of oxidizing time for the 58-26-4-12 claddings and the substrate are shown in Fig. 2.2-3. All of these cladding samples gain mass at a faster rate than those of the substrate after three hours of oxidation time. The mass of the cladding sample increases at a nearly linear rate during the last four hours while the mass of the substrate sample appears to level off.

A similar plot in Fig. 2.2-4 shows that the 70-7-3-20 samples gain mass at a lower rate than the substrate throughout the test period. The slopes for the claddings J, L1, and L2 are nearly zero after two hours. In fact the mass gains recorded during that period are at the limit of the resolution of the microbalance, 1 μg .

One result of the combination of a 1200°C testing temperature and the use of Pt suspension wires and sample pans is PtO_2 volatilization [6,7]. Two runs were made using the standard cycle of 8 hours at 1200°C without any sample, one of which is represented in Fig. 2.2-5. In both cases, the weight loss was a linear function of oxidizing time. In addition, the empty weight of the suspension wire and sample pan was recorded before and after six of the runs involving a cladding or substrate sample. Figures 2.2-6 and 2.2-7 correspond to Figs. 2.2-3 and 2.2-4, respectively, adjusted for the net empty weight loss (assumed linear with time) measured for each sample. The most important effect of this adjustment is that the mass gains of the 70-7-3-20 samples as adjusted are nearly linear with time after 3 hours instead of approaching zero as unadjusted. The weight gains are still lowest for the 70-7-3-20 samples and highest for the 58-26-4-12 samples.

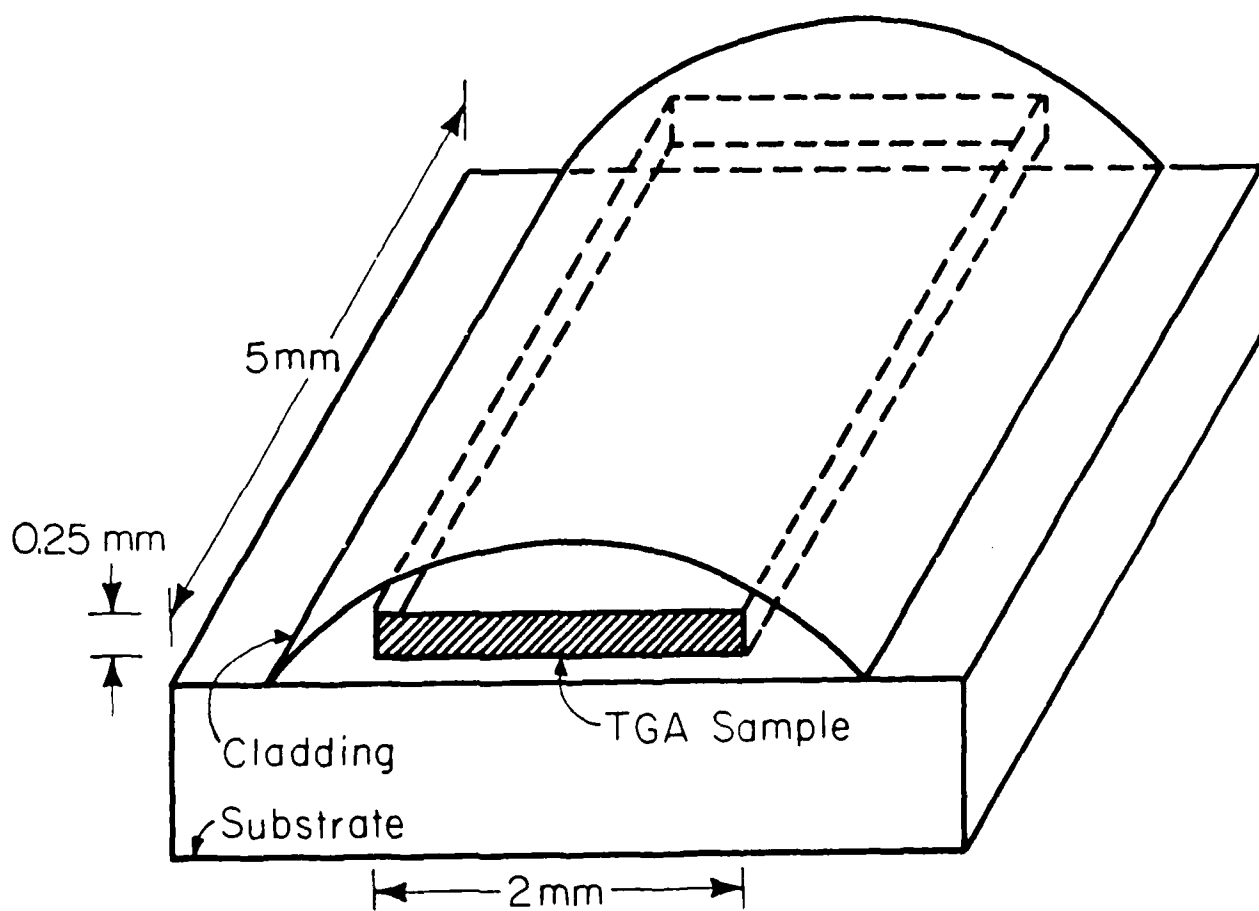


Figure 2.2-2 Sample Schematic

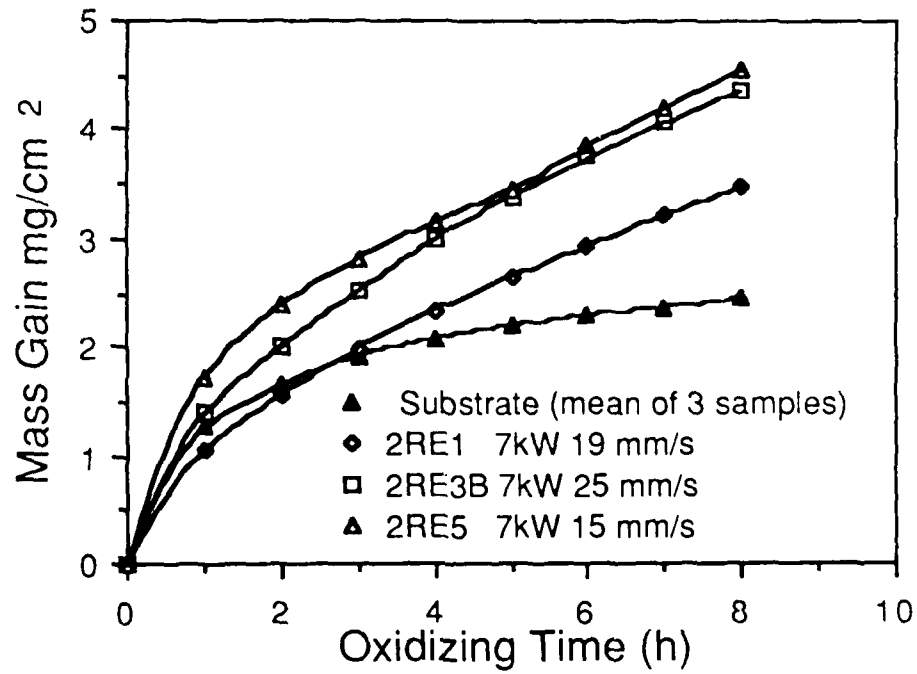


Figure 2.2-3 TGA Mass Gain as a Function of Oxidizing Time for 58-26-4-12 Claddings and the Substrate

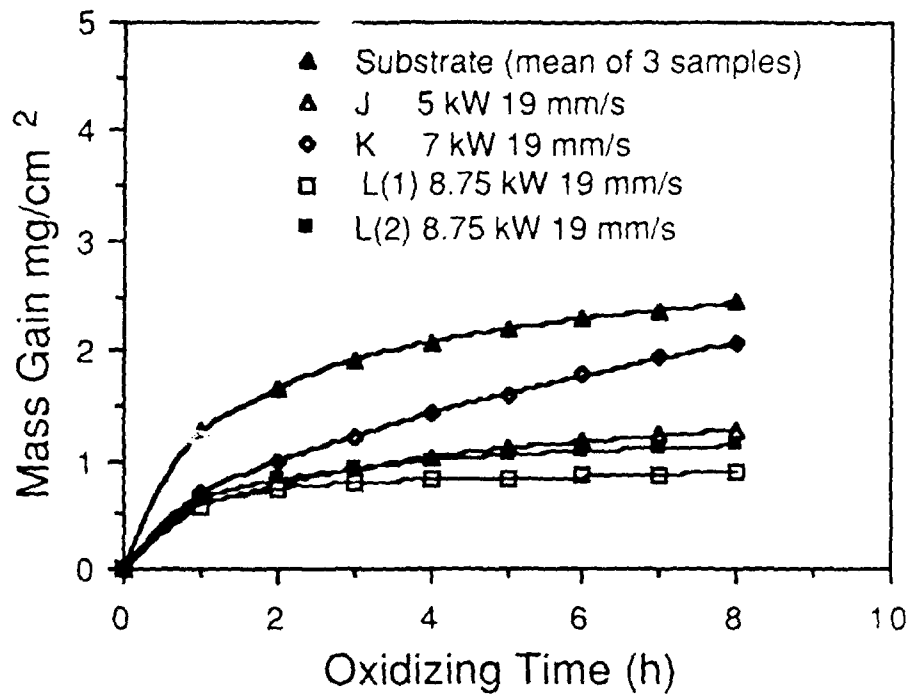


Figure 2.2-4 TGA Mass Gain as a Function of Oxidizing Time for 70-7-3-20 Claddings and the Substrate

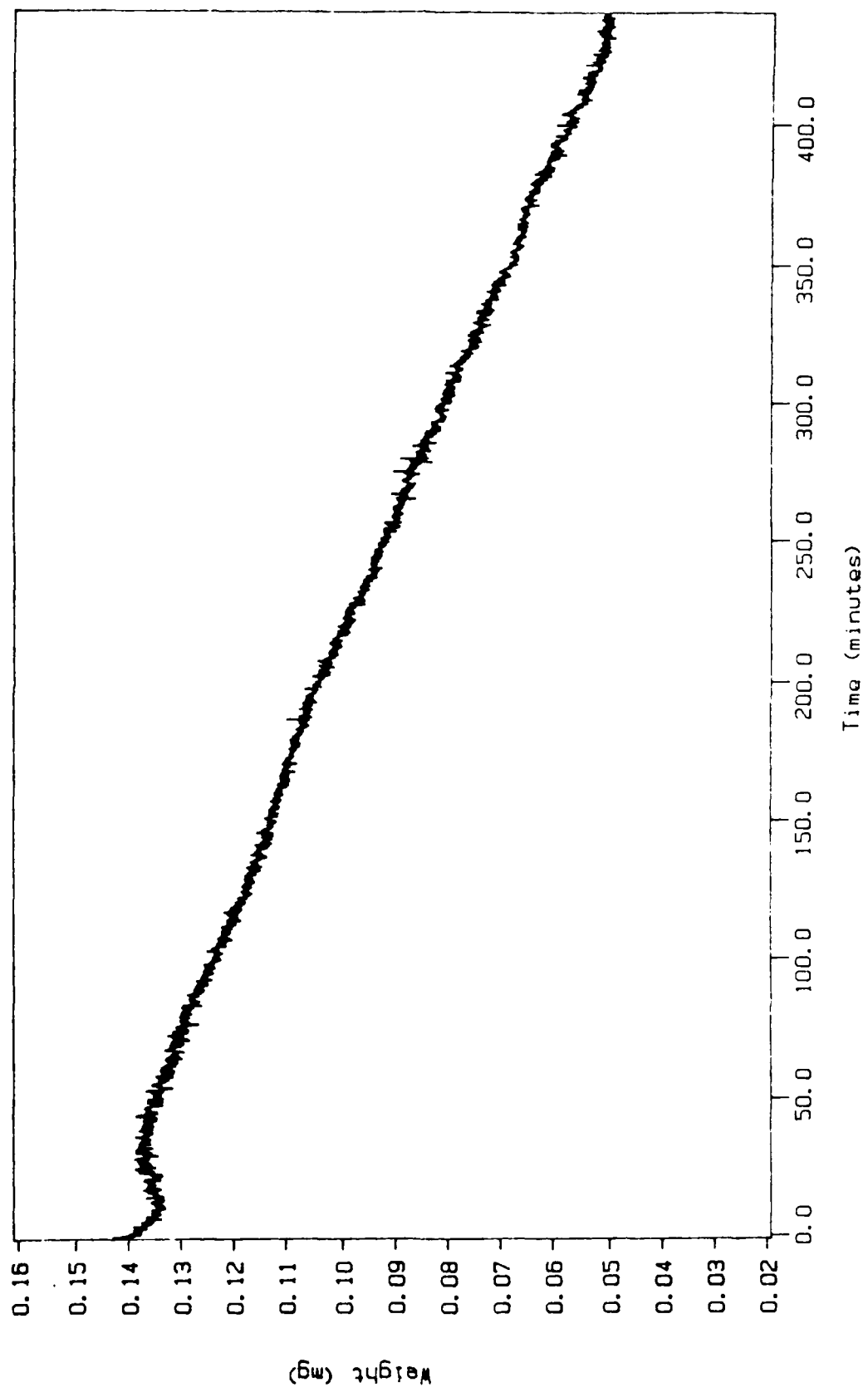


Figure 2.2-5 Measured Empty Weight as a Function of Time at 1200°C

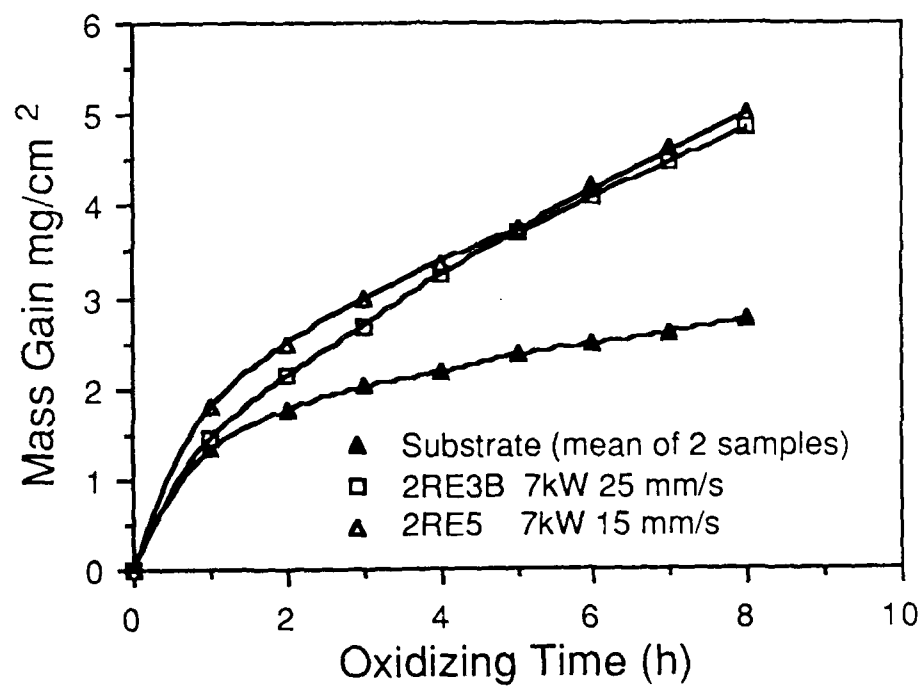


Figure 2.2-6 TGA Mass Gain as a Function of Oxidizing Time for 58-26-4-12 Claddings and the Substrate - Adjusted for Net Empty Weight Loss

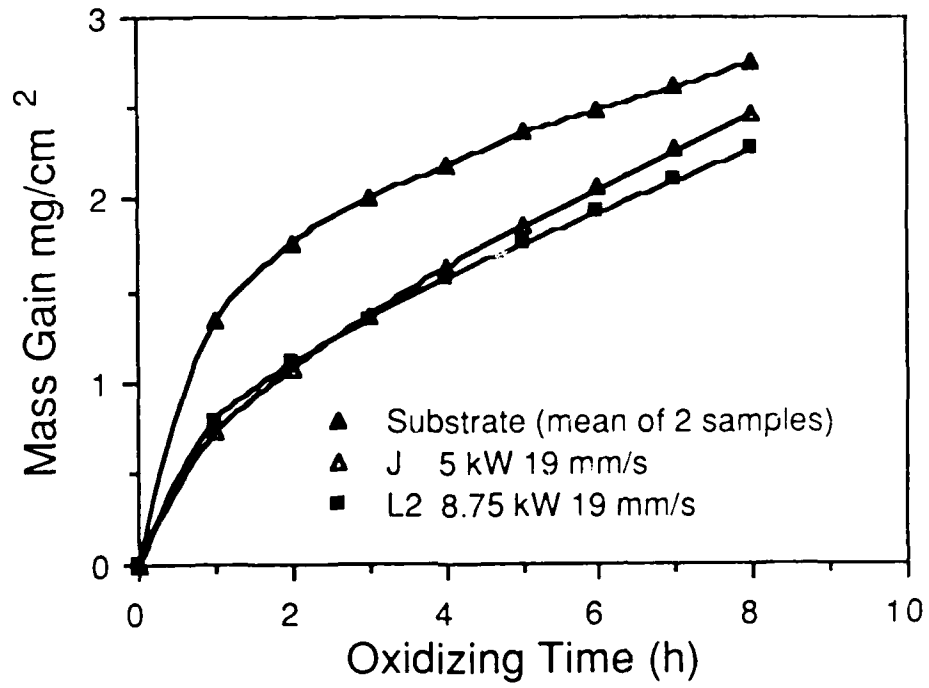


Figure 2.2-7 TGA Mass Gain as a Function of Oxidizing Time for 70-7-3-20 Claddings and the Substrate - Adjusted for Net Empty Weight Loss

Measurement of Thickness of Unoxidized Sample

Three typical optical photomicrographs of cross-sections of as-oxidized samples are shown in Figs. 2.2-8 through 2.2-10. The substrate sample of Fig. 2.2-8 has a nearly planar metal-oxide interface while the samples of Figs. 2.2-9 and 2.2-10 have irregular interfaces. All 3 of the 58-26-4-12 samples contain a series of cracks whose length runs in the vertical direction during cladding. The presence of heavy oxide layers along the length of at least some of the cracks indicates that the cracks were formed prior to oxidation or soon after the beginning of oxidation. No cracks were observed in the samples from the 70-7-3-20 claddings nor from the substrate.

The sharp contrast between the oxides and the unoxidized alloy in an unetched cross-sectional specimen provides another means of measuring oxidation resistance. The thickness of unoxidized alloy in the sample (short dimension in Figs. 2.2-8 through 2.2-10) was measured at 0.4 mm intervals using the optical photomicrographs and compared to the original thickness of the sample as measured with a micrometer (Table 2.2-2). Both sets of cladding samples lost less metal to oxidation than the substrate sample based upon thickness with the 70-7-3-20 samples losing the least of the 3.

AES

The plot of the frequency of counts as a function of electron energy gives a relative measure of composition. Typical surveys for the surfaces of a substrate sample and 2 cladding samples are shown in Figs. 2.2-11 through 2.2-13. The results of correcting the magnitudes with the appropriate sensitivity factors are shown in Table 2.2-3.

Figure 2.2-8 Optical Photo micrograph
of Cross-section of Oxidized Substrate,
Unetched (Original at 250x)



Figure 2.2-9 Optical Photo micrograph

of Cross-section of Oxidized 2RE1
(58-26-4-12), Unetched (Original at 250x)

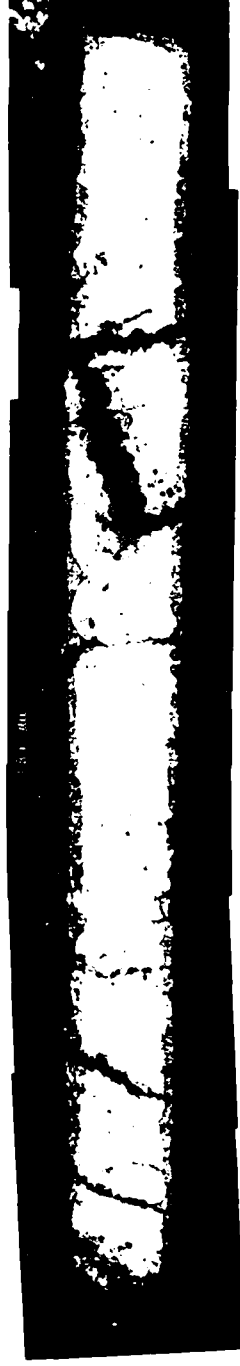


Figure 2.2-10 Optical Photo micrograph of

Cross-section of Oxidized Sample "K"

(70-7-3-20), Unetched (Original at 250x)



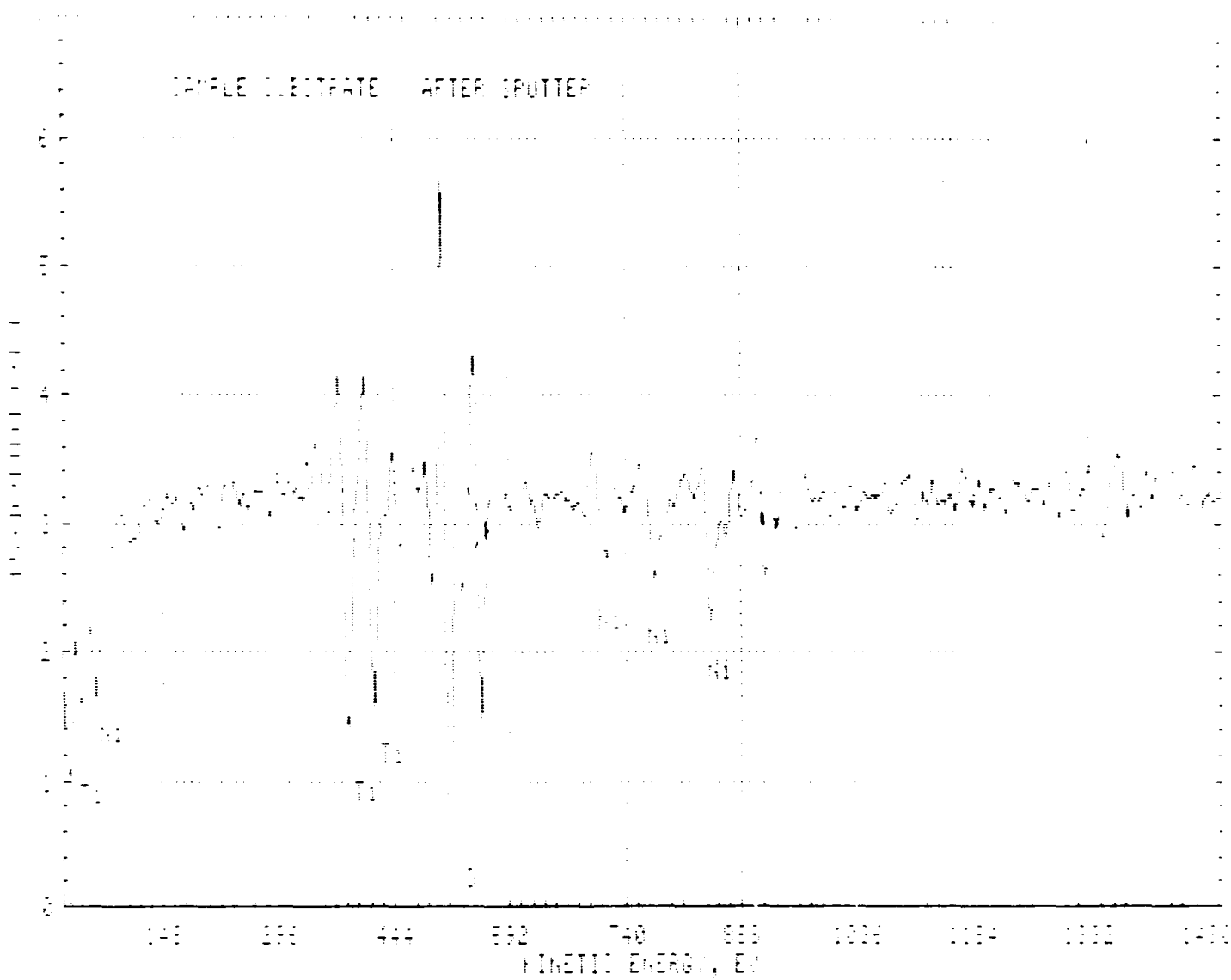


Figure 2.2-11 AES Survey of Substrate Surface

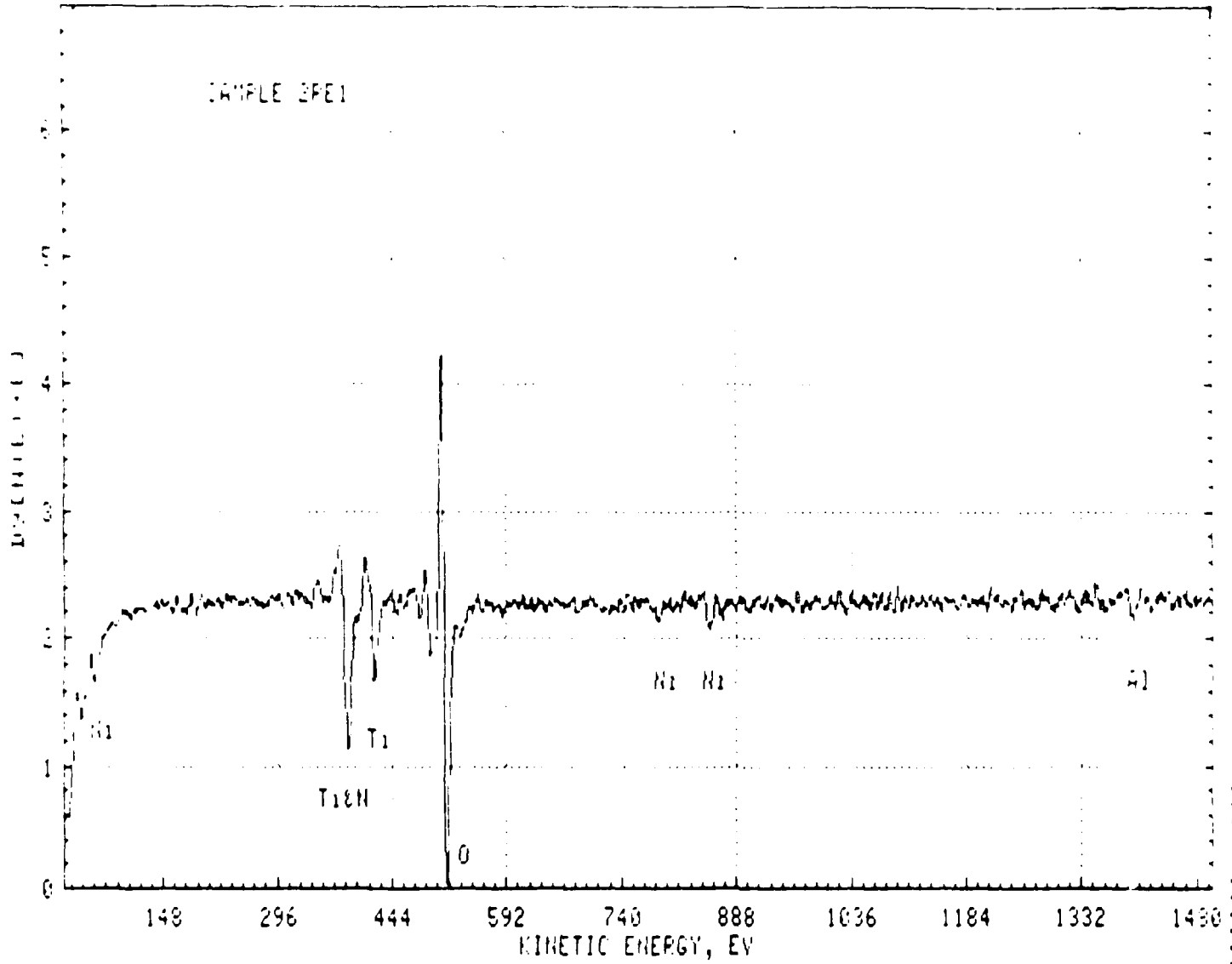


Figure 2.2-12 AES Survey of 2RE1 (58-26-4-12) Surface

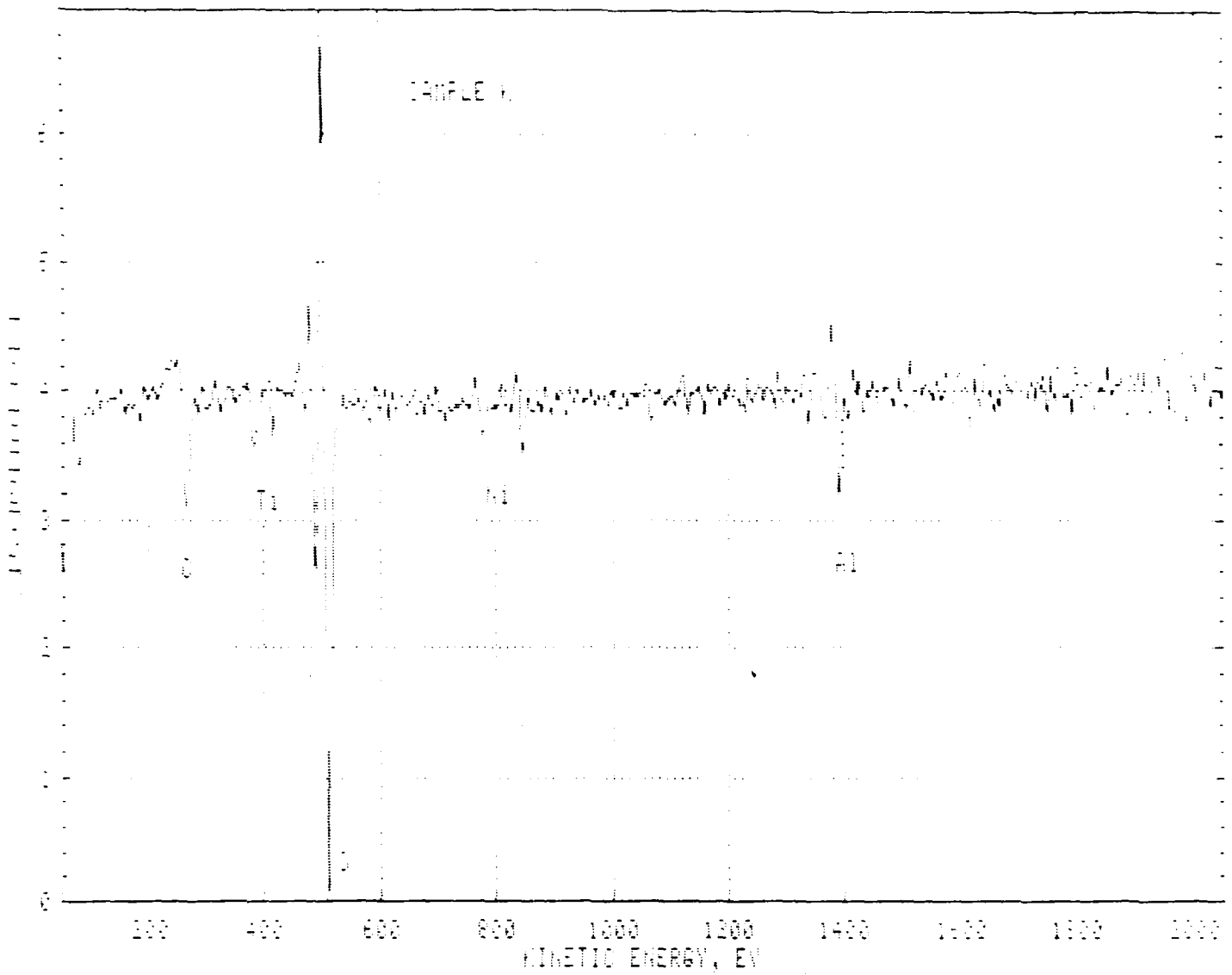


Figure 2.2-13 AES Survey of Surface of "K" (70-7-3-20)

Table 2.2-2
Comparison of Unoxidized Sample Thickness
with Original Sample Thickness

Sample	No. Measures	Original Thickness (mm)	Mean Unoxidized Thickness (mm)	Metal Loss (mm)
2RE1	4	.18	.14	.04
2RE3B	4	.22	.18	.04
2RE5	5	.13	.081	.05
Substrate	5	.21	.12	.09
K	3	.36	.33	.03
L1	3	.25	.23	.02

(Readings taken at 0.4 mm intervals except L1 where the interval used was 0.1 mm due to smaller sample dimensions.)

Table 2.2-3
 Magnitude of Auger Electron Characteristic Energies of
 as Oxidized Surfaces Adjusted for Sensitivity After Sputtering

Sample	KV	Al	C	Cr	Ni	O	Ti	Ti+N
K (side 1)	5	510			31.5	354	51.2	
K (side 2)	5	401	58.6		34.1	259	18.8	
L	3	591			34.4	249		
2RE1(A)	5	101		71.9	206	224	103	173
2RE1(B)	5			71.3	186	186	18.8	35.1
2RE1(C)	5	82.9			23.3	217	57.9	135
2RE3B(A)	5				212	240	33.8	
2RE3B(B)	5				179	258	68.8	158
2RE5	5				116		62.9	
SUBSTRATE	5				92.6	289	157	

A, B, C different map locations on surface of sample

The surfaces of the 58-26-4-12 samples all contain significant amounts of Ni and Ti and some also contain Cr. The 70-7-3-20 samples are high in Al and contain smaller amounts of Ni and Ti. Note that no Ti is present in the alloying powder while the substrate contains 5 weight percent Ti as shown in Table 2.2-1.

The appearance of two microstructural constituents on the as-oxidized surface of the substrate sample shown in Fig. 2.2-14 is related to a sharp partitioning of alloying elements. The elemental maps shown in Fig. 2.2-15 indicate that the raised oval mounds in Fig. 2.2-14 are of very high Ni and O content while the surrounding matrix consists mostly of Ti and O. No other alloying elements were found in significant amounts as predicted by Fig. 2.2-11.

The surfaces of the oxidized 58-26-4-12 samples are also divided into 2 distinct regions (Fig. 2.2-16). The primary alloying element in the bright region in the center of the images in Fig. 2.2-16 is Ti (Fig. 2.2-17) while the darker region contains Ni and Cr which also tend to partition from each other.

In all cases, very little Hf was found on the surface. The relatively high atomic number of Hf, 72, allows for only a very low yield of Auger electrons, but the amount of Hf on the surface is still probably very small.

As suggested by the scan in Fig. 2.2-13, the oxidized surfaces of 70-7-3-20 claddings consisted primarily of Al and O. The SEI photomicrograph shown in Fig. 2.2-18 (taken at the same magnification as Figs. 2.2-14 and 2.2-16) reveals a much more uniform morphology than those of the 58-26-4-12 and substrate samples.

Examination of a transverse cross-section of the oxidized substrate sample reveals the chemical composition and morphology of the various oxide

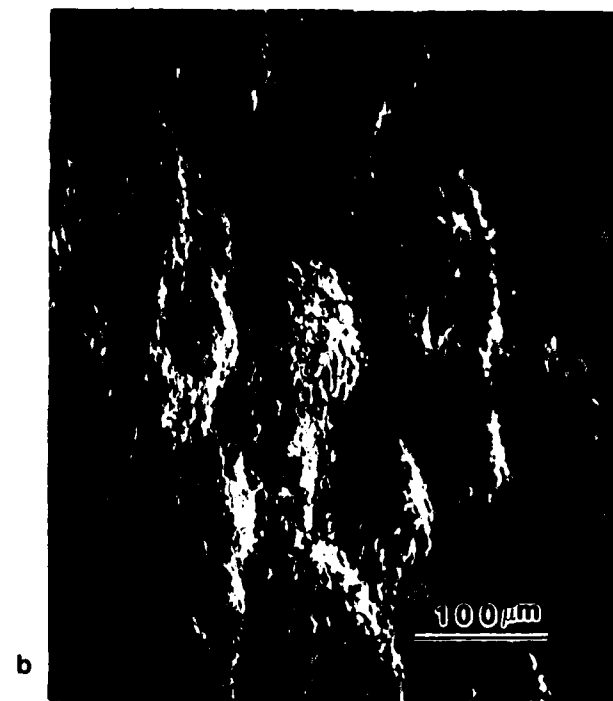


Figure 2.2-14 (a) Secondary Electron Image
(b) Absorbed Image
of Surface of Oxidized Substrate at 204x

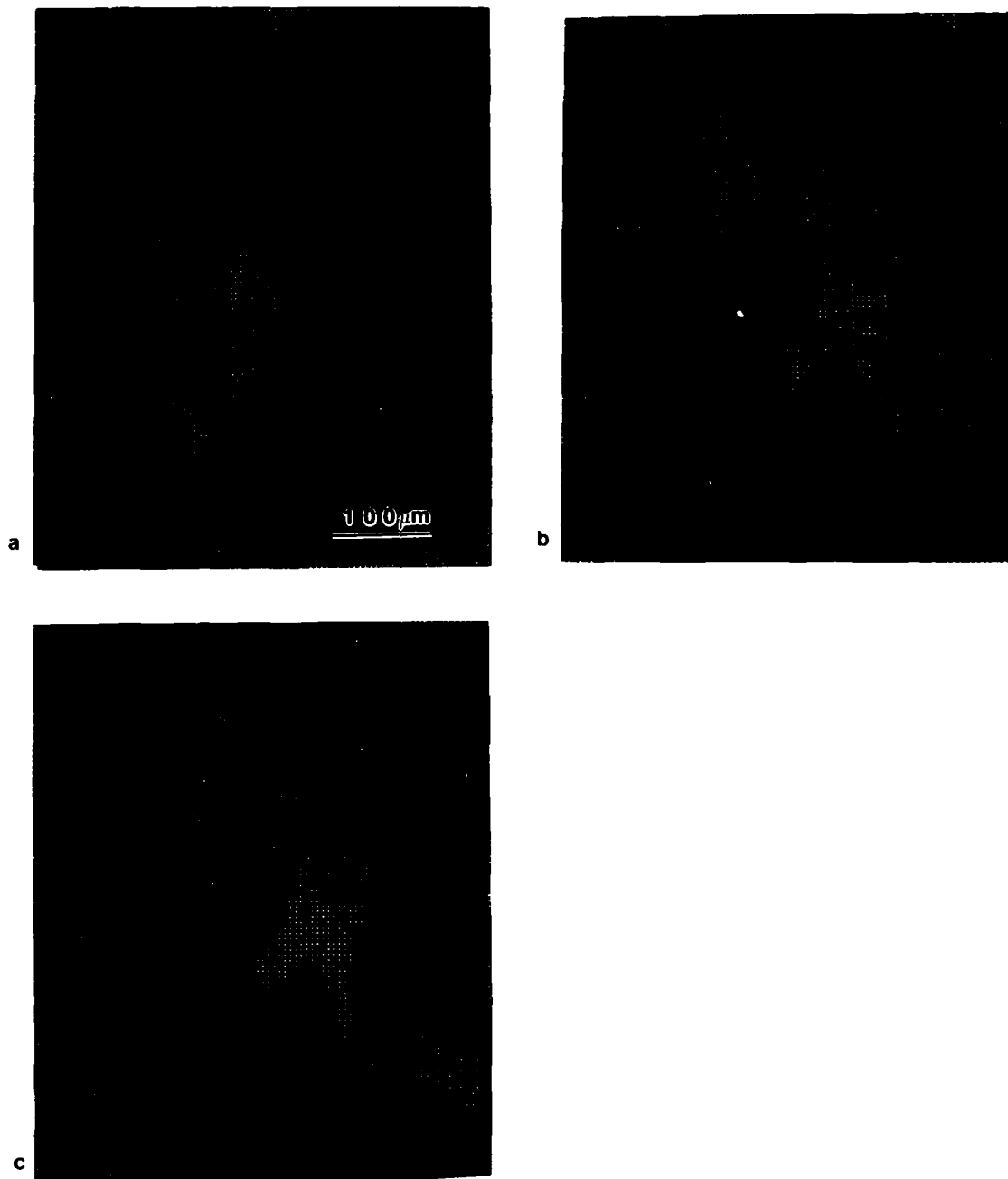


Figure 2.2-15 Elemental Maps of Surface of Oxidized Substrate
(Same Field as Figure 14) 210.
(a) Ni, (b) Ti, (c)

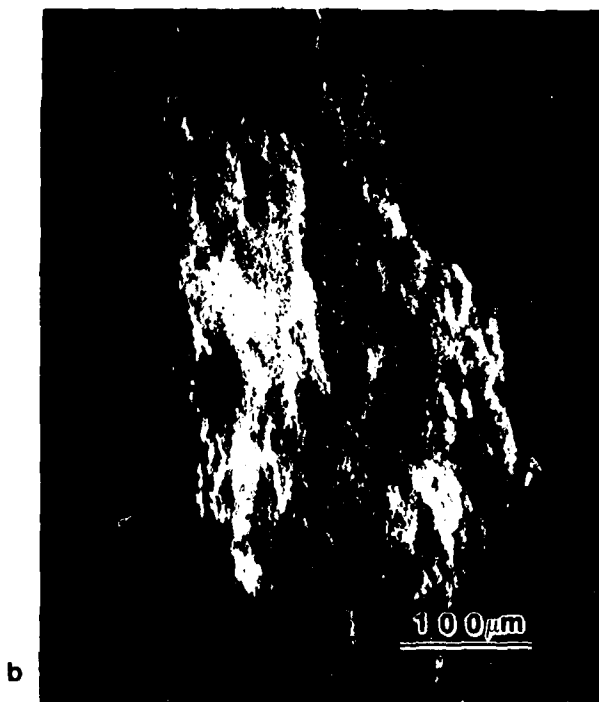
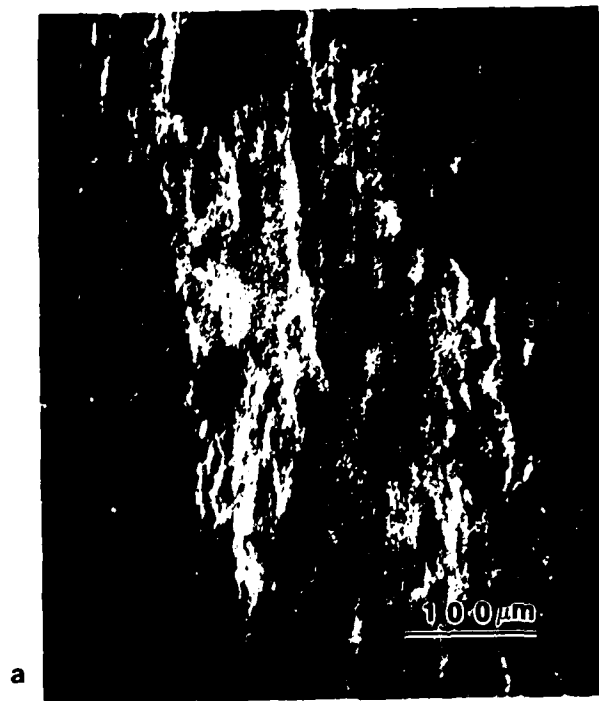


Figure 2.2-16 (a) SEI and (b) ABS
Images of Surface of Oxidized 2RF1 (58-26-4-12) 204x

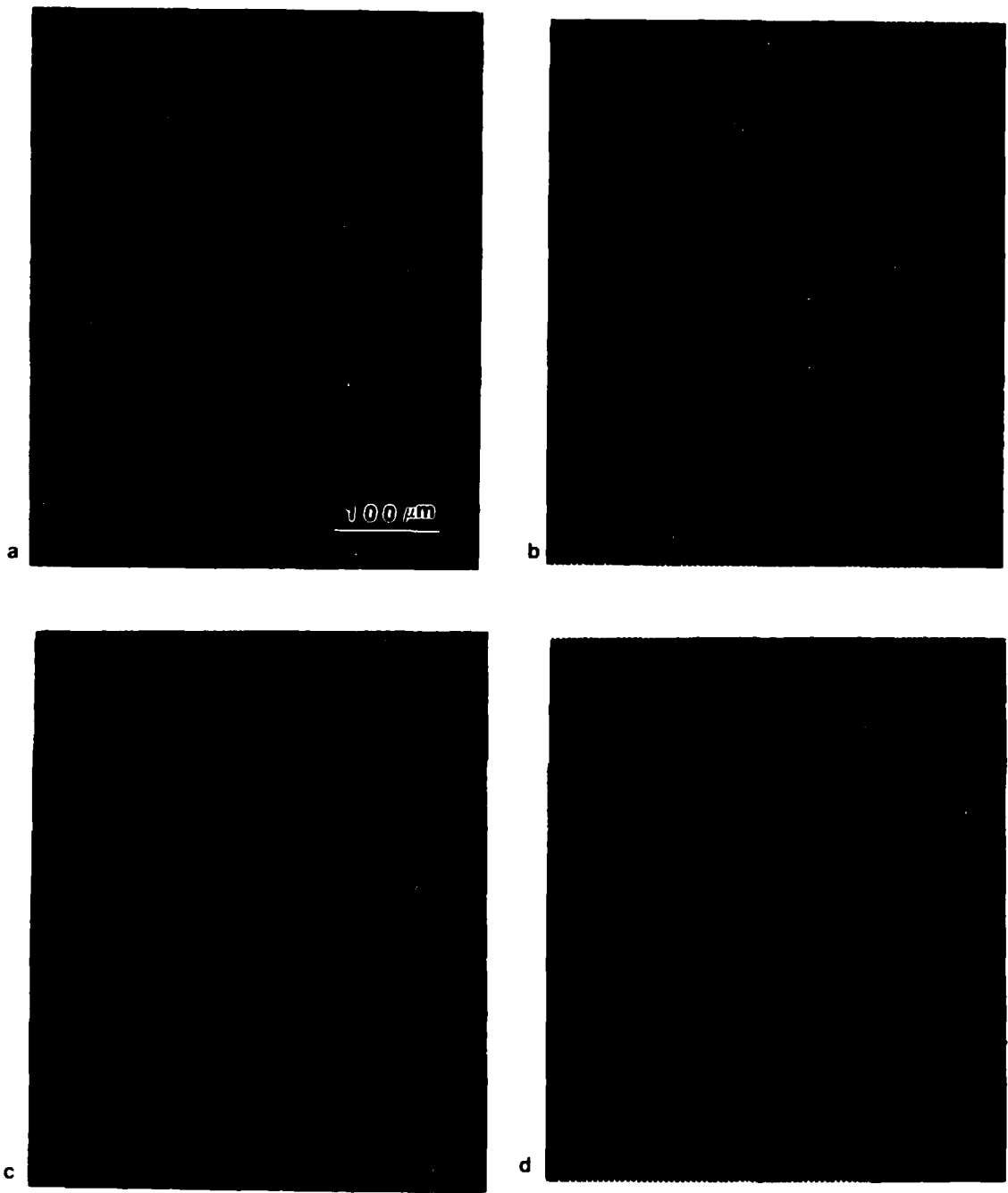


Figure 2.2-17 Elemental Maps of Surface of Inconel 281
(58-26-4-12), Same Field as Figure 16
(a) Ni, (b) Ti, (c) Cr, (d) O

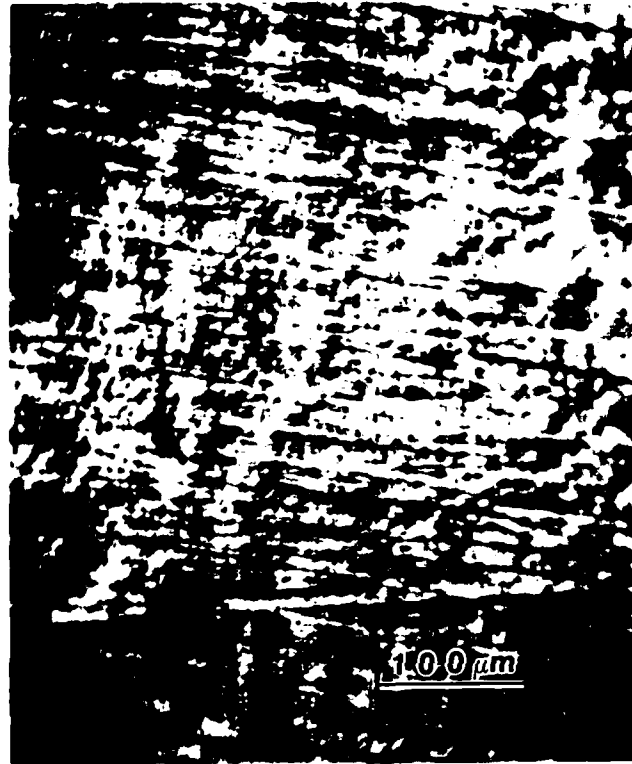


Figure 2.2-18 SEI Image of Surface of Oxidized K (70-7-3-20) 204x

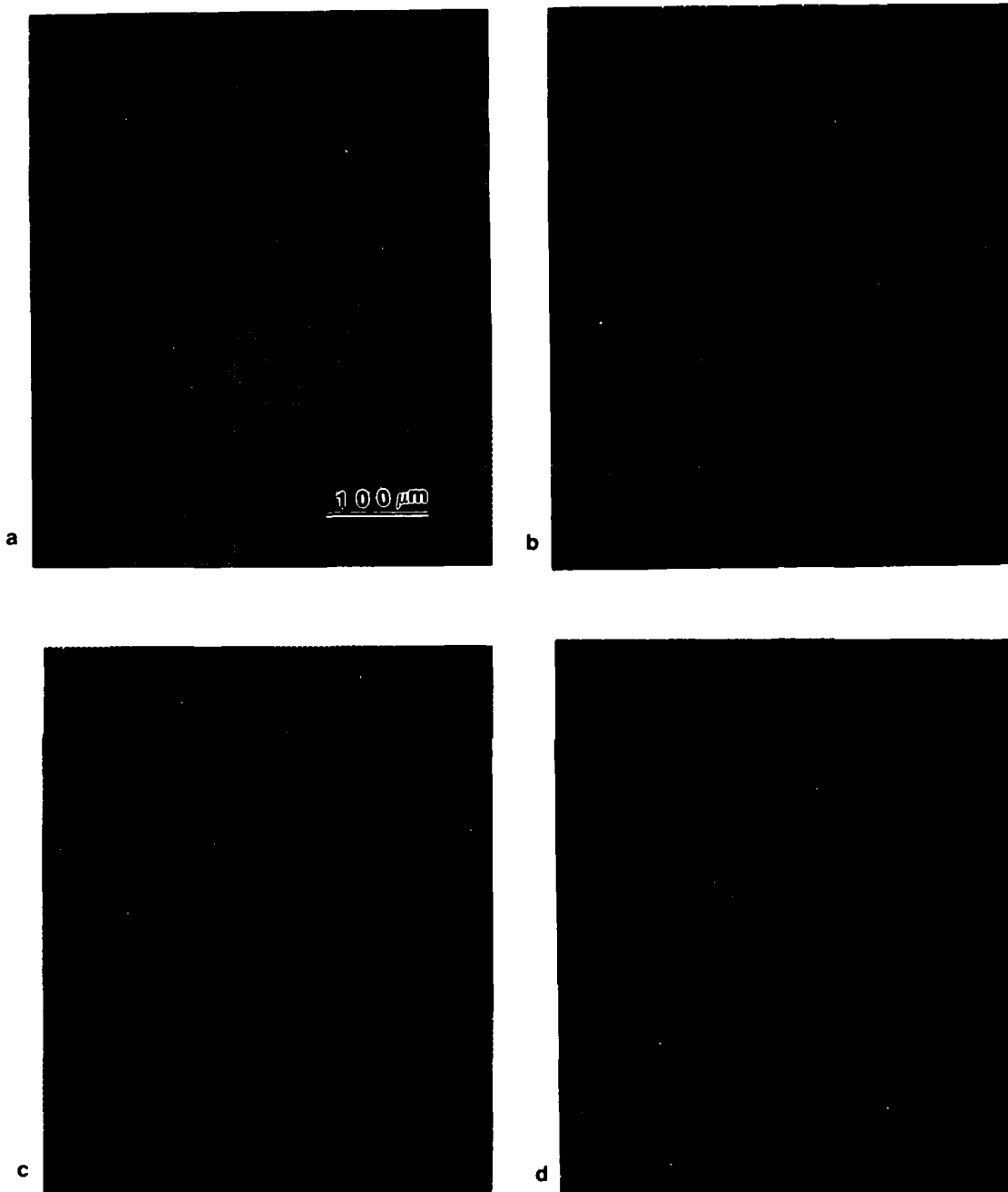


Figure 2.2-19 Elemental Maps of Surface of Oxidized K (70-7-3-20)
Same Field as Figure 18
(a) Al, (b) Ni, (c) O, (d) Ti

layers formed (Fig. 2.2-20). The outermost oxide layer in Fig. 2.2-20, 1, contains some Ti while the next oxide layer, 2, is very high in Cr (Fig. 2.2-21). Within the region containing both oxide and the base alloy, layer 3, Ni replaces Cr as the main alloying element. The base alloy itself is primarily Ni with some Cr and Ti present. Located within the matrix near its interface with the oxide layer are dark rods, 4, approximately 40 μm long, which are perpendicular to the surface of the sample. These rods are high in Ti.

The appearance of a cross-sectional photomicrograph of 2RE1 (58-26-4-12) is similar to that of the substrate, but the chemical composition of the oxide layers is different. Figure 2.2-22 displays a continuous outermost layer, 1, of oxide. Below this layer is a subscale layer, 2, intermingled with the unoxidized alloy, 3. As shown in Fig. 2.2-23, oxide layer 1 is very high in Cr while oxide layer 2 is mostly Al. The trail of aluminum oxide subscale in the right central portion of Fig. 2.2-22a extends more than a quarter of a millimeter beyond the surface of the sample.

These appendages apparently correspond to those seen around the entire perimeter of the cross-section of the sample in Fig. 2.2-9. Ti appears at random throughout the metal matrix and oxide layers while Hf is present at random in the metal matrix but is absent from the oxide layers.

The samples from 70-7-3-20 claddings tend to have more Al in the surface oxide layer (Figs. 2.2-24 and 2.2-25). While the layer of aluminum oxide is not completely continuous at the surface in Fig. 2.2-24a, the region of highest aluminum content is more sharply defined and nearer the sample surface than in the 58-26-4-12 samples. The Cr map of Fig. 2.2-24b is more uniform than that from the 58-26-4-12 sample shown in Fig. 2.2-22b. Hf and Ti were not found in any appreciable amount in the fields examined from 70-7-3-20 samples.

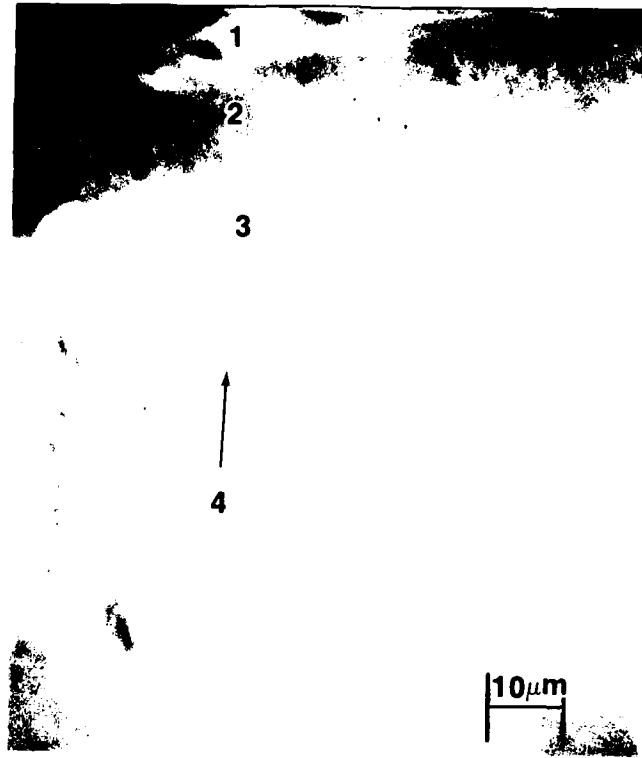


Figure 2.2-20 Absorbed Image of Cross-section of Oxidized Substrate (1000x)

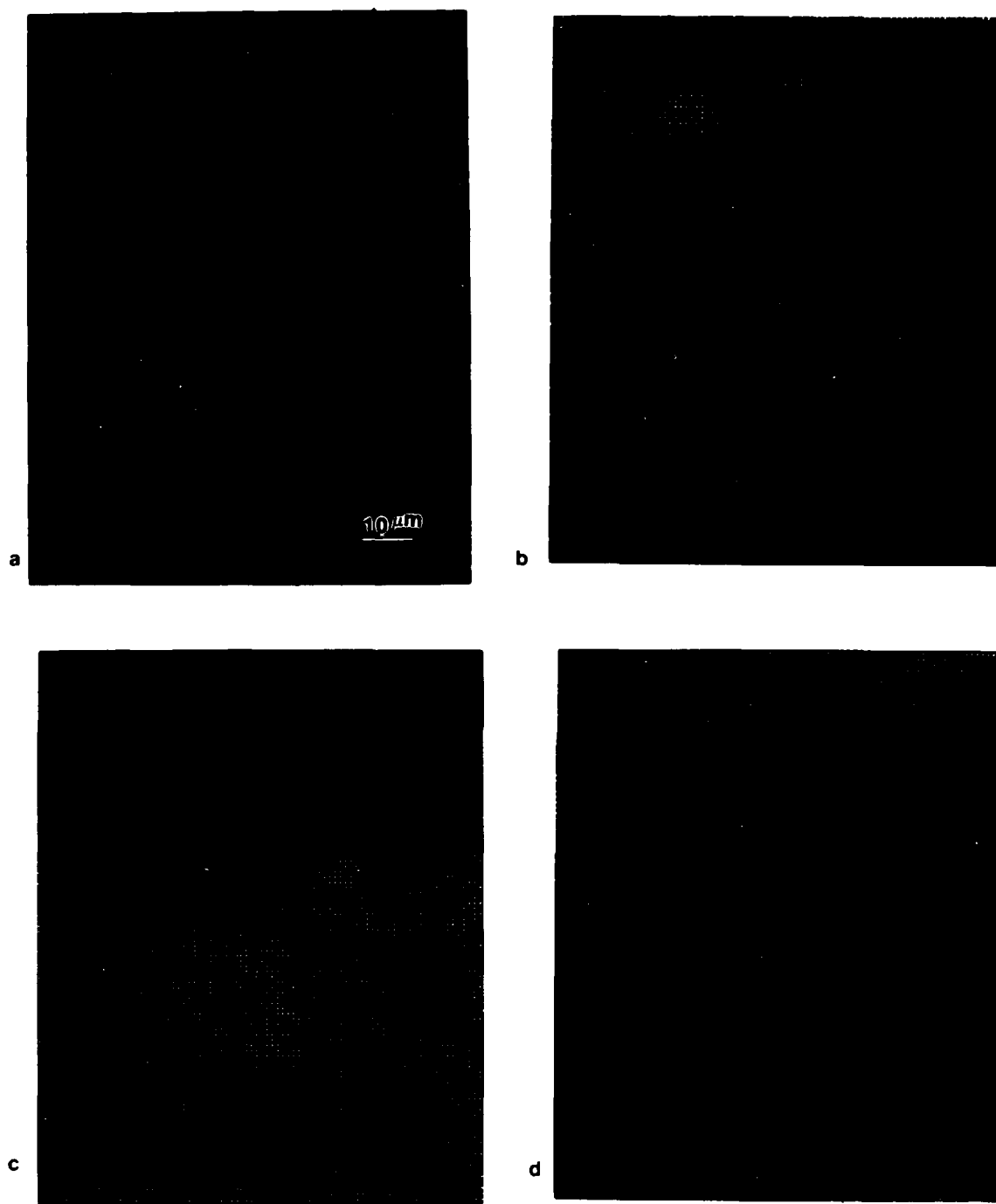


Figure 2.2-21 Elemental Maps of Cross-section of Oxidized Substrate
(Same Field as Figure 20)
(a) Al, (b) Cr, (c) Ni, (d) O

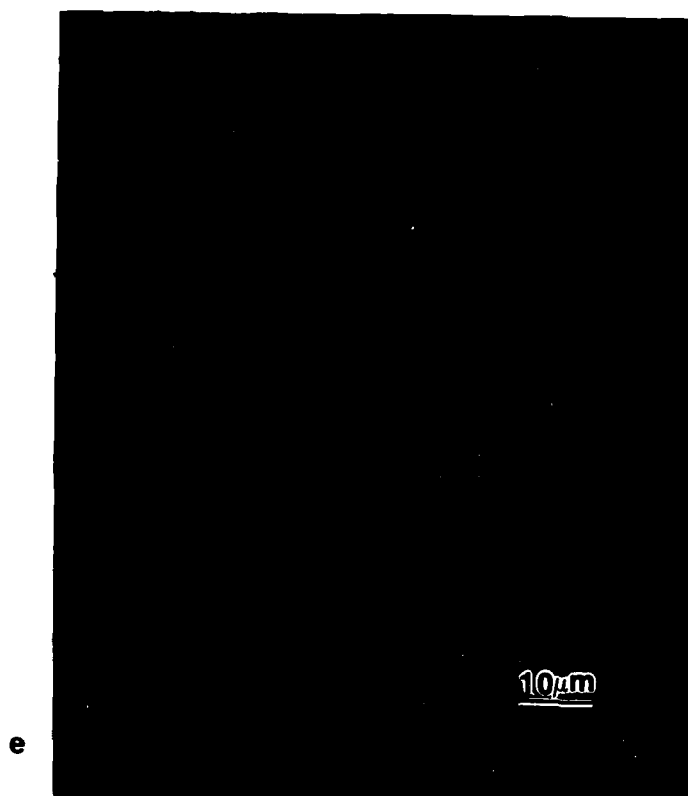


Figure 2.2-21 Elemental Maps of Cross-section of Oxidized Substrate
(Same Field as Figure 20), (e) Ti

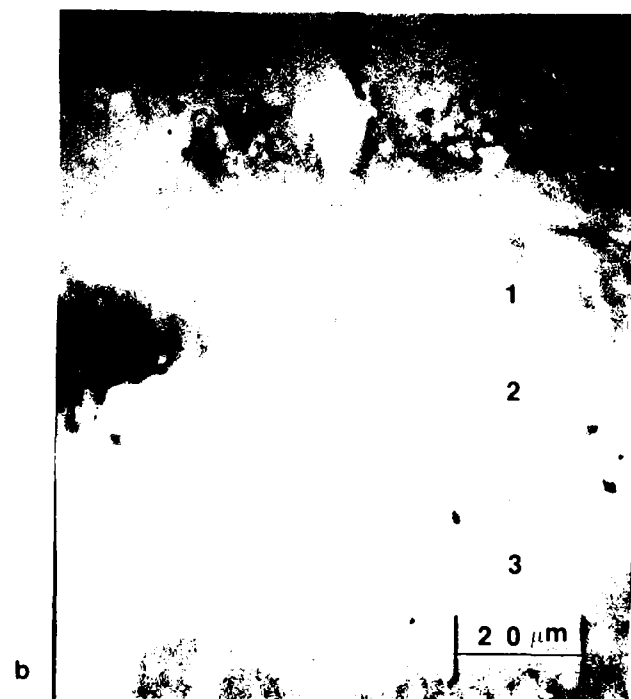
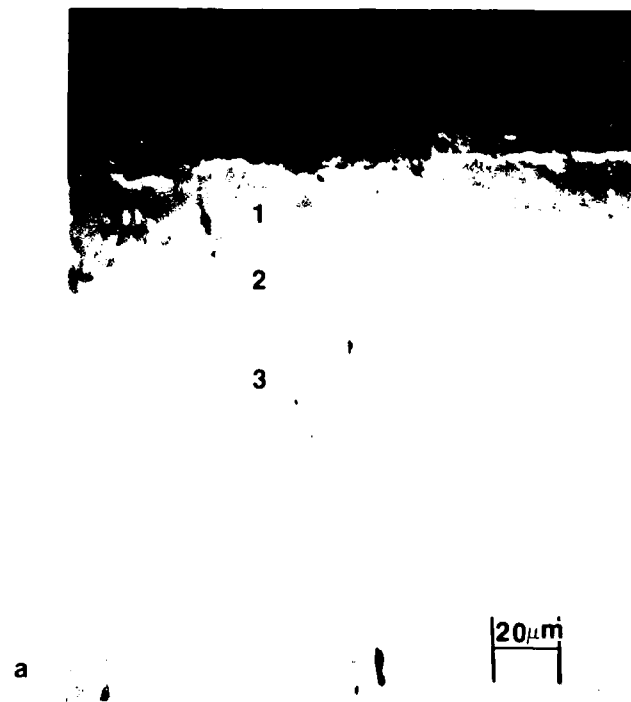


Figure 2.2 22 SE Image of Cross section of Oxidized PBE1 (58 26 1 12)
(a) 500x, (b) 1000x

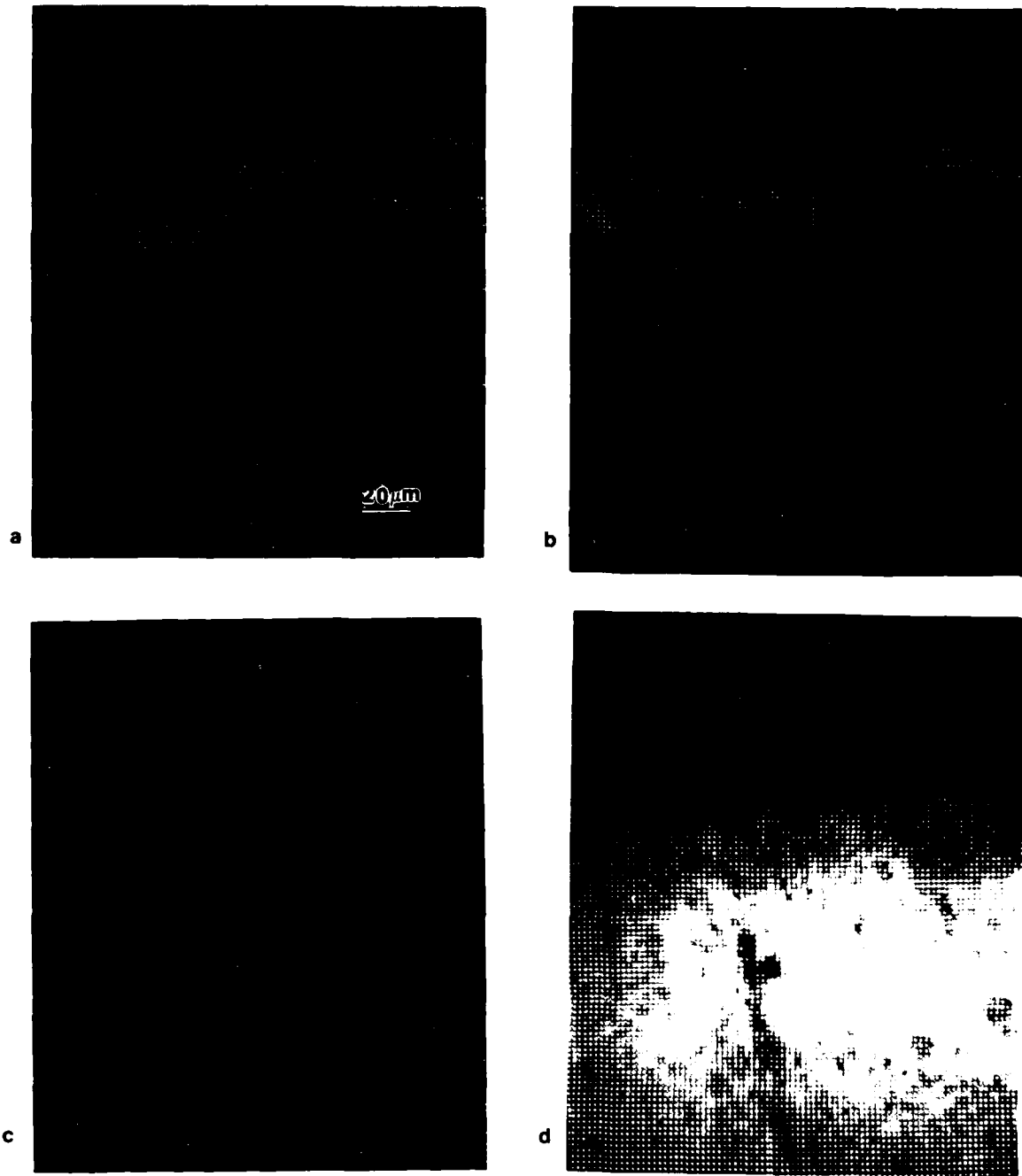


Figure 2.2-23 Elemental Maps of Cross-section of Oxidized 2RE1 (58-26.4-12)
Same Field as Figure 22a
(a) Al, (b) Cr, (c) Hf, (d) Ni

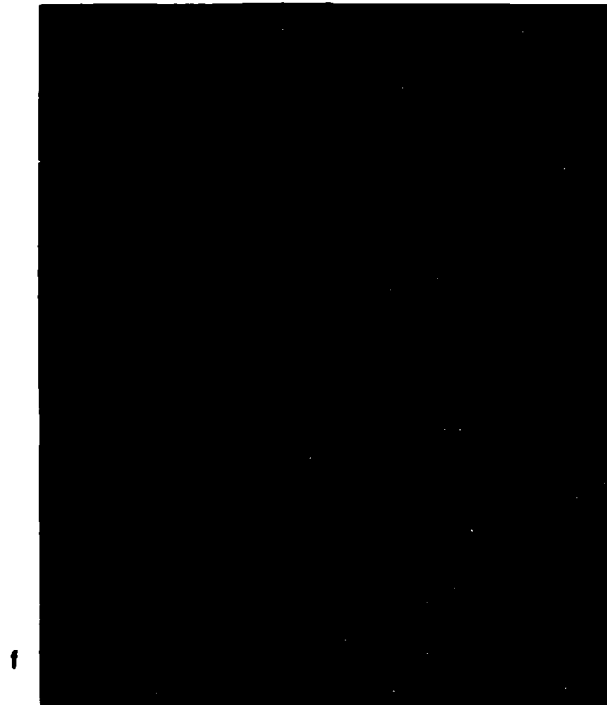
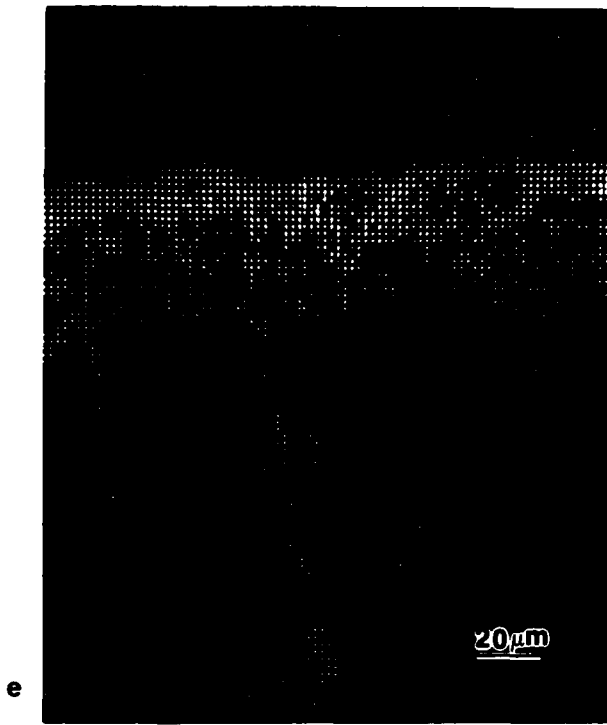


Figure 2.2-23 Elemental Maps of Cross-section of Oxidized 2RE1 (58-26-4-12)
Same Field as Figure 22 a
(e) O, (f) Ti



Figure 2.2-24 Absorbed Image of Cross-section of Oxidized K
(70-7-3-20) (500x)

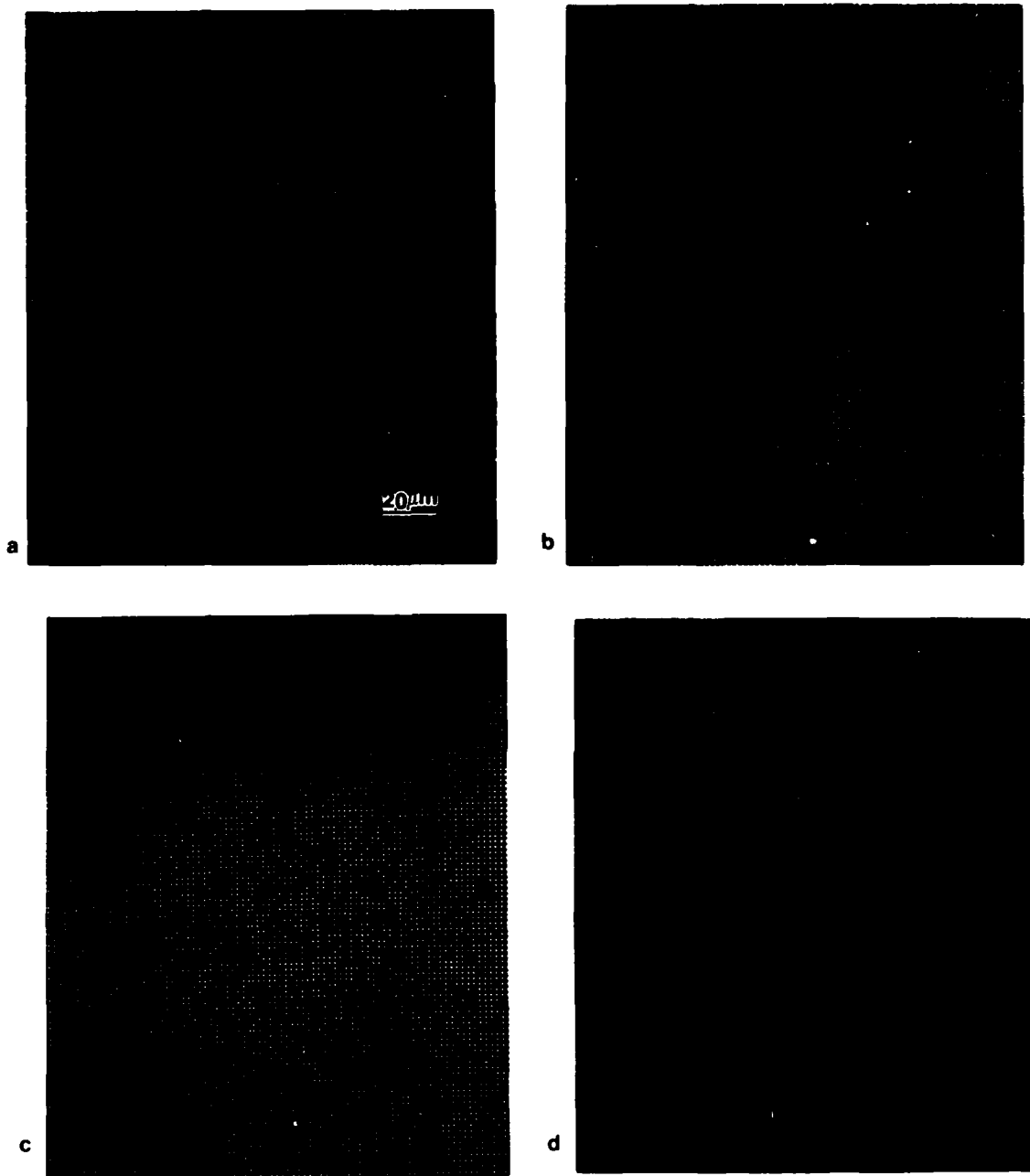


Figure 2.2-25 Elemental Maps of Cross-section of Oxidized K (70-7-3-20)
Same Field as Figure 24
(a) Al, (b) Cr, (c) Ni, (d) O

2.2.3 DISCUSSION

The results give a clear indication of the relative oxidation resistances of the substrate and the two classes of claddings. The 70-7-3-20 claddings suffered the least loss of metal based upon thickness and gained the least weight during oxidation. While the oxidation tests were only of 8 hours in duration, it is unlikely that the 58-26-4-12 claddings would ever prove superior in oxidation resistance at 1200°C since their weight gain rates are higher than those for the 58-26-4-12 claddings throughout the test period. Despite the fact the 58-26-4-12 claddings gained more weight than the substrate, the fact that far less metal was lost to oxidation is some evidence of a modest improvement over the substrate.

The most obvious source of the contrast between the two classes of claddings is the alloy composition. Examination of the Auger photomicrographs and elemental maps suggests that at least part of the compositional effect is due to the Al content. The primary metallic element in the outermost oxide layers in the 70-7-3-20 samples is Al while the corresponding layer in the 58-26-4-12 samples contain Ni, Ti, Cr and very little Al. Earlier work [8] on the oxidation resistance of five common superalloys at 1200°C in air indicated that chromium oxides were usually the most volatile oxides to form in these alloys during oxidation while aluminum and silicon oxides were the least volatile. As mentioned in Section 1 of this report, Al_2O_3 is the protective coating of choice since 1) diffusion through this oxide layer is very slow, 2) volatility is limited, 3) growth kinetics is slow, and 4) it is relatively inert in a high temperature oxidation environment.

In addition to the effect of forming more alumina during oxidation the microstructural effect of higher Al upon oxidation resistance must be

considered. As described in Section 2.2.1, the microstructure of the The 70-7-3-20 series samples consists mostly of γ' and a small amount of eutectic phase. The microstructure of the 58-26-4-12 samples contains a number of metastable Hf-rich phases as well as a much lower volume fraction of γ' . This difference in itself could be responsible for the variation in the oxidation behavior of the two compositions. Hence, future work must be directed towards determining how the microstructure of the 70-7-3-20 samples contributes to superior oxidation resistance.

The effect of Hf content upon the oxidation resistance of these claddings remains unclear. As noted, the high atomic number of Hf limits its detectability using AES. Even so, the lack of any relatively high concentration of Hf in the 58-26-4-12 and 70-7-3-20 samples within or immediately below the oxide layers (Figs. 2.2-23 and 2.2-25) suggests that its effect in these claddings was rather small. Examination of the sample cross-sections using SEM and energy dispersive X-ray techniques is a necessary if insufficient method to determine the effect of Hf [9].

One interesting result is the presence of Ti in the outermost oxide layers in the 58-26-4-12 samples despite not being present in the cladding powder. Microprobe results indicating that the 58-26-4-12 cladding nuggets contained more Ti than those of the 70-7-3-20 composition suggest that more of the substrate was melted during the cladding of the former set of samples. The exact impact of higher Ti contents in the oxide on the oxidation resistance of the claddings is not yet clear, but its mere presence in the cladding must be reckoned with during further alloy and laser processing design work.

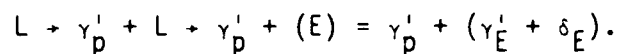
The complicating effect of probable PtO_2 volatilization during oxidation testing merits some additional investigation since the adjustments made in

Figs. 2.2-6 and 2.2-7 result in constant oxidation rates for all of the claddings. Fortunately, this effect does not obscure the relative advantage of the 70-7-3-20 claddings.

The cracks observed in Fig. 2.2-9 are of great concern. Given that the cracks correspond to the vertical direction during cladding and are outlined by heavy oxide layers, the cracks probably were generated during the cladding process itself. Fortunately no such cracks were observed in either sample from the 70-7-3-20 series of claddings, so it is possible that this composition is more resistant to cracking during processing as well as having better oxidation resistance.

2.3 CONCLUSIONS

- (1) The 70-7-3-20 claddings microstructurally consisted of γ' mostly in the form of dendrites, together with a small amount of eutectic constituents. There was also some amount of undissolved or partially dissolved Hf particles.
- (2) The eutectic structure was a mixture of two phases which are Hf rich (δ phase) and Hf lean (γ'_E).
- (3) The possible phase transformation sequence in this system could be represented as



- (4) The lattice parameter of γ' , produced by the laser cladding process, is $a = 3.458 \text{ \AA}$, the crystal structure is ordered f.c.c ($L1_2$) and the point group is $m3m$.

- (5) The Hf rich, δ phase is a heavily faulted f.c.c structure with lattice parameter $a = 10.96 \text{ \AA}$. The Hf lean, γ'_E phase is an ordered f.c.c structure ($L1_2$) with lattice parameter $a = 3.62 \text{ \AA}$ and point group is $43m$.
- (6) Microchemistry studies indicate that the extent of Hf in terminal solid solution is about 13 wt.%, which indicates an extended solid solubility in the system as compared to cast superalloys.
- (7) Laser processing parameters, e.g. laser power, traverse speed, etc., influences the morphology of the APB in γ' .
- (8) Preliminary results indicate that the $(1/2) a_0 \langle 110 \rangle$ vector appears almost exclusively in this system in the $L1_2$ ordered γ' .
- (9) The oxidation resistance of the 70-7-3-20 claddings was superior to that for both the substrate and the 58-26-4-12 claddings based upon TGA and unoxidized metal thickness measurements.
- (10) The surface scale of oxidized samples of the 70-7-3-20 claddings contained more Al and less Cr than those from the 58-26-4-12 claddings and the substrate.

2.4 FUTURE WORK

- (1) The internal defect structure in the δ phase needs to be studied carefully to understand the phase transformation in the system.
- (2) Further work needs to be done on the process parameter dependence of APB's in order to obtain a clearer picture of the mode of their formation.
- (3) Composition optimization needs to be performed in order to determine the ideal composition for high oxidation resistance coupled with high γ' dissolution temperature.

- (4) Further compositional analysis using intermetallic standards need to be performed in order to obtain a more accurate microchemistry.
- (5) Determine how the cladding microstructure affects oxidation behavior using SEM and energy dispersive X-ray analysis (EDX) and AEM techniques.
- (6) Using AES, SEM and EDX techniques, determine the effect of Hf upon the oxidation resistance of the claddings.
- (7) Determine the cause of the cladding cracks and the means of avoiding such cracks using metallurgical techniques.
- (8) Determine if the samples from the 70-7-3-20 claddings actually passivate during oxidation testing by isolating the PtO_2 volatilization effects.

3. LASER CLADDING OF Nb-Ti SYSTEM

3.1 EXPERIMENTAL PROCEDURE

The insitu laser cladding of Ti onto Nb has been carried out using a 10 kW CW CO_2 laser. Ti powder (99.9% pure, ~ 200 μm size) has been cladded onto Nb plates under the following process conditions:

Power:	4, 5, 6, 7 kW
Translation speed:	0.00846, 0.0127, 0.01693, 0.02116 m/s
Beam diameter:	0.003 m
Beam-focus condition:	Overfocussed beam
Shielding Gas:	Helium

Thin foil for electron microscopy study has been prepared in the following manner. Top surface of the clad has been ground to a flat surface. The

underlying substrate has been removed by grinding to get a thin section of the clad material. A 3 mm disc has been punched out from the clad section and jet polished to get thin foil using the electrolyte,

Perchloric acid:	60 ml
Ethylene glycol mono butyl ether:	360 ml
Methanol:	600 ml

under the following conditions,

Voltage:	30 V
Temperature:	-10 to -15°C

The electron microscope, Philips EM 400, has been used to carry out the microstructural study of the clad.

Differential thermal analysis and differential scanning calorimetry have been done on the clad material under the following operating conditions:

Temperature range:	25 to 1100°C
Heating rate:	20°C/min
Atmosphere:	Argon
Flow rate:	40 cc/min

The sectioning of clad has been done in the same way used to prepare thin foil for electron microscopy. A portion of the clad section has been accurately weighed and thermal analysis has been done.

3.2 RESULTS AND DISCUSSION

Laser cladding of Ti onto Nb and subsequent studies of the clad material have been discussed in the previous report. Niobium has high strength at high temperatures but very poor oxidation resistance above 300°C [10]. Conventional coating techniques [11-24] and alloying Nb in the conventional ingot metallurgy route have been used to prevent oxidation at high temperatures. Laser cladding a carefully chosen material onto Nb has its unique advantages over other techniques. Addition of Ti in different amounts (10, 20, 30 wt%) has been found to improve the oxidation resistance of Nb [25]. Oxygen diffusion has been reported as the preponderant mechanism of oxidation of Nb alloys. Increase in Ti content has been found to decrease the oxygen penetration and increase the high temperature stability.

In this regard, laser cladding of Ti onto Nb has been done in the present investigation and the clad material has been analyzed using different metallographic techniques.

In situ laser cladding of Zr onto Mg and the evaluation of corrosion properties of the clad material have been mentioned in the previous report. Significant improvement of corrosion resistance by laser cladding has been reported in that investigation.

Optical Microscopy

The cross section of the clad has been examined in the optical microscope (Fig. 3-1). Good fusion has been observed at the interface with no defects in the clad. The darkly etched phase at the interface is the widmanstätten structure of Ti. The α needles and the β matrix of the widmanstätten β -transformed structure are seen at the interface.

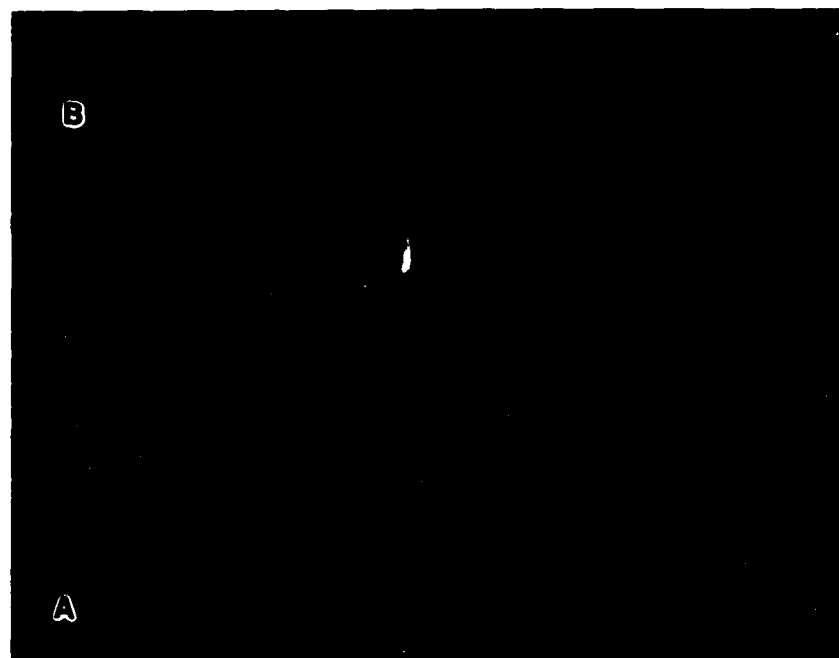


Fig. 3-1 Optical micrograph of the clad/substrate (Ti/Nb). The widmanstätten β -transformed structure is seen at the interface.

Martensitic Plates

Different phases in the clad region have been observed. Figures 3-2a and 3-2b show the bright field image of the martensitic plates. Different sizes of the martensitic plates have been observed. The martensitic plates are heavily faulted containing dislocations suggesting the shear type of transformation.

The SAD pattern (Fig. 3-2c) taken from the martensitic plate has been analyzed and is of $1\bar{2}1\bar{3}$ zone axis. The lattice parameters calculated from this spot pattern are $a = 2.78 \text{ \AA}$, $c = 4.54 \text{ \AA}$. The lattice parameters of pure Ti are: $a = 2.95 \text{ \AA}$, $c = 4.68 \text{ \AA}$. Figure 3-2d shows another zone axis $(01\bar{1}2)$ pattern from the same plate.

Unalloyed Ti transforms martensitically from bcc to hcp during cooling through its $\beta \rightarrow \alpha$ allotropic transformation temperature, 882°C . In alloys of Ti, the equilibrium α and β fields are separated by a two-phase, $\alpha + \beta$, region and the $\beta \rightarrow \alpha^m$ (α^m is used as a short-hand notation for the product of martensitic transformation, whether it be α' or α'') transformation temperature, M_s , is composition dependent.

In α -stabilized alloys, typified by Ti-Al, M_s may lie a little below the $(\alpha+\beta)/\alpha$ transus [26]; in the β -stabilized alloys (present investigation, Ti-Nb) it always lies within the $\alpha+\beta$ field.

In contrast to nucleation-and-growth types of phase change which rely on thermally activated atomic diffusion, martensitic transformations involve a cooperative movement of atoms resulting in a microscopically homogenous transformation of one crystal lattice into another. The ideal martensitic process itself is not thermally activated and takes place at high speeds (temperature-independent); but in practice a clear-cut separation of transformation processes into "nucleation-and-growth" and "martensitic" is generally not

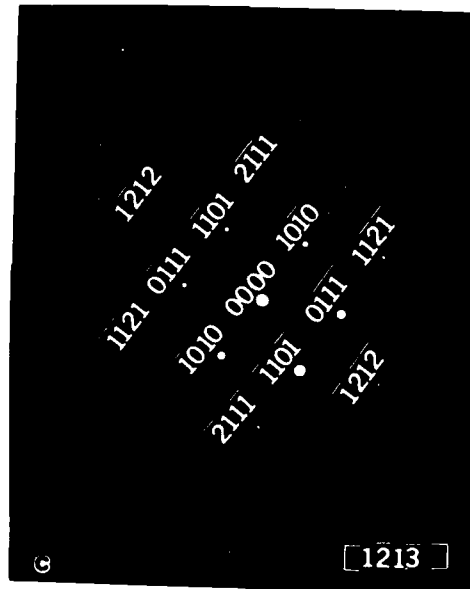
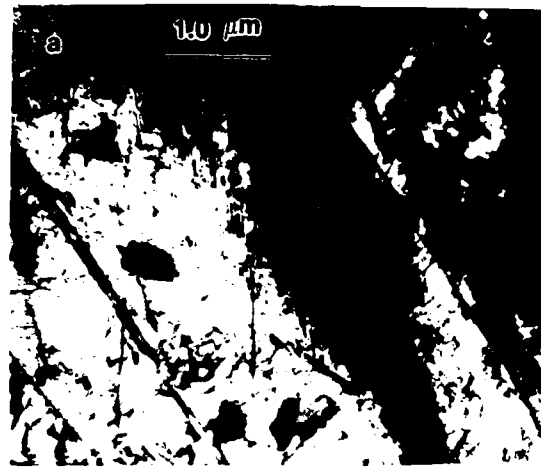


Fig. 3-2 Martensitic plates in the clad region. a) BF image of the martensitic plates containing faults and dislocations. b) martensitic plates at higher magnification. c) $[1\bar{2}13]$ zone SAD pattern from the martensitic plate.

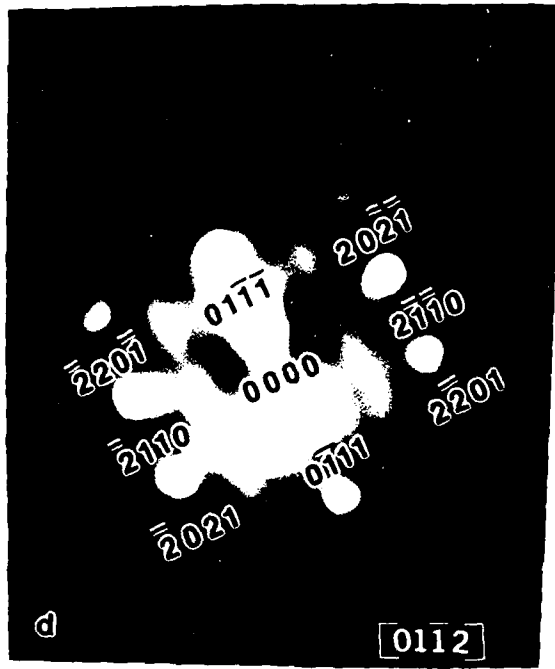


Fig. 3-2 (d) $[01\bar{1}2]$ Zone SAD pattern from the martensitic plate

possible. Although in pure metals, such as unalloyed Ti, a simple athermal martensitic transformation is conceivable, in an alloy the situation is more complicated. The long-range effect of alloying, described for example in terms of changes of the elastic parameters, may be to change the conditions under which athermal transformation takes place. On the other hand, the local effect of alloying is to inhibit the movement of atomic planes and thereby: (i) to reduce the distances over which atomic regions can cooperate, which perturbs the microstructure of the transformation product; and (ii) to reduce the speed of the transformation, thus bringing it into competition with the nucleation-and-growth mechanism [27].

When conditions are particularly favorable, transformation from β to α^m takes place completely, on a large scale, and with considerable structural coherence. The result is the so-called "massive martensite" (otherwise known as lath martensite), which consists of large irregular zones on the scale of 50 to 100 μm , subdivided into parallel arrays of fine platelets less than 1 μm across.

The martensitically transformed structure assumed by the pure Ti and by the dilute Ti-transition metal alloys in general, is hcp and has been assigned the symbol α' [28,29]. Quenched Ti-transition metal alloys with compositions exceeding certain limits, which differ from system to system, transform to an orthorhombic martensite designated by α'' . The α'/α'' compositional boundaries for the Ti-transition metal alloy systems have been determined by Bagariatskii, et al. [28]. For the Ti-Nb system (under present investigation) the α'/α'' boundary is at 10.5 wt% (5.7 at%) Nb in Ti. In another work [30], it has been reported that at concentrations higher than 11 at% Nb, the quenched martensitic structure is orthorhombic α'' which seems to persist out to concentrations as high as 25 at% Nb depending on the quenching conditions.

The results of studies of martensitic transformation in representative members of the Ti-V, Ti-Nb, and Ti-Mo systems by Flower, et al. [31] describe that α'' has been detected in Ti-20Nb(11 at%). Since stress-induced martensite can occur only in alloys not already transformed by quenching, it is obviously confined to higher concentration ranges; therefore, the martensite is invariably of orthorhombic variety in the Ti-transition metal alloy systems [13].

Amorphous Phase

In the clad region, a distinct phase (Figs. 3-3a and 3-3b) gave rise to diffuse ring pattern (Fig. 3-3c). Figures 3-4a and 3-4c show the similar amorphous phase. The spot pattern (Fig. 3-4b) taken from region marked 'A' in Fig. 3-4a is from the crystalline phase. The SAD pattern at the interface (indicated by the arrow in Fig. 3-4a) shows the diffuse ring pattern from the amorphous phase and the superimposed spot pattern (Fig. 3-4d) from the crystalline phase.

Scanning Transmission Electron Microscopy

The region in the clad which showed the amorphous phase in transmission electron microscope has been studied in scanning transmission electron microscope. In that region crystallites have been found to be distributed in an amorphous phase. The crystallites (indicated by 'A' in Fig. 3-5b) are of size 0.05 to 0.2 μm . Microdiffraction patterns have been obtained using an electron beam of 10 \AA size in STEM. Microdiffraction pattern from the crystallite (Fig. 3-5c) shows spot pattern and that from amorphous region (indicated by 'B' in Fig. 3-5b) shows diffuse ring pattern (Fig. 3-5d). Figures 3-6a through 3-6d show the bright field images and microdiffraction patterns obtained from the crystallites and amorphous phase from the same region at

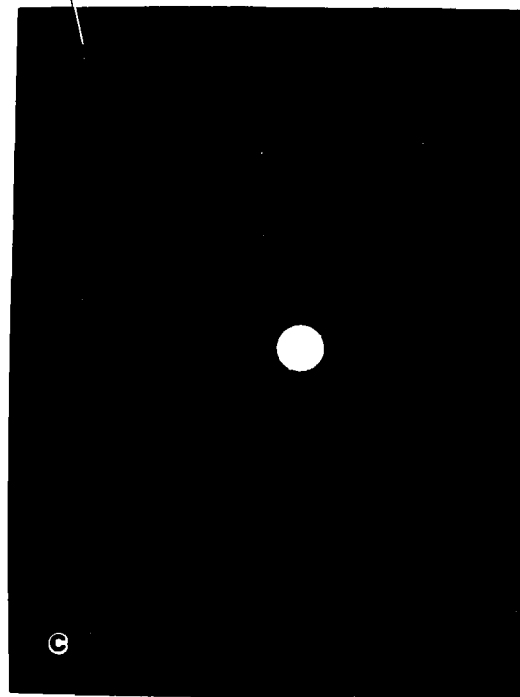
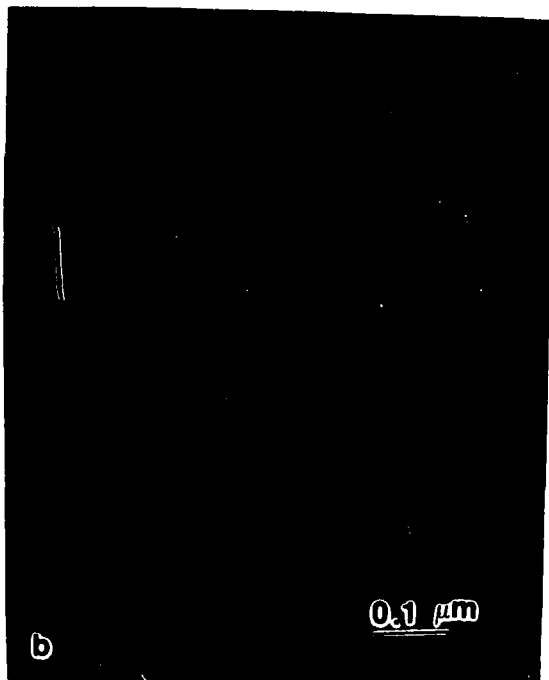


Fig. 3-3 Amorphous phase in the clad region. a) BF image of the amorphous region. b) BF image of the same region at higher magnification. c) SAD pattern from the amorphous phase showing diffuse ring pattern.

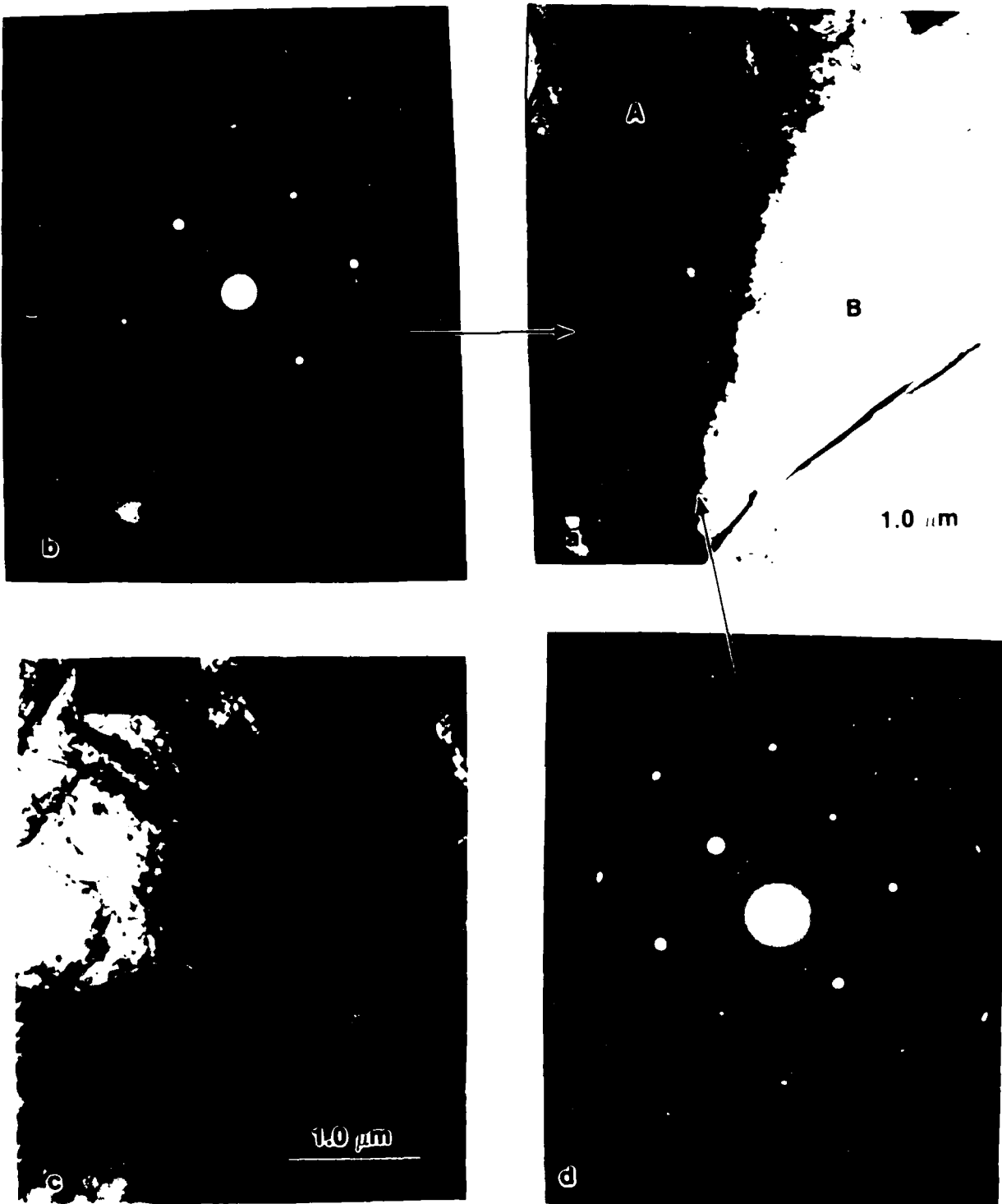
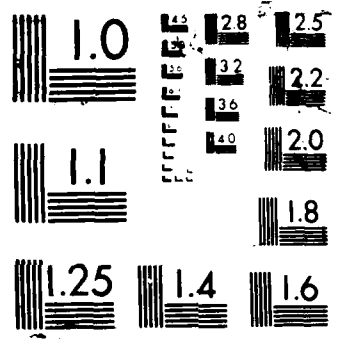


Fig. 3-4 A different amorphous region in the clad. a) BF image of amorphous phase and the adjacent crystalline phase. b) SAD pattern from the crystalline phase. c) BF image of the crystalline phase. d) SAD pattern from the amorphous-crystalline interface showing diffuse ring pattern superimposed on the spot pattern.



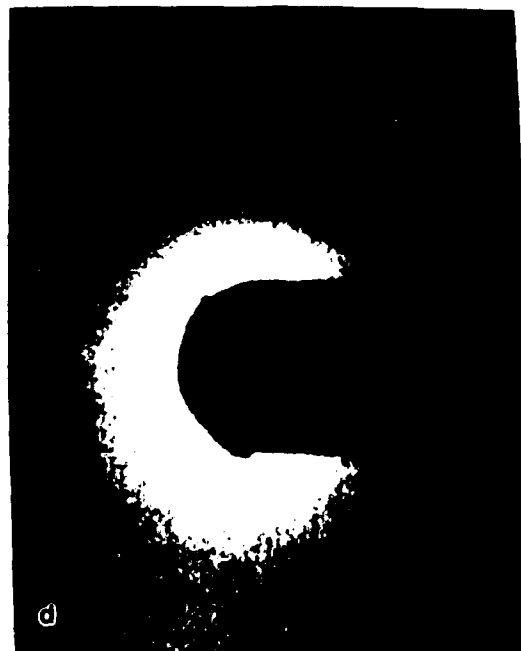
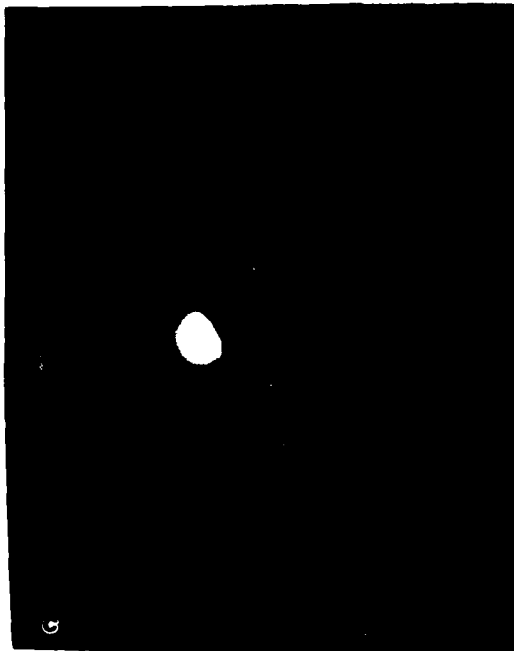
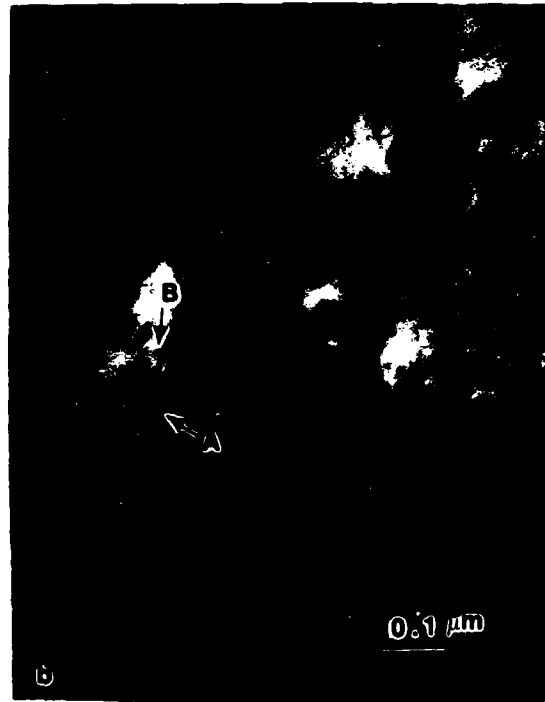


Fig. 3-5 Scanning transmission electron micrograph of the clad.
a) BF image of the amorphous image (from the same area shown in TEM micrograph Fig. 3-3. b) BF image of the amorphous phase containing crystallites.
c) micro-diffraction pattern from the crystallite (marked 'A', in Fig. 3-5b). d) microdiffraction pattern from the amorphous phase (marked 'B' in Fig. 3-5b).

higher magnification. Spot pattern (Fig. 3-6c) has been obtained from region 'A' in Fig. 3-6a and diffuse ring pattern (Fig. 3-6d) has been obtained from region 'B' in the same Fig. 3-6a.

In the literature, similar observations of amorphous phase in Nb-Ti system under rapid solidification conditions have been reported. Two categories of amorphous alloys have been identified. The first category, and the most widely investigated, is the metal-metalloid type in which the metal is a late transition metal and the metalloid content is about 20 wt%. The second category is the metal-metal type in which one metal is a late transition metal; no strict composition requirements have been noticed in this category. A new category consists of an early transition metal (Ti) and either a metalloid or a late transition metal and a metalloid or another early transition metal (Nb) and a metalloid [32].

The amount of Nb is found to vary in the amorphous phase region. The preliminary work of composition analysis carried out in STEM shows the following data. The crystalline region marked 'A' in Fig. 3-5b is found to have the composition: 3.26 at% Nb-Ti. Figure 3-7 shows the X-ray energy dispersive analysis data from the same region 'A' analyzed in STEM. The amorphous region marked 'B' in Fig. 3-5b is found to have the composition: 8.77 at% Nb-Ti. Figure 3-8 shows the X-ray energy dispersive analysis data from the same region 'B'.

Thermal Analysis of the Clad

Figure 3-9 shows the DSC data of the Ti/Nb cladding made under the process conditions, 6 kW, 0.021 m/sec, 0.003 m beam diameter and helium as the shielding gas. The onset of $\alpha + \beta$ transformation is 874.1°C compared to 882°C in case of pure Ti. This suggests the solubility of Nb in Ti as seen in the phase diagram Ti-Nb (Fig. 3-10).

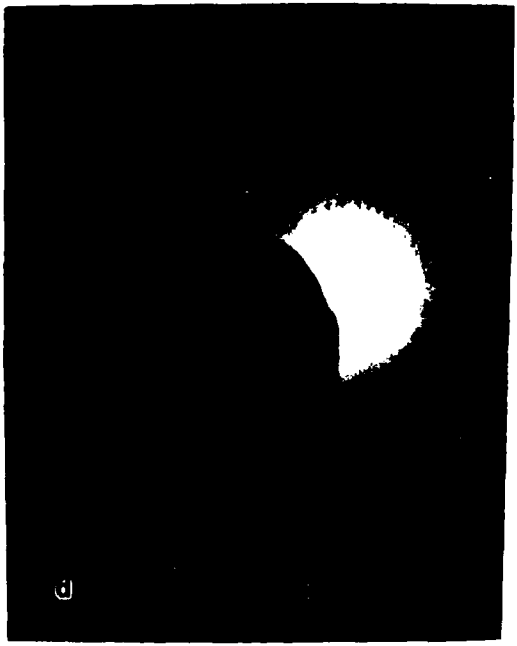
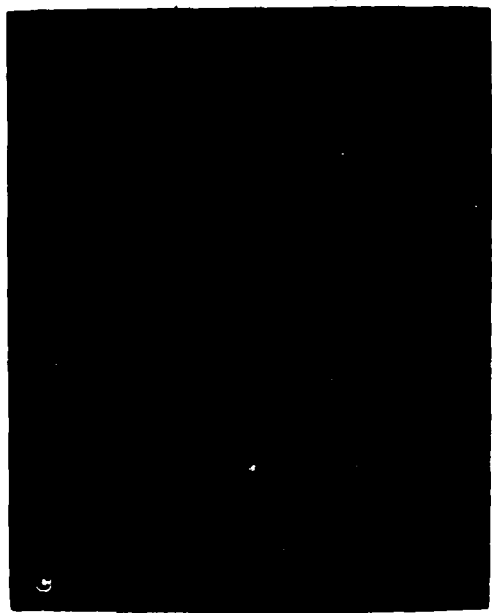


Fig. 3-6 The scanning transmission electron micrograph of the clad. a) and b) BF image of the amorphous phase containing crystallites at higher magnification than Fig. 3-5. c) microdiffraction pattern from the crystallite (marked 'A' in Fig. 3-5a). d) microdiffraction pattern from the amorphous phase (marked 'B' in Fig. 3-5a).

STEMC3

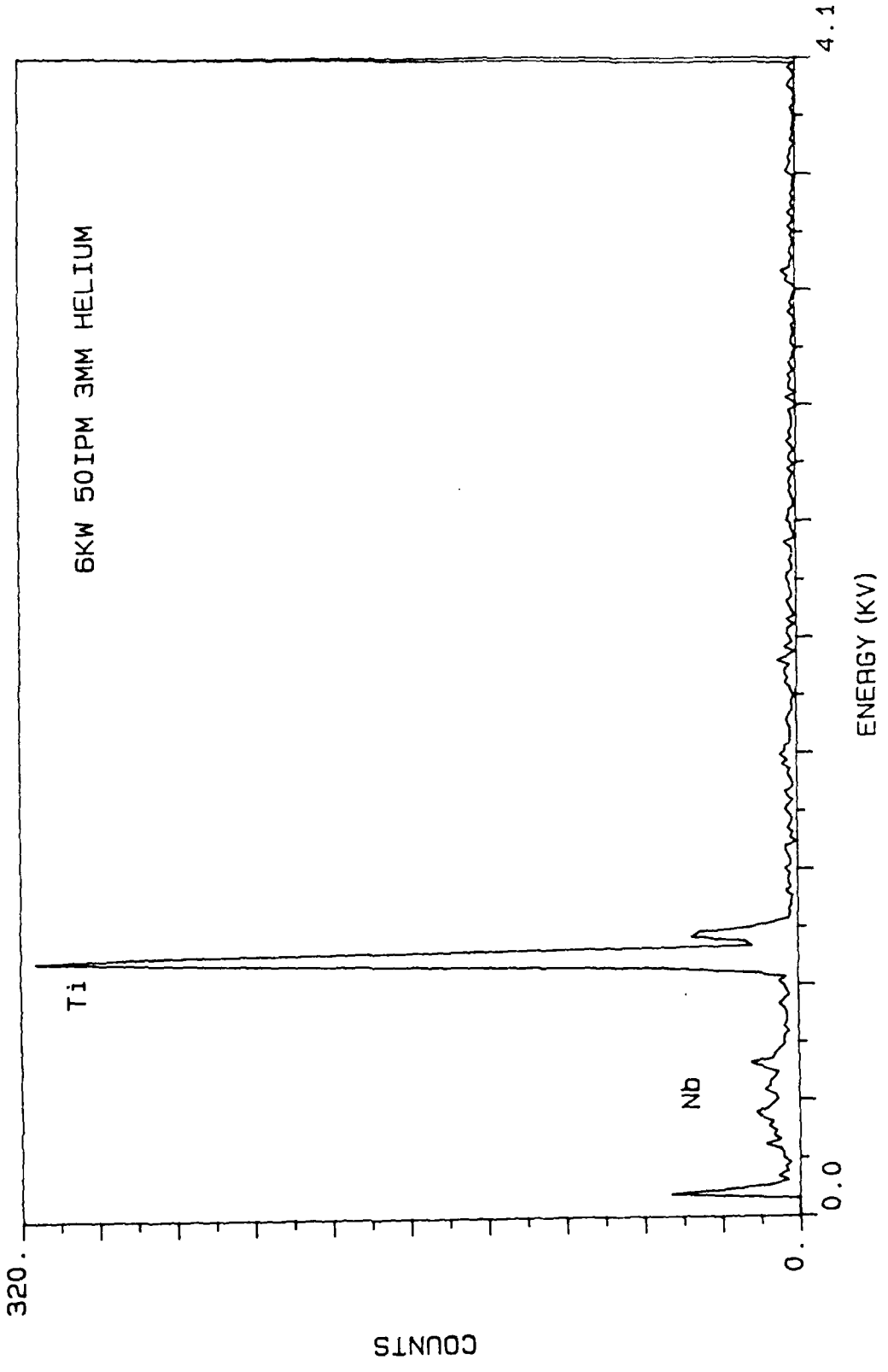


Fig. 3-7 X-ray energy dispersive analysis obtained in STEM from the crystallite.

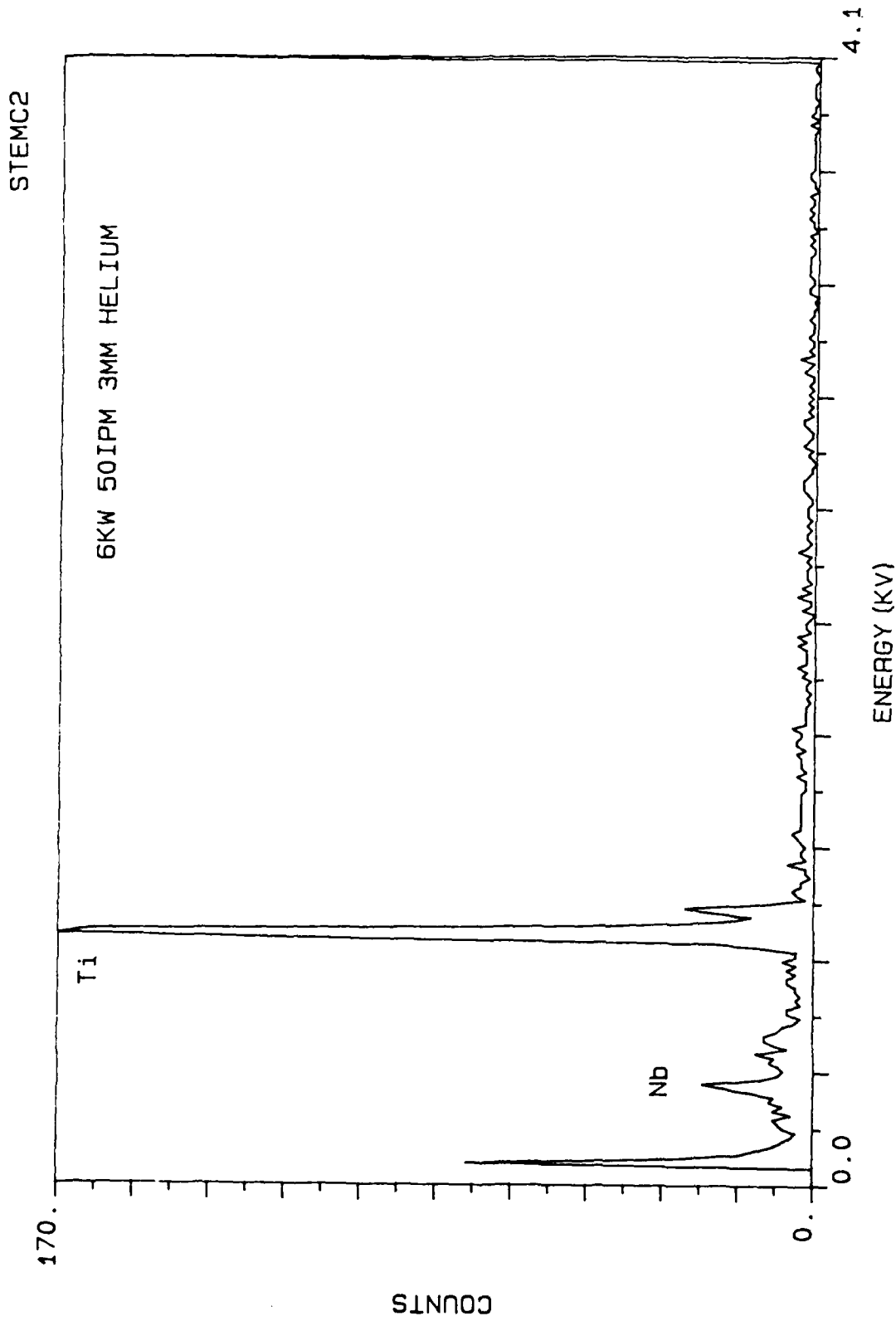


Fig. 3-8 X-ray energy dispersive analysis obtained in STEM from the amorphous phase.

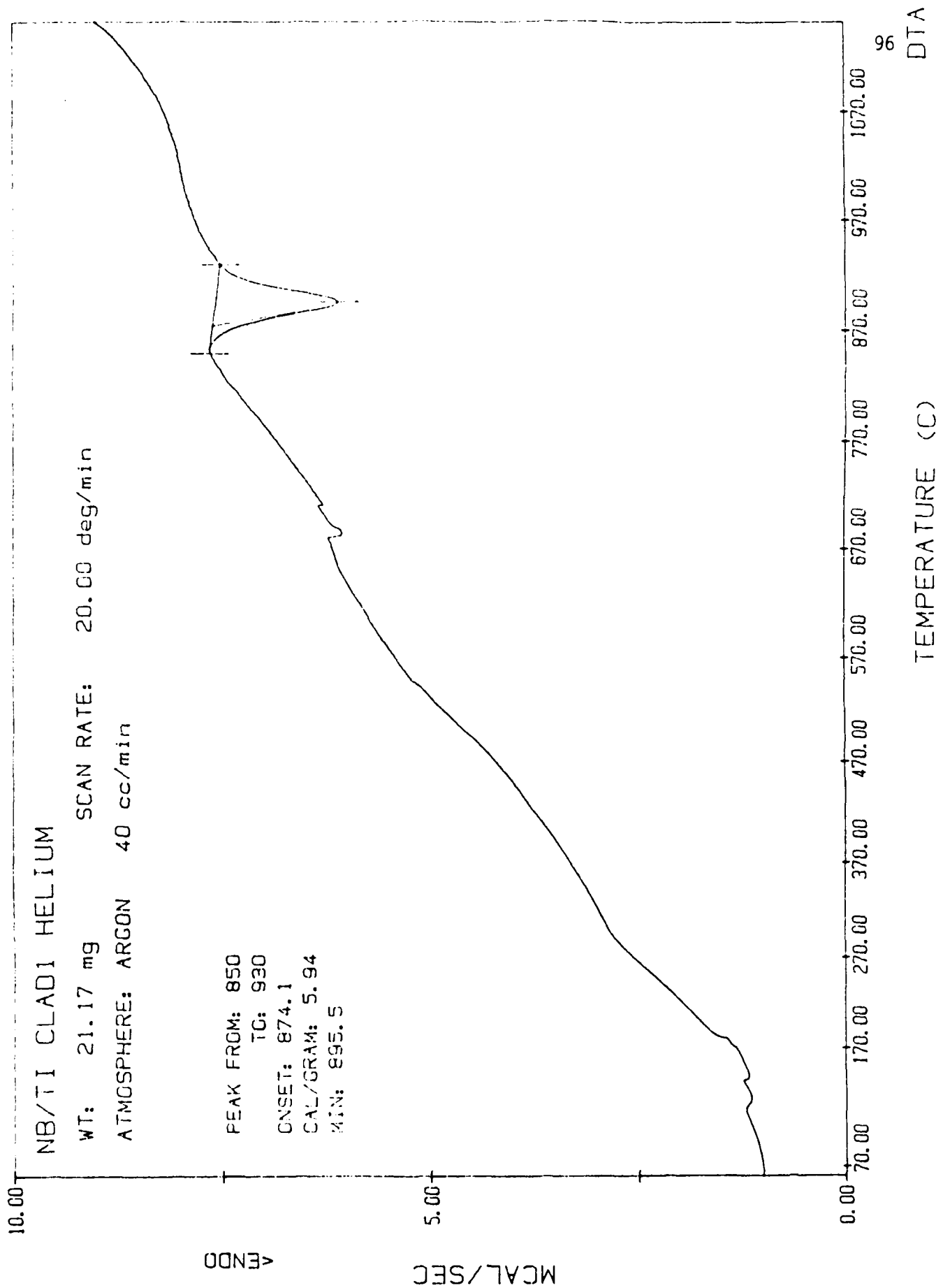


Fig. 3-9 A plot from the DSC analysis of the clad region (Ti/Nb); process parameters: 6 kW, 0.02116 m/s, 0.003 m, Helium.

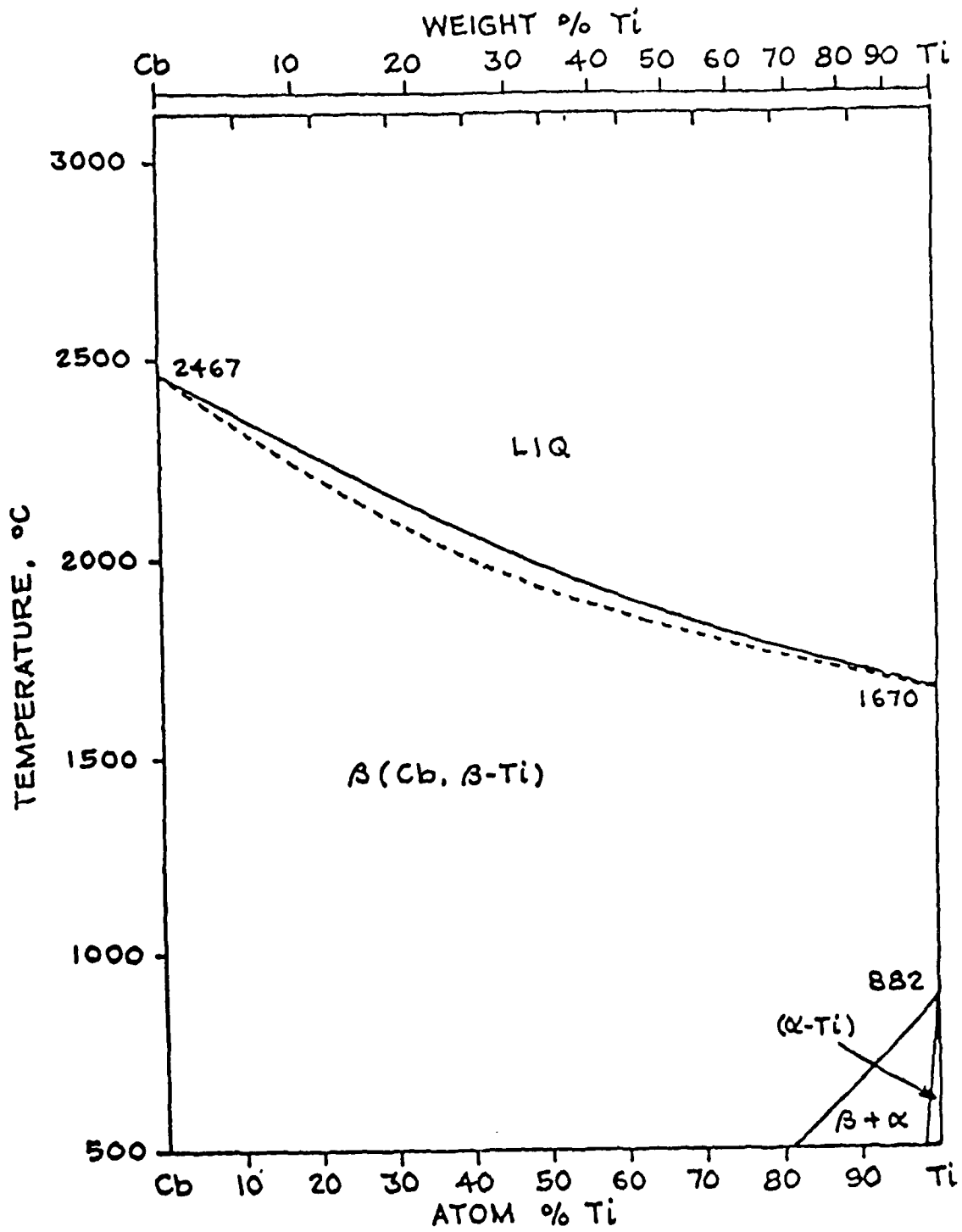


Fig. 3-10 Equilibrium phase diagram of Ti-Nb system.

Figure 3-11 shows the DSC data of the Ti/Nb cladding made under the following process conditions: 8 kW, 0.0043 m/sec, 0.003 m beam diameter, using argon as shielding gas. The lower temperature of onset of $\alpha \rightarrow \beta$ transformation (860.2°C) suggests the increase in the amount of Nb dissolved in the Ti clad as seen in the phase diagram.

Surface Profile Analysis of the Clad

The surface profile of the clad using different parameters have been determined. The cladding was carried out by delivering constant amount of powder into the laser interaction zone. The average radius of the various claddings determined by Talysurf surface profile analyzer has been plotted in Fig. 3-12 for various process parameters. The constant radius of the cladding is due to the constant amount of powder delivered into the laser interaction zone.

3.3 CONCLUSION

- (1) Good fusion has been observed at the Ti/Nb interface; there are no defects in the clad. In the optical micrograph of the clad, widmanstätten β -transformed structure has been observed in the clad near the interface.
- (2) Martensitic plates have been found in the electronmicroscopy of the clad. Different size of the martensitic plates have been found. These plates are heavily faulted containing dislocations. The lattice parameters of the martensite α' determined by using the SAD pattern from the martensitic plate are: $a = 2.78 \text{ \AA}$, $c = 4.54 \text{ \AA}$.
- (3) Amorphous phase has been found in the electron microscopy of the clad. The microchemical analysis shows that the amorphous phase con-

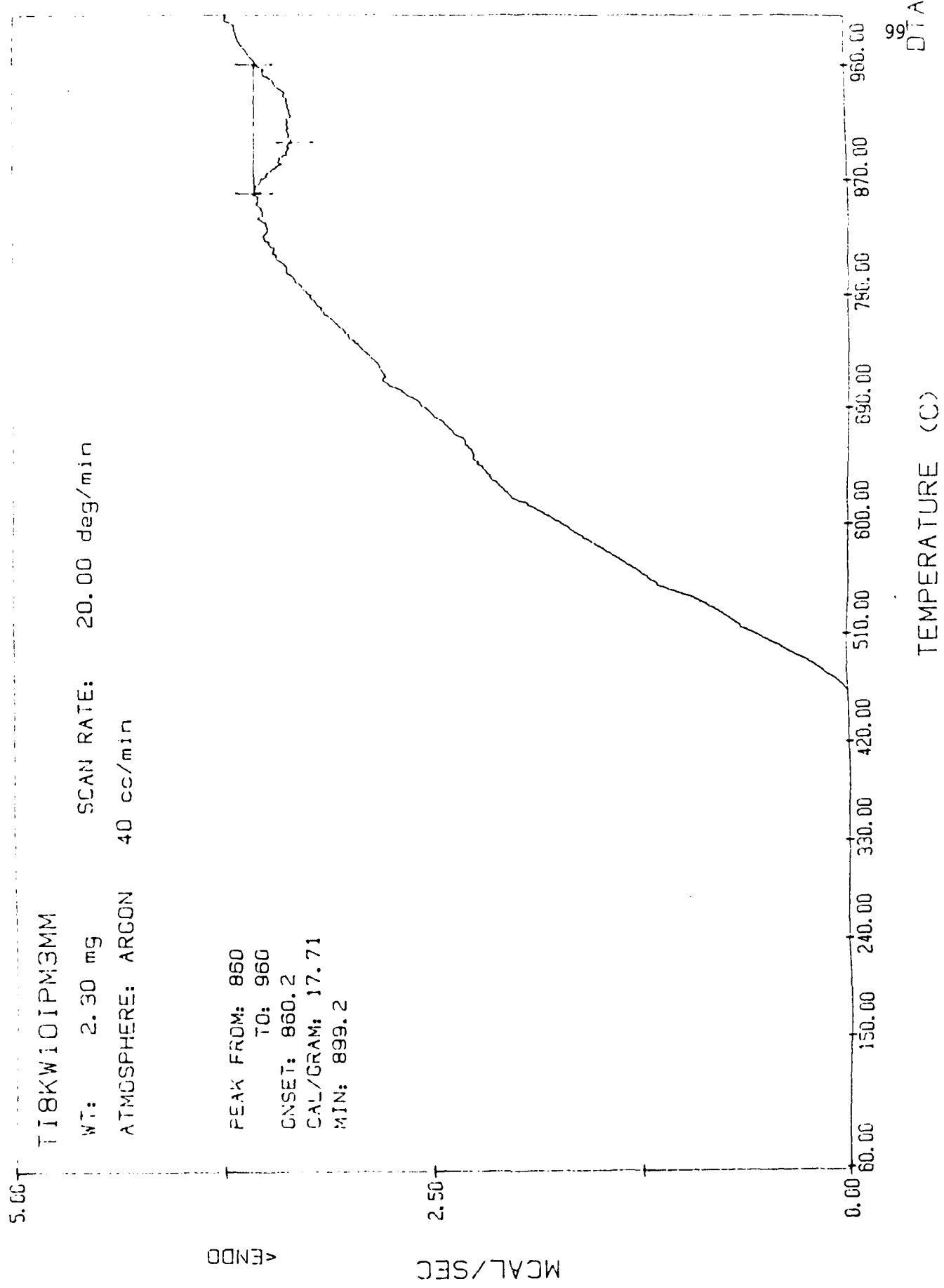


Fig. 3-11 A plot of the DSC analysis of the clad region (Ti/Nb); process parameters: 8 kW, 0.00423 m/s, 0.003 m, Argon.

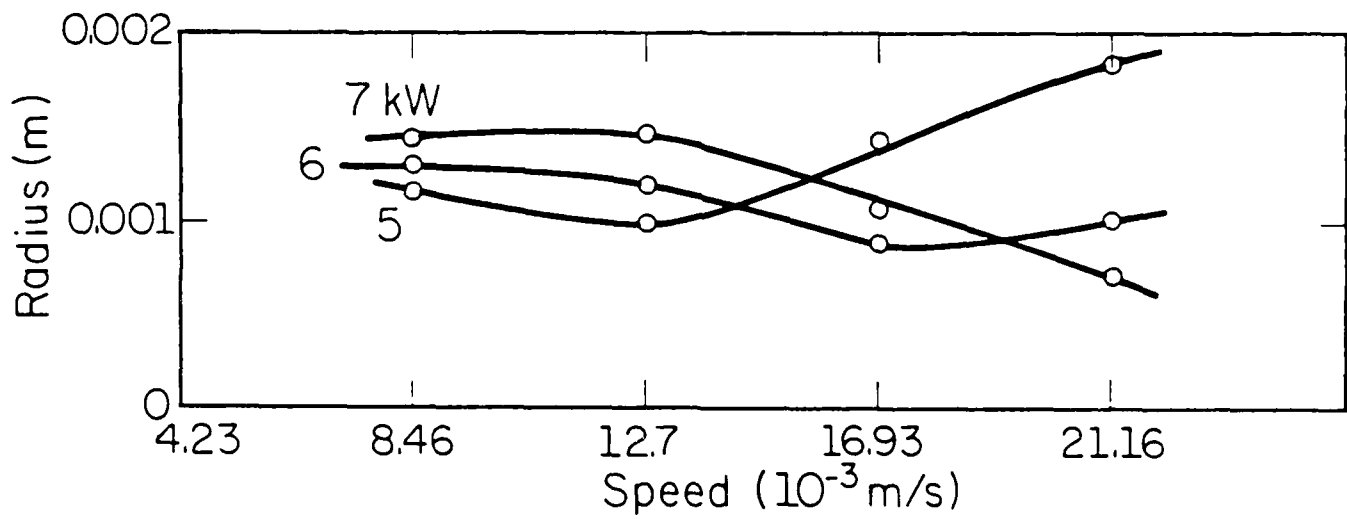


Fig. 3-12 Average radius of the clad (Ti/Nb) made using different power, translation speed and constant amount of powder delivered into the laser interaction zone.

tains relatively higher Nb compared to the crystalline phase. In the amorphous region, crystallites are found to be distributed uniformly. The crystallites are found to be depleted in Nb content.

- (4) The radius of the cladding of Ti onto Nb using different laser cladding process parameters is found to be constant on account of constant amount of powder delivered into the laser interaction zone.

3.4 FUTURE WORK

The oxidation behavior of the clad material has to be evaluated using thermogravimetric analyzer. The data obtained by TGA has to be compared with similar oxidation behavior of Nb-Ti(10, 20, 30 wt%) alloys [25] produced in the conventional ingot metallurgy route.

The role of the amorphous phase in improvement of oxidation resistance of rapidly solidified Nb-Ti alloys has not been reported. Further studies have to be done along this line. Crystallization behavior of the amorphous phase as observed in the present investigation has to be done using DSC and the result has to be correlated with the high temperature behavior of the clad material in TGA.

The martensitic phase transformation of the clad material has to be studied in detail. The crystallographic study of the martensitic plates with different amount of Nb in solid solution has been envisaged.

A screw feeder (Fig. 3-13) has been designed to deliver the zirconium powder into the laser interaction zone on the surface of Mg sample to carry out insitu laser cladding. This feeder has to be calibrated in terms of speed versus amount of powder delivered under different process conditions. This is necessary to determine the effective utilization of the powder in the cladding process. The cladding process has to be made more efficient to reduce wastage

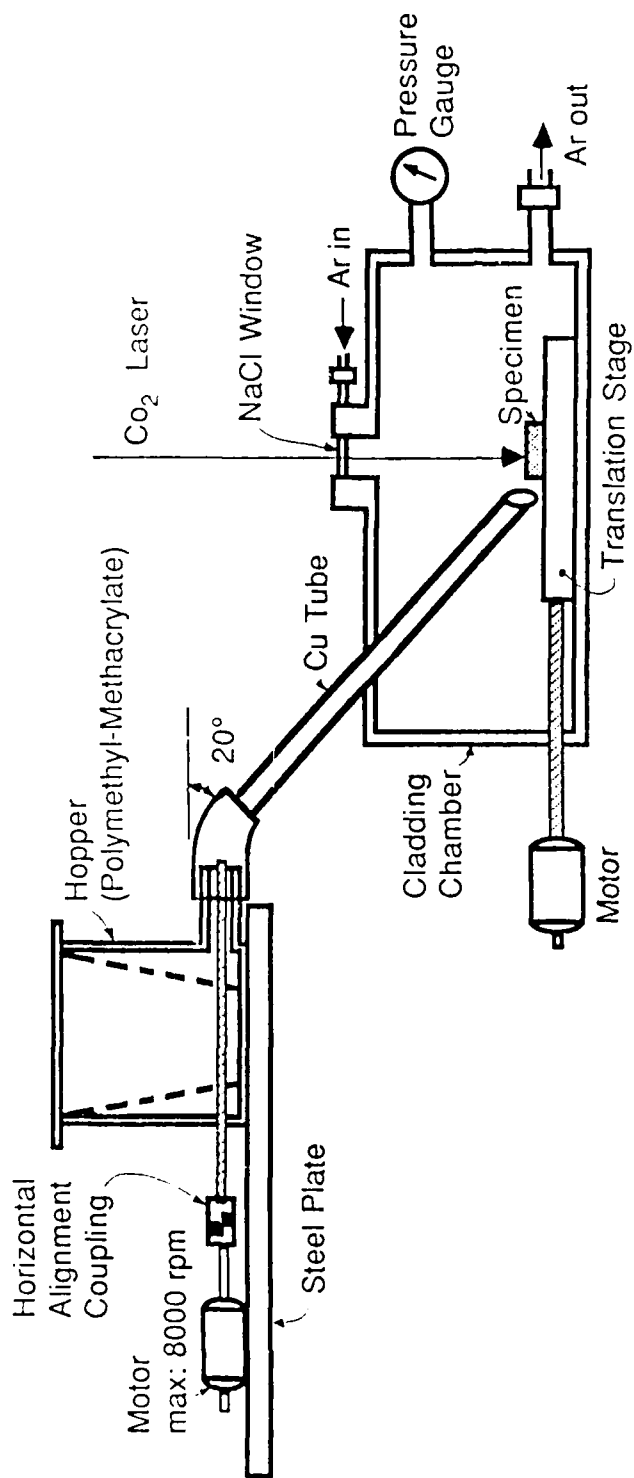


Fig. 3-13 The screw feeder designed to carry out the in situ laser cladding of Zr onto Mg.

of powder. It has to be faster to deposit a large amount of material onto the substrate. The coefficient of utilization of powder has been defined as the ratio of the mass of powder forming the cladding to the mass of powder consumed. This is an important characteristic of the technological processes taking place in applying coatings by melting powder with a laser beam. Powder which has not been melted can be re-used. The aim of the future investigation of laser cladding of Zr onto Mg is to achieve the maximum coefficient of utilization of powder with satisfactory formation of the deposited metal. The subsequent evaluation of the corrosion properties of the clad material has to be done as before. The previous work done on this Mg-Zr system shows amorphous phase rich in Zr (84.634 wt% Zr, 15.367 wt% Mg) has been found in the electron microscopic investigation of the clad material. The significant improvement in the corrosion resistance of the clad material has been ascribed to the formation of amorphous phase rich in Zr. Further work along this line has been envisaged. Alloy powder (Mg with large amount of Zr) can be laser cladded onto Mg to produce amorphous material in the clad. Subsequent characterization of the clad has to be done to evaluate the corrosion properties.

4. MATHEMATICAL MODELING OF EXTENDED SOLID SOLUTION IN LASER CLADDING

4.1 CURRENT WORK

Besides the above-mentioned experimental works, theoretical studies have also been pursued to examine the extension of solid solubility observed during laser cladding. The mathematical model developed during this reporting period also enables us to study the effects of various laser processing parameters on the composition of cladding alloys. This model has been applied to nickel-hafnium (Ni-Hf) and nickel-aluminum (Ni-Al) systems. In both cases, theoretical predictions have been found in good agreement with experimental

results. These two systems differ from each other in that the Ni-Al equilibrium phase diagram has positive slope at the initial composition of the cladding powder, whereas it is negative for the Ni-Hf system. Because of this, decrease in the initial pool mean temperature causes reduction of Al and increase of Hf in Ni-Al and Ni-Hf systems, respectively. Currently, we are also concerned with the development of non-equilibrium partition coefficient for concentrated solutions. This is important because concentrated solutions are usually encountered in laser cladding processes. Consequently, the non-equilibrium partition coefficient obtained under dilute solution approximation is invalid for such processes.

The findings of our studies on Ni-Hf and Ni-Al systems have been submitted for publication. The paper on Ni-Hf system has been accepted for publication in Acta Metallurgica and the paper on Ni-Al system has been submitted for possible publication in Metallurgical Transaction A. Since the mathematical model and the results have been discussed in detail in these two papers, they have been appended to this report instead of rewriting them as a separate chapter for this report.

4.2 FUTURE WORK

The mathematical models that we have developed so far are one-dimensional and applicable to binary systems. These models utilize an expression of non-equilibrium partition coefficient which is not accurate for concentrated solution systems. Our plan is to eliminate these restrictions from our models and towards these objectives, we intend to do the following:

- (1) Examine non-equilibrium partition coefficient for concentrated solution.

- (2) Develop two- and three-dimensional models for laser cladding processes.
- (3) Use these models to predict the extension of solid solubility found in laser claddings and generate non-equilibrium phase diagrams.
- (4) Extend the binary system models to multi-component alloy systems.
- (5) Also, we want to study the formation of ripples in laser-melt liquid metal pools and its effect on the shape of the resulting solid formed from this melt pool.

5. REFERENCES

1. Li, L. J., and J. Mazumder, Laser Processing of Materials, K. Mukherjee and J. Mazumder, eds., published by TMS-AIME, Vol. 35, 1985.
2. Singh, J., and J. Mazumder, Acta Metallurgica, Vol. 35, No. 8, pp. 1995-2003, 1987.
3. Buxton, B. F., J. A. Eades, J. W. Steeds, and G. M. Racham, Phil. Trans. Roy. Soc., London, Vol. A281, No. 1, 1976, p. 71.
4. Marcinkowski, M. J., Electron Microscopy and Strength of Crystals, G. Thomas and J. Washburn, eds., Interscience, pp. 333-439, 1963.
5. Inoue, A., H. Tomioka, and T. Masumoto, Met. Trans. A., Vol. 14A, p. 1367, 1983.
6. Golightly, F. A., F. H. Stoot, and G. L. Wood, Oxidation of Metals, 1976, Vol. 10, No. 3, pp. 163-187.
7. Allam, I. M., D. P. Little, and J. Stringer, Oxidation of Metals, 1978, Vol. 12, pp. 35-66.
8. Zaplatynsky, I., Oxidation of Metals, 1977, Vol. 11, No. 6, pp. 289-305.
9. Smeggil, J. G., A. W. Funkenbusch, and N. S. Bornstein, High Temperature Science, 1985, Vol. 20, pp. 163-182.
10. Jacobson, D. M., Critical Materials in the Electrical and Electronics Industry, The Inst. of Metallurgists, p. 35, 1985.
11. Weinman, L. S., DeVault, J. N., and Moore, P., Applications of Lasers in Materials Processing, American Society for Metals, Metals Park, OH, pp. 245-257, April 1979.
12. Domashevskaya, E. P., Metallofizika, Vol. 7, No. 3, pp. 31-36, 1985.
13. Korotaev, A. D., et al., Fiz. Met. Metalloved., Vol. 54, No. 6, 1982.
14. Troitskii, B. S., et al., Izv. V. U. Z. Tsvetn. metall., Vol. 6, pp. 71-74, 1981.
15. Maksimovich, et al., Fiz. Khim, Mekh. mater., Vol. 4, pp. 82-86, 1984.
16. Oshima, M., et al., Solid State Communication, Vol. 46, No. 11, pp. 815-818, 1983.
17. Lyutyi, E. M., et al., Fiz. Khim, mekh. mater., Vol. 2, pp. 122-124, 1985.
18. Kozlov, A. T., et al., Izv. Akad. Nauk, SSSR, met., Vol. 3, pp. 182-186, 1985.
19. Belov, A. F., et al., Izv. Akad. Nauk, SSSR, met., Vol. 5, pp. 92-97, 1982.

20. Troitskii, B. S., et al., Sov. Nonferrous met. res., Vol. 9, No. 6, pp. 500-503, 1981.
21. Voitovich, R. V., et al., Russ. Met., Vol. 1, pp. 183-187, 1979.
22. Fedotov, A. R., Izv. Akad. Nauk, SSSR, met., Vol. 5, pp. 248-252, 1979.
23. Shatinskii, V. F., et al., Prot. met. (USSST), Vol. 15, No. 3, pp. 301-303, 1979.
24. Vasileva, E. V., et al., Tr. Moskov Vyssh Etkh Univ. NE Bauman, Vol. 214, pp. 63-67, 1976.
25. Perrin, C., Proc., Titanium '80 Science and Technology, 4th Int. Conf. on Ti, H. Kimuro and O. Izumi, eds., Vol. 4, pp. 2793-2802, 1980.
26. Jepson, K. S., Brown, A. R. G., and Gray, J. A., in The Science and Technology and Application of Titanium (Proc., First Int. Conf., or Titanium, London), Jaffee, R.I. and Promisel, N. E. (eds.), pp. 677-690, Pergonon Press, 1970.
27. Collings, E. W., The Physical Metallurgy of Titanium Alloys, American Society for Metals, 1984.
28. Bagariatskii, Yu. A., Nosova, G. I., and Tagunova, T. V., Sov. Phys. Dokl. 3, pp. 1014-1018, 1959 (Transl. of DOK. Akad. Nauk SSSR Vol. 122, pp. 593-596, 1958).
29. Williams, J. C., Proc. Second Int. Conf. on Titanium, Boston, Jaffee, R. I., and Burte, H. M. (eds.), pp. 1433-1439, Plenum Press, 1973.
30. Hickman, B. S., Trans. TMS-AMIE 245, pp. 1329-1335, 1969.
31. Flower, H. M., Davis, R., and West, D. R. F., Proc. Third Int. Conf. on Titanium, Moscow, Williams, J. C., and Belov, A. F. (eds.), Plenum Press, pp. 1703-1715, 1982.
32. Suryanarayana, C., A. Inoue, and T. Masumoto, Titanium' 80, Science and Technology, Proc. of the Fourth Int. Conf. on Titanium, H. Kimura and O. Izumi, eds., Vol. 1, pp. 699-707, 1980.

APPENDIX A

Accepted for Publication in Acta Metallurgica

ONE-DIMENSIONAL FINITE-MEDIUM DIFFUSION MODEL
FOR EXTENDED SOLID SOLUTION IN LASER CLADDING OF HF ON NICKEL

A. Kar and J. Mazumder
Laser Aided Materials Processing Laboratory
Department of Mechanical and Industrial Engineering
University of Illinois at Urbana-Champaign
1206 West Green Street
Urbana, IL 61801

Abstract

Inherent rapid solidification involved in laser cladding with pneumatic powder delivery leads to the formation of metastable alloys with extended solid solution. This has been experimentally observed for various binary, ternary and quaternary alloy systems. Composition of the alloys produced by laser cladding process often exceeds the solid solubility limit far beyond that expected from the equilibrium phase diagram. This paper presents a mathematical model for determining the composition of metastable alloys and the effects of various process parameters on the composition of extended solid solution for Ni-Hf binary alloy system. The cooling process of the molten cladding pool has been modeled by considering conduction of heat through the pool and the substrate. Both the pool and the substrate were taken to be one-dimensional and finite. Also the freezing point at the solid-liquid interface has been allowed to vary with concentration of the solute. The distribution of solute atoms in the cladding pool has been obtained using diffusion theory with non-equilibrium partitioning of solute at the solid-liquid interface. The governing partial differential equations for the temperature and the concentration fields have been reduced to a set of first-order ordinary non-linear differential equations using finite medium integral transforms and then solved by using Runge-Kutta method.

I. INTRODUCTION

Recent advances in laser technology have drawn considerable interest in using lasers for materials processing and manufacturing. Laser technology not only makes manufacturing processes simpler and more economical but also provides a unique way of modifying the surface chemistry of materials. Due to the inherent rapid heating and cooling rate in laser alloying and cladding processes, it is often possible to obtain novel materials without being restricted by equilibrium phase diagram. The high cooling rate results in extended solid solution to produce metastable alloys. Recently, laser cladding technique has been applied to increase the solid solubility of reactive elements such as Hf in nickel superalloy [1] for improved high temperature properties. Thus understanding of basic mechanism of extended solid solution in laser cladding will be useful. The mechanism of extended solubility encompasses the energy, momentum, and mass transport of solute atoms. The heating and cooling rates are determined by the heat transfer equation while the extent of mixing and the redistribution of solute atoms in the molten cladding pool are obtained from the momentum and mass transport equation. This paper presents a mathematical model for Ni-Hf binary alloys to calculate the composition of solute in the extended solid solution which is usually formed during laser cladding. It allows the construction of a non-equilibrium phase diagram of a given system from its equilibrium phase diagram.

There is very little information in the available literature on mathematical modeling of laser surface cladding and alloying with rapid cooling rate. As mentioned earlier, the composition of a rapidly cooled metastable alloy depends greatly on the heat transfer rate during the solidification process. Three-dimensional heat transfer models for various

material processing with CW laser were presented by several authors [2-5]. It was found experimentally that surface tension arising due to very high temperature gradient in laser melted pools causes convection. This aspect was modeled by Chan, et al. [6]. They studied the effects of surface tension on the cooling rate, surface velocity, surface temperature, and the pool shape. Chande and Mazumder [7] examined the distribution of solute by diffusion and convection in a laser melted pool after it was delivered to such a pool.

The problem of extended solid solution due to rapid cooling has been studied by various investigators using thermodynamic variables such as free energy and chemical potential. The thermodynamics of nonequilibrium solidification has been examined very well by Baker and Cahn [8]. Boettinger and Perepezko [9] discussed the process of rapid solidification from the thermodynamics point of view. Boettinger, et al. [10], also used the response function approach of Baker and Cahn [8] and stability analysis for microsegregation-free solidification. Further details on rapidly solidified materials can be found in Refs. [11,12]. In a recent paper [13], the authors have presented a model for extended solid solution during laser cladding by considering the cladding pool and the solid substrate semi-infinite and the freezing point of the cladding melt independent of the concentration of solute. The present study considers the width of the substrate and the cladding melt finite. Also, the dependence of freezing point of the cladding melt on the concentration of solute has been taken into account in this paper.

II. MATHEMATICAL MODEL

Process Physics

In laser cladding processes the substrate material to be clad is moved at a constant rate while the cladding powder is poured onto it using a pneumatic powder delivery system and melted simultaneously by a laser beam (see Fig. 1a). The uniform speed of the substrate and the constant feed rate of the cladding powder ensure uniform cladding thickness. The molten pool of the cladding material which forms just below the laser beam solidifies by dissipating heat to the surrounding air, adjacent cladding, and the solid substrate as it moves away from the laser beam. The shape of the cladding melt pool and the solidified cladding on the substrate is influenced by laser power, laser beam diameter, thermo-physical properties of the cladding powder and the substrate, temperature of the substrate, relative motion between the cladding powder delivery system and the substrate, the cladding powder feed rate and the interaction time between the cladding and the laser beam. In the present model the strip of cladding BCDEB (see Fig. 1a) is assumed to be semi-cylindrical in shape (see Fig. 1b) and based on this the initial pool mean temperature is determined (see Eq. (5)). The liquid cladding pool and the substrate were taken to have finite thickness in the positive direction of the x-axis and they are considered infinitely large in the other two directions (see Fig. 1c).

This paper is concerned with heat and mass transfer in the cladding melt ABCA to model extended solid solution during laser cladding. This liquid pool solidifies by conducting away heat to the substrate and to the solid cladding across AB and BC, respectively. Also, it loses some energy to the ambient inert gas across the free surface CA. The cladding BCDEB is formed from the liquid cladding melt just solidified and hence its temperature distribution is

almost uniform and equal to the temperature of the molten pool ABCA. So the heat loss across BC would be very little. Therefore, we can consider that the pool of cladding melt (ABCA) loses energy through the surfaces at AB and CA. To carry out one-dimensional heat transfer calculations we assume that the pool extends up to infinity along AB. Due to this assumption the cladding melt solidifies along AB and this freezing front moves upward in the direction of BC. The solid substrate has been considered to have finite width, but it is infinitely large along AB. The geometric configuration of this pool has been shown in Fig. 1c by rotating the pool 90 degrees in the clockwise direction. In this figure the freezing front has been shown to be planar. This is true when a pure metal solidifies. For a cladding melt of an alloy system, the freezing front develops curvature due to surface tension and also there could be dendrite and cellular growth at the solid-liquid interface. Moreover, rapid cooling may lead to nucleation in the bulk of the liquid phase. The stability criterion of Mullins and Sekerka [14] of a planar interface during solidification of a dilute binary alloy shows that the planar interface will be unstable for the nickel-hafnium system considered in this study. It was found [13] that there are dendrites which are very small in size. Nevertheless, the dendrites will affect the diffusion of solute atoms at the freezing front. However, to simplify the mass transfer analysis, the freezing front has been assumed to be planar due to the small size of dendrites. Moreover, the trend predicted by the model is more important than the exact numerical values due to the paucity of high temperature materials data and simplifying assumptions. Besides this the present model has been developed based on a few more assumptions listed below.

- (1) The thermal conductivity and the thermal diffusivity for a mixture is the sum of the volume-averaged value of the respective transport properties of each element of the mixture,
- (2) The mass diffusivity of each element in the liquid phase is the average value of self-diffusivity over the room temperature and the initial temperature with modified activation energy for the mixture,
- (3) The cladding pool and the substrate are in thermally perfect contact,
- (4) There is no mass diffusion in the solid phase,
- (5) The solute segregated at the solid-liquid interface moves into the liquid phase by diffusion only. This is because a boundary layer is formed near the interface where diffusion of solute atoms is dominant,
- (6) The cladding melt forms a uniform solution of composition equal to that of the cladding powder mixture before its solidification begins,
- (7) Only 50 percent of the laser energy is absorbed by the cladding material. Studies [12] show that the amount of laser energy absorbed by different materials is 37 to 60 percent.

With these assumptions, the one-dimensional heat conduction equations for the substrate, solidified cladding, and the liquid cladding regions are solved. The solutions of these heat transfer equations are used to obtain the velocity of the solid-liquid interface and then the mass transfer equation is solved to determine the distribution of solute atoms in the liquid phase. From this, the concentration of the solute atoms in the solid phase is computed by using an expression for nonequilibrium partition coefficient for dilute solution developed by Aziz [15].

Mathematical Formulations

In this section the governing heat conduction equations for energy transport in the substrate, solidified cladding, liquid cladding regions, and the mass transfer equation for diffusion of solute atoms in the liquid cladding pool are presented along with boundary and initial conditions. These equations have been solved using the integral transform technique. A systematic procedure to obtain the kernel of integral transform has been given. Since the problem involves a moving boundary due to solidification of cladding, the eigenfunction used for integral transform has time-varying eigenvalues. A general method of solution of moving boundary problems using variable eigenvalues has been discussed by Grindberg [16]. Özisik and Gruceri [17] followed a similar approach to obtain a solution to the phase change problem. Also Yener and Özisik [18] used the method of variable eigenvalues to solve for temperature distribution in multi-region finite media with time-varying heat transfer coefficient.

The governing equations for energy transport are

- (i) Solid substrate region

$$\frac{\partial^2 T_1'}{\partial x^2} = \alpha_1 \frac{\partial T_1'}{\partial t}; \quad t \geq 0, \quad 0 \leq x \leq a; \quad (1)$$

- (ii) Solidified cladding region

$$\frac{\partial^2 T_2'}{\partial x^2} = \alpha_2 \frac{\partial T_2'}{\partial t}; \quad t \geq 0, \quad 0 \leq x \leq S(t); \quad (2)$$

- (iii) Liquid cladding region

$$\frac{\partial^2 T_3'}{\partial x^2} = \alpha_3 \frac{\partial T_3'}{\partial t}; \quad t \geq 0, \quad s(t) \leq x \leq b. \quad (3)$$

The auxiliary conditions are

$$k_1 \frac{\partial T_1'}{\partial x} = h_1(T_1' - T_r) \quad \text{at } x = 0 \text{ and } t \geq 0, \quad (4a)$$

$$T_1'(a, t) = T_2'(a, t), \quad (4b)$$

$$k_1 \frac{\partial T_1'}{\partial x} = k_2 \frac{\partial T_2'}{\partial x} \quad \text{at } x = a \text{ and } t \geq 0, \quad (4c)$$

$$T_2'(s(t), t) = T_3'(s(t), t) = T_I(C_2, \dot{s}(t)), \quad (4d)$$

$$-k_3 \frac{\partial T_3'}{\partial x} = h_3(T_3' - T_r) \quad \text{at } x = b \text{ and } t \geq 0, \quad (4e)$$

$$k_2 \frac{\partial T_2'}{\partial x} - k_3 \frac{\partial T_3'}{\partial x} = \rho L \frac{ds}{dt} \quad \text{at } x = s(t) \text{ and } t \geq 0, \quad (4f)$$

and

$$s(0) = a. \quad (4g)$$

The initial conditions for the above problems are obtained from the following considerations.

The cladding has been assumed to melt almost instantaneously as soon as it is exposed to the laser beam to reach a uniform temperature \bar{T}_2 . \bar{T}_2 is calculated by taking a lumped-parameter energy balance of the laser energy imparted to the cladding and the energy required to melt the cladding powder and raise its temperature to \bar{T}_2 . This yields the following expression for \bar{T}_2 :

$$\bar{T}_2 = T_r + \frac{1}{C_p} \left[\frac{2pf}{\pi r_c^2 v_p} - L \right]. \quad (5)$$

This expression is derived by considering the cladding to be formed in the shape of a semi-cylindrical strip (see Fig. 1b). To obtain the initial condition for the solid substrate, a linear temperature profile has been constructed between the temperature \bar{T}_2 at $x = a$ and T_r at $x = 0$. Thus the initial conditions are

$$T_1'(x,0) = (\bar{T}_2 - T_r) \frac{x}{a} + T_r \quad (6a)$$

and

$$T_3'(x,0) = \bar{T}_2. \quad (6b)$$

The eigenfunctions used in the integral transform technique satisfy homogeneous boundary conditions and they lead to nonuniformly convergent solution if the boundary conditions are not homogeneous. Since the present problem has nonhomogeneous boundary conditions, the following substitution is made to transform them into homogeneous boundary conditions in order to obtain uniformly convergent solution. Let

$$T_1(x,t) = T_1'(x,t) - T_r,$$

$$T_2(x,t) = T_2'(x,t) - T_r,$$

and

$$T_3(x,t) = T_3'(x,t) - T_r.$$

When these equations are substituted into the governing differential equations (1) through (3), the boundary conditions (4a) through (4g), the initial conditions (6a) and (6b) and $\tau(x,t)$ is chosen such that

$$\frac{\partial^2 \tau}{\partial x^2} = R(t) \quad (7)$$

where $R(t)$ is an arbitrary function of time to be determined later and $\tau(x,t)$ is subject to the conditions

$$\left. \begin{aligned} -k_3 \frac{\partial \tau}{\partial x} &= \rho L s \\ & \end{aligned} \right\} \text{ at } x = s(t) \quad (8a)$$

$$\tau(x,0) = 0$$

and

$$-k_3 \frac{\partial \tau}{\partial x} = h_3 \tau \text{ at } x = b \quad (8b)$$

the following problem is obtained

$$\frac{\partial^2 T_1}{\partial x^2} = \frac{1}{\alpha_1} \frac{\partial T_1}{\partial t}, \quad (9a)$$

$$\frac{\partial^2 T_2}{\partial x^2} = \frac{1}{\alpha_2} \frac{\partial T_2}{\partial t}, \quad (9b)$$

and

$$\frac{\partial^2 T_3}{\partial x^2} = \frac{1}{\alpha_3} \left(\frac{\partial T_3}{\partial t} + \frac{\partial \tau}{\partial t} \right) - R(t) \quad (9c)$$

subject to

$$k_2 \frac{\partial T_2}{\partial x} - k_3 \frac{\partial T_3}{\partial x} = 0 \text{ at } x = s(t), \quad (10a)$$

$$k_1 \frac{\partial T_1}{\partial x} = h_1 T_1 \text{ at } x = 0, \quad (10b)$$

$$T_1(a,t) = T_2(a,t), \quad (10c)$$

$$k_1 \frac{\partial T_1}{\partial x} = k_2 \frac{\partial T_2}{\partial x} \text{ at } x = a, \quad (10d)$$

$$T_2(x,t) = T_3(x,t) = T_I - T_r \text{ at } x = s(t), \quad (10e)$$

$$-k_3 \frac{\partial T_3}{\partial x} = h_3 T_3 \text{ at } x = b, \quad (10f)$$

$$T_1(x,0) = (\bar{T}_2 - T_r) \frac{x}{a}, \quad (10g)$$

and

$$T_3(x,0) = T_2 - T_r - R(0) \frac{x}{2} - A(0)x - B(0) \quad (10h)$$

where $A(0)$, $B(0)$, and $R(0)$ are computed from the functions $R(t)$, $A(t)$, and $B(t)$ which arise in the solution

$$\tau(x,t) = R(t) \frac{x^2}{2} + A(t)x + B(t) \quad (11)$$

of Eq. (7) and given by, due to the constraints (8a) and (8b),

$$R(t) = \frac{\rho L}{k_3} \left(\frac{\dot{s}}{b-s} \right) \left(\frac{1+2\tau_1}{1+\tau_1} \right), \quad A(t) = -Rs - \frac{\rho L \dot{s}}{k_3}$$

$$B(t) = -R \frac{s^2}{2} - As, \quad \text{and} \quad \tau_1 = \frac{h_3}{2k_3} (b-s).$$

The governing equations, Eqs. (9a-c) can be rewritten as

$$\frac{\partial^2 T_i}{\partial x^2} = \frac{1}{\alpha_i} \frac{\partial T_i}{\partial t} + \epsilon_i \left[\frac{1}{\alpha_3} \left(R \frac{x^2}{2} + Ax + B \right) - R(t) \right] \quad (12)$$

for $i = 1, 2, 3$ which represents the substrate, solidified cladding, and the liquid region, respectively, and $\epsilon_1 = \epsilon_2 = 0$ and $\epsilon_3 = 1$.

To obtain the kernels $K_i(x,t)$, $i = 1, 2, 3$ of integral transform for the above problem, let us operate Eq. (12) with

$$\sum_{i=1}^3 \int_{a_i}^{b_i} \bar{w}_i K_i(x,t) dx$$

where \bar{w}_i is a weight function for the i -th region and it will be determined later. Also, $a_1 = 0$, $a_2 = a$, $a_3 = s(t)$, $b_1 = a$, $b_2 = s(t)$ and $b_3 = b$.

The above operation on Eq. (12) yields

$$\sum_{i=1}^3 \int_{a_i}^{b_i} \frac{\partial^2 T_i}{\partial x^2} \bar{w}_i K_i(x,t) dx = \sum_{i=1}^3 \int_{a_i}^{b_i} \frac{\partial T_i}{\partial t} \bar{w}_i K_i(x,t) dx$$

$$+ \int_{s(t)}^b \bar{w}_3 K_3(x,t) \epsilon_i \left[\frac{1}{\alpha_3} \left(\dot{R} \frac{x^2}{2} + A\dot{x} + \dot{B} \right) - R(t) \right] dx. \quad (13)$$

Integrating the left-hand side of the above equation by parts twice, using Leibnitz's rule to interchange the integral and the derivative operators in the first term on the right-hand side of Eq. (13), one gets the following set of ordinary nonlinear first-order differential equations:

$$\frac{d}{dt} \bar{T}_n(t) + \lambda_n^2 \bar{T}_n(t) = \sum_{i=1}^3 \int_{a_i}^{b_i} \bar{w}_i T_i \frac{\partial K_{i,n}}{\partial t} dx$$

$$- \int_{s(t)}^b k_3 K_{3,n}(x,t) \frac{1}{\alpha_3} \left(\dot{R} \frac{x^2}{2} + A\dot{x} + \dot{B} - \alpha_3 R \right) dx \quad (14)$$

for $n = 1, 2, \dots, \infty$, and subject to the initial conditions

$$\bar{T}_n(0) = \sum_{i=1}^3 \int_{a_i}^{b_i} w_i T_i(x,0) K_{i,n}(x,0) dx.$$

where

$$w_i = k_i / \alpha_i.$$

To arrive at the Eq. (14), all the boundary conditions have been applied, the weight function \bar{w}_i , the kernel of integral transform $K_i(x,t)$, the integral transform variable $\bar{T}_n(t)$, and the associated weight function w_i have been chosen in the following way:

$$\bar{w}_i = k_i$$

$$\frac{d^2 K_i}{dx^2} = -\frac{\lambda^2(t)}{\alpha_i} K_i, \quad i = 1, 2, 3 \quad (15)$$

subject to the following boundary conditions:

$$\frac{dK_1}{dx} = \frac{h_1}{k_1} K_1 \quad \text{at } x = 0$$

$$K_1 = K_2 \quad \left. \vphantom{K_1} \right\} \quad \text{at } x = a$$

$$k_1 \frac{dK_1}{dx} = k_2 \frac{dK_2}{dx}$$

$$K_2 = K_3 \quad \left. \vphantom{K_2} \right\} \quad \text{at } x = s(t)$$

$$k_2 \frac{dK_2}{dx} = k_3 \frac{dK_3}{dx}$$

$$-\frac{dK_3}{dx} = \frac{h_3}{k_3} K_3 \quad \text{at } x = b$$

and

$$\bar{T}_n(t) = \sum_{i=1}^3 \int_{a_i}^{b_i} w_i T_i(x,t) K_{i,n}(x,t) dx \quad (16)$$

The inverse transform of the above integral transform, Eq. (16), is

$$T_i(x,t) = \sum_{n=1}^{\infty} \frac{1}{N_n} \bar{T}_n(t) K_{i,n}(x,t) \quad (17)$$

where the normalizing constant N_n is evaluated from

$$N_n = \sum_{i=1}^3 \int_{a_i}^{b_i} w_i (K_{i,n}(x,t))^2 dx. \quad (18)$$

For an expression of $K_i(x,t)$, Eq. (15) is solved to obtain

$$K_i(x,t) = E_i \sin\left(\frac{\lambda(t)x}{\sqrt{\alpha_i}}\right) + F_i \cos\left(\frac{\lambda(t)x}{\sqrt{\alpha_i}}\right). \quad (19)$$

When all the boundary conditions on $K_i(x,t)$ are satisfied, the eigenvalues are obtained from the following equation:

$$\det M = 0$$

where $\det M$ represents the determinant of a 6×6 matrix M . The elements of this matrix M_{jk} for $j = 1, 2, \dots, 6$ and $k = 1, 2, \dots, 6$ have been given in the Appendix. The constants of integration E_j and F_j 's are obtained from a set of algebraic equations given by

$$[G] [H] = [N]$$

where $[G]$ is a 4×4 matrix, $[H]$ and $[N]$ are column vectors of four elements each. These elements have been defined in the Appendix. To obtain the four algebraic equations given by the above matrix equation, F_1 has been set equal to unity and this implies

$$E_1 = \frac{h_1 \sqrt{\alpha_1}}{\lambda k_1}$$

When the eigenvalues and the constants of integration E_i and F_i 's are determined, the kernel of integral transform $K_{i,n}(x,t)$ is completely known. $K_{i,n}(x,t)$ can be substituted into the Eq. (14) and then the resulting set of first-order ordinary nonlinear differential equations can be solved using the Runge-Kutta method. These equations are to be solved in conjunction with the equations for mass transfer since they are coupled by the condition at the solid-liquid interface given by

$$T_I - T_r = T_3(s(t), t) = \sum_{n=1}^{\infty} \frac{1}{N_n} \bar{T}_n(t) [E_3 \sin(\lambda_n s / \sqrt{\alpha_3}) + F_3 \cos(\lambda_n s / \sqrt{\alpha_3})] \quad (22)$$

This equation is solved to determine the location of the freezing front $s(t)$. In this equation the interface temperature T_I depends on concentration. The following expression for T_I as derived by Boettinger and Perepezko [9] has been used in this model

$$T_I = T_m^* + m_\ell C_\ell^* + \frac{m_\ell C_\ell^*}{1 - k_e} (k_e - k^* (1 - \lambda_n \frac{k^*}{k_e})) + \frac{m_\ell}{1 - k_e} \frac{\dot{s}(t)}{v_0} \quad (23)$$

Here v_0 represents the velocity of sound in the liquid phase. The velocity of sound in a medium depends on its temperature and composition. In this study v_0 has been taken to be equal to the velocity of sound in the pure solvent. T_m^* and m_ℓ are determined from the equilibrium phase diagram by taking a segment of the liquidus around the point of interest. This segment is considered linear whose slope and intercept with the temperature axis are m_ℓ and T_m^* respectively. C_ℓ^* is obtained by evaluating $C(x,t)$ at $x = s(t)$ and by expres-

sing it in terms of mole fraction.

The concentration dependence of T_I couples the energy equations (14) with the mass transfer equation and hence they must be solved simultaneously. The diffusion of solute atoms in the cladding melt pool is governed by the following mass transfer equation

$$\frac{\partial^2 C}{\partial x^2} = \frac{1}{\bar{D}} \frac{\partial C}{\partial t} \quad (24)$$

subject to the following initial and boundary conditions

$$C(x,0) = C_0, \quad (25a)$$

$$-\bar{D} \frac{\partial C}{\partial x} = 0 \text{ at } x = b, \quad (25b)$$

and

$$-\bar{D} \frac{\partial C}{\partial x} = \dot{s}(t) [k^*(t) - 1] C(x,t) \text{ at } x = s(t). \quad (25c)$$

Here again the method of integral transform with variable eigenvalues is used to solve the above mass transfer problem. The kernel of integral transform for this problem can be obtained using the procedure used for the heat transfer equations, except that here we are concerned with only region. The kernel for the above problem is

$$\phi(x,t) = \cos(u(t)(b-x)) \quad (26)$$

and the eigenvalues are given by the following transcendental equation

$$\mu [\mu \sin(\mu(b-s)) - \frac{\dot{s}(k^*-1)}{\bar{D}} \cos(\mu(b-s))] = 0. \quad (27)$$

Applying the operator

$$\int_{s(t)}^b dx \phi_n(x,t)$$

to the governing Eq. (14) and integrating the left-hand side twice by parts, using Leibnitz's rule on the right-hand side, and making use of all the boundary conditions, one obtains the following set of coupled and nonlinear first order ordinary differential equations:

$$\frac{d\bar{C}_n(t)}{dt} + \bar{D}_n^2(t)\bar{C}_n(t) = H_{m,n}(t) - \phi_n(s(t),t) \dot{s}(t) \sum_{m=0}^{\infty} \frac{1}{N_m} \bar{C}_m(t) \phi_m(s(t),t)$$

$$\text{for } n = 1, 2, 3, \dots, \infty, \text{ and} \quad (28)$$

subject to the initial conditions

$$\bar{C}_n(0) = \int_a^b dx C_0 \cos(\mu(x-b))$$

where

$$H_{m,n}(t) = -\sum_{m=0}^{\infty} \frac{\bar{C}_m(t)}{N_m} \int_{s(t)}^b dx \phi_m(x,t) \sin(\mu_n(x-b)) \dot{\mu}_n(t)(x-b)$$

$$\bar{C}_n(t) = \int_{s(t)}^b dx \phi_n(x,t) C(x,t). \quad (29)$$

The inverse transform of the integral transform, Eq. (29), is given by

$$C(x,t) = \sum_{n=0}^{\infty} \frac{1}{N_n} \bar{C}_n(t) \phi_n(x,t) \quad (30)$$

with the normalizing constant obtained from

$$N_n = \int_{s(t)}^b \phi_n^2(x,t) dx.$$

The partition coefficient, normally defined as the ratio of the concentration of solute in the solid phase to that in the liquid phase at the solid-liquid interface is constant for equilibrium solidification. When solidification progresses rapidly, it is no longer constant. For rapid cooling rate, the partition coefficient $k^*(t)$ has been derived by Aziz [15] which is

$$k^*(t) = \frac{C_s}{C_l} = \frac{\beta + k_e}{\beta + 1} \quad (31)$$

where $\beta = \dot{s}(t)\lambda/D^*$. In the present model the interdiffusivity D^* is taken to be equal to the mass diffusivity \bar{D} and the interatomic distance λ is taken to be 4\AA , which is the average diameter of an atom. To use the expression (31) for determining the concentration of solute in the solid phase at the solid-liquid interface, we have to know $\dot{s}(t)$ and C_l . For this, Eq. (22) and its time-derivative are solved for $s(t)$ and $\dot{s}(t)$ respectively. Similarly, C_l is obtained from Eq. (30) by evaluating $C(x,t)$ at $x = s(t)$.

III. RESULTS AND DISCUSSION

Experimental Verification

The results of the above model were compared with experimental data. Laser cladding was performed on nickel substrate with a mixture of Ni-Hf powder of nominal composition, 74% Ni and 26% Hf by weight. The laser power, laser beam diameter and the speed of workpiece were 5 kW, 3 mm, and 50 inch/min., respectively, and the initial pool mean temperature (T_2) was found to be 1862°K. The solid substrate was clad with the above cladding material which takes the shape of an approximately semi-cylindrical strip of metal on the substrate (see Fig. 1b). Electron Probe Micro-Analysis (EPMA) and Scanning Transmission Electron Microscope (STEM) analysis of these samples show the concentration of Hf in the matrix of Ni in excess of that predicted by the equilibrium phase diagram. These experimental results show 3.58 to 6.5 wt.% in the Ni matrix. A small fraction of the Ni-Hf alloy was found experimentally to contain 9.3% (by wt.) Hf in the Ni matrix. Fine distribution of undissolved Hf-particles and the difference in the electron beam diameter of the two instruments are probably the source of such a large fluctuation.

The theoretical results predicted by this model is 7.15 wt.% Hf in the Ni-Hf alloy. The prediction of composition of the extended solid solution based on the present model is within 9 percent of the experimental results when compared with the maximum value (6.50 percent) of Hf concentration. This discrepancy may be due to some of the assumptions of this model. For example, it has been assumed that all of the solute dissolves in the solvent before the cladding melt starts solidifying. But the time it takes to melt and freeze the cladding powder may not be sufficient for dissolution of all solute atoms to occur. Also the present model utilizes an expression, Eq. (31), for the nonequilibrium partition coefficient which is applicable to dilute solution.

Apart from these conditions, the presence of a two-phase zone between the solidus and the liquidus lines and the surface tension driven flow causing convection in the liquid pool will affect the mixing of solute in the liquid phase and thus alter its composition in the solid phase. Paucity of high temperature liquid metal data also contributes to the numerical error. However, the objective of this study is to determine the trend of, and thus understand, the underlying process physics.

Parametric Results

The above model was used to study the effect of various important process parameters such as laser power, laser-cladding interaction time, cladding thickness, cladding powder delivery rate on the composition of hafnium in nickel matrix. Results were obtained for ambient temperature $T_r = 293^\circ\text{K}$ and the heat transfer coefficients $h_1 = 1 \text{ Watt/cm}^2\text{-}^\circ\text{K}$ and $h_2 = 0.01 \text{ Watt/cm}^2\text{-}^\circ\text{K}$. The laser power was fixed at 5, 6, and 7 kW. For each power of laser, the speed of the workpiece was varied as 40, 50, and 60 inches/min. Since the transport properties depend on temperature, average values, which are calculated according to formulas of Ref. [13], were used in this model.

Results obtained from this study have been presented in Figs. 2 through 12. Figure 2 shows the concentration of hafnium (in wt. %) in a nickel matrix for different values of laser power and cladding thickness measured in units of laser beam diameter. The laser beam diameter used in this study is 3 mm. As can be seen from this figure, the concentration of hafnium increases with cladding thickness for a given speed of the workpiece and laser power. This is due to the fact that the initial pool mean temperature, \bar{T}_2 , varies inversely with the cladding thickness as evident from Eq. (5). The closer is \bar{T}_2 to the melting point of the cladding powder the higher would be the

cooling rate and this will result in a higher concentration of solute in the solid phase. This was discussed in detail by Kar and Mazumder [13]. However, it would be erroneous to conclude that one can enrich the solid phase with solute to any concentration by increasing the cladding thickness indefinitely for a given laser power and a given speed of the workpiece. There is a critical value of the cladding thickness at which \bar{T}_2 becomes equal to the melting point of the cladding powder for a given workpiece speed and laser power. This critical cladding thickness can be obtained from Eq. (5). If the cladding thickness is greater than this critical value, then there will be some unmelted powder between the substrate and the cladding melt and hence the substrate will not be clad. Thus for a given workpiece speed and laser power, the concentration of solute in the solid phase increases with cladding thickness as long as it is lower than the critical thickness value.

Figure 3 shows the variation of initial pool mean temperature with respect to the cladding thickness per unit laser beam diameter for different values of laser power. Figures 4 and 5 are concerned with the variation of solute concentration in the solid phase and the initial pool mean temperature with the cladding powder feed rate. The cladding powder feed rate is determined by using the expression $1/3 - \pi r_c^2 v_D$ and assuming that the cladding takes the shape of a semi-cylindrical strip (see Fig. 1b). Cladding powder feed rate is a very important process parameter since it is related to cladding thickness and velocity of the workpiece as well as the initial pool mean temperature. Thus if the powder delivery rate is known, then \bar{T}_2 can be obtained from the Fig. 5 and the concentration of solute can be obtained from the Fig. 4 and then the velocity of the workpiece can be selected for a desired cladding thickness. Figures 6 and 7 indicate the effect of specific laser energy on solute concentration in the solid phase and on the initial

pool mean temperature. Specific laser energy is defined as laser power required to produce a cladding of unit mass per unit time. It is determined by the relation $P/(\frac{1}{2}\pi r_c^2 v_D)$. The importance of selecting specific laser energy as a parameter is that it allows representation of the solute concentration data for any combination of laser power, workpiece speed, and cladding thickness parameters on one graph. This is because the initial pool mean temperature is proportional to specific laser energy. Thus the initial pool mean temperature and hence the thermal characteristic of the cladding melt pool will not be different as long as the laser specific energy remains the same for any choice of the process parameters. The effect of initial pool mean temperature on the solute concentration in the solid phase is shown in Fig. 8. It can be seen from this figure that the the concentration decreases with an increase in temperature for reasons explained above.

The effect of another important process parameter, laser-materials interaction time, on the solute concentration and the initial pool mean temperature is shown in Figs. 9 and 10 for different values of laser power. Interaction time is defined as the ratio of laser beam diameter to the speed of the workpiece. It can be observed that the trends of the graphs with respect to laser-material interaction time are opposite to those observed with respect to cladding thickness. This is because thin cladding leads to higher initial pool mean temperature than what is obtained as interaction time decreases provided other process parameters are kept unchanged. We have also seen that the solute concentration in the solid phase is higher at a lower initial pool mean temperature. This explains why the solute concentration curves with respect to the interaction time should be opposite to those which are plotted with respect to the cladding thickness.

Finally, the solidus temperature versus the solidus concentration of Hf has been plotted in Fig. 11 different laser powers. It is natural to expect that for a given solidus temperature, there should be a unique value of the solidus concentration of solute irrespective of how the process parameters are selected. This emphasizes the fact that the temperature versus concentration curves obtained for different process parameters must overlap. As can be seen from the Fig. 11, these curves are very close to each other. A possible reason for them not overlapping would be the rounding error during various stages of computations for different input values representing different process parameters. The Fig. 12 shows the nonequilibrium phase diagram computed by using this model. The characterizing parameters for this figure have been presented in Table 1. The deviation of nonequilibrium phase diagram from the equilibrium one shows the extension of solid solubility that can be obtained during laser cladding. The nonequilibrium phase diagram has been plotted in the neighborhood of the melting point of the cladding powder because the value of k_e used in the expression for nonequilibrium partition coefficient (Eq. (31)) corresponds to this melting point. It can be seen from the Fig. 12 that the width of the solid-liquid region between the equilibrium solidus and liquidus has reduced considerably. The nonequilibrium solidus line of this figure shows the extension of Hf concentration in Ni that can be obtained due to the rapid cooling in laser cladding. This phenomenon can be understood from the fact that the equilibrium phase diagram of Ni-Hf has a negative slope at the point which corresponds to the nominal composition of the cladding powder. Due to this, Hf is rejected from the Ni matrix when the solution of Ni-Hf solidifies and this results in increasing the concentration of Hf in the liquid phase. But since the solid phase retains more Hf than its equilibrium composition, the liquid phase will have less Hf than the equilib-

rium value and hence the extended solid solution (that is, the nonequilibrium) phase diagram will shrink.

Table 1 Solidus Composition of Hf, Solidus/Liquidus Temperature at the Substrate-cladding Interface and the Speed of Solidification at this Interface

Composition of Hf (wt%)	Solidus/Liquidus Temperature (K)	Interface Speed (cm/sec)
3.19	1505	3.26
4.83	1499	2.88
6.23	1489	2.74
7.15	1480	2.68
9.58	1453	2.55

IV. CONCLUSIONS

The present work examines the extension of solid solubility based on the transport of energy and mass. Solute transport has been considered to take place only in the liquid phase while the energy transport has been considered in both solid and liquid phases. The effect of nonequilibrium cooling rate on solute segregation at the freezing front has been taken into account by considering a nonequilibrium partition coefficient. Using this, the mass transfer problem has been solved for solute distribution in the liquid phase and the heat transfer problem has been solved to obtain the velocity of the solid-liquid interface, its location, and the freezing temperature of the interface. These mathematical solutions have been utilized to study the effect of various process parameters on the concentration of solute in an alloy. The hafnium concentration in the nickel-hafnium alloy is found to be higher for lower initial pool mean temperature (which implies a higher cooling rate) and also it is found that more laser energy is required to obtain an alloy of a given composition at a higher powder delivery rate than that for a lower rate of powder delivery.

It is found that the same composition of solute is obtained in the alloy for different cladding thicknesses by varying the laser power and the speed of the workpiece. This is because the initial pool mean temperature of the cladding material and hence the cooling rate are the same even through other parameters are different. Thus it can be concluded that the choice of the initial pool mean temperature determines the composition of the alloy. Since initial pool mean temperature is directly proportional to specific laser energy, when the initial temperature of the cladding melt is fixed or the specific laser energy is selected other process parameters can be determined by selecting any two of the three parameters, r_c , v , and P and the third one

will then have to be determined from Eq. (5). The composition of solute in the solid phase can be represented by a single curve for all possible values of the process parameters if it is plotted against the specific laser energy or the initial pool mean temperature. The effect of laser-cladding interaction time on solute concentration in the alloy and on the initial pool mean temperature is found to be opposite to that of cladding thickness. Also, it has been found that if the equilibrium liquidus has a negative slope at the nominal composition of the cladding powder, then the nonequilibrium phase diagram shrinks from the equilibrium phase diagram, resulting in a thin solid-liquid region between the solidus and the liquidus.

ACKNOWLEDGEMENTS

This work was made possible by a grant (AFOSR: 85-0333) from the U.S. Air Force Office of Scientific Research. Continued encouragement from the program managers, Dr. A. Rosenstein and Major J. Hagar is appreciated. The authors appreciate the help provided by Dr. J. Singh for the necessary experimental data. They also acknowledge Dr. W. J. Boettinger's critical reading of the manuscript and useful comments.

NOMENCLATURE

a	width of the substrate
b	width of the substrate and the cladding melt
B	Laser beam diameter
C	Concentration of solute in the liquid phase
C_l	Concentration of solute in the liquid phase at the solid-liquid interface
C_p	Average specific heat of the cladding material
C_s	Concentration of solute in the solid phase at the solid-liquid interface
C_l^*	Concentration (mole fraction) of solute in the liquid phase at the solid-liquid interface
\bar{D}	Average mass diffusivity of solute in the liquid phase
D^*	Interdiffusivity of solute at the interface
f	Fraction of laser energy absorbed by the cladding material
h_1	Heat transfer coefficient at the substrate boundary
h_3	Heat transfer coefficient at the cladding surface boundary
k_e	Equilibrium partition coefficient
k^*	Nonequilibrium partition coefficient
k_i	Thermal conductivity of the i -th region
L	Latent heat of fusion of the cladding material
m_l	Liquidus slope ($^{\circ}\text{K}/\text{mole fraction of solute}$)
P	Laser power
q	Rate of cladding powder delivery
r_c	Radius of the semi-cylindrical strip of cladding
s	Position of the solid-liquid interface
\bar{T}_2	Initial pool mean temperature

T_i	Temperature of the i-th region
T_I	Temperature at the solid-liquid interface
T_r	Ambient temperature
T_m^*	Intercept of liquidus line on temperature axis
v	Speed of the workpiece
v_0	Speed of sound in the cladding melt

Greek Symbols

α_i	Average thermal diffusivity in the i-th region
β	A non-dimensional parameter defined as $\dot{S}(t)\lambda/D^*$
λ	Interatomic distance
ρ	Average density of the cladding material

Subscripts

i 1, solid substrate; 2, solidified cladding; 3, liquid cladding.

REFERENCES

1. Singh, J., and Mazumder, J., "Effect of Extended Solid Solution of Hf on the Microstructure of the Laser Clad Ni-Fe-Cr-Al-Hf Alloys," Acta Metallurgica (accepted for publication).
2. Mazumder, J., and Steen, W. M., "Heat Transfer Model for CW Laser Material Processing," J. Appl. Phys., Vol. 51, 1980, pp. 941-947.
3. Cline, E., and Anthony, T. R., "Heat Treating and Melting Material with a Scanning Laser or Electron Beam," J. Appl. Phys., Vol. 48, 1977, pp. 3895-3900.
4. Kou, S., Hsu, S. C., and Mehrabian, R., "Rapid Melting and Solidification of a Surface Due to a Moving Heat Flux," Met. Trans. B., Vol. 12B, 1981, pp. 33-45.
5. Ashby, M. F., and Easterling, K. E., "The Transformation Hardening of Steel Surfaces by Laser Beams-I. Hypo-eutectoid Steels," Acta Met., Vol. 32, 1984, pp. 1935-1948.
6. Chan, C., Mazumder, J., and Chen, M. M., "A Two-Dimensional Transient Model for Convection in Laser Melted Pool," Met. Trans. A, Vol. 15A, 1984, pp. 2175-2183.
7. Chande, T., and Mazumder, J., "Two-Dimensional, Transient Model for Mass Transport in Laser Surface Alloying," J. Appl. Phys., Vol. 57, 1985, pp. 2226-2232.
8. Baker, J. C., and Cahn, J. W., "Thermodynamics of Solidification," in Solidification, ASM, Metals Park, OH, 1971, pp. 23-58.
9. Boettinger, W. J., and Perepezko, J. H., "Fundamentals of Rapid Solidification," Proc., Rapidly Solidified Crystalline Alloys, TMS-AIME, NJ, May 2-3, 1985.
10. Boettinger, W. J., Coriell, S. R., and Sekerka, R. F., "Mechanism of Microsegregation-free Solidification," Mat. Sci., Eng., Vol. 65, 1984, pp. 27-36.
11. Kear, B. H., Giessen, B. C., and Ghen, M. (eds.), "Rapidly Solidified Amorphous and Crystalline Alloys," Proc. MRS, Vol. 8, Boston, MA, Nov. 1981.
12. Li, L. J., and Mazumder, J., "A Study of the Mechanism of Laser Cladding Processes," Laser Processing of Materials (eds., K. Mukherjee, and J. Mazumder), Proc. Metal. Soc. AIME, Los Angeles, CA, 1984, pp. 35-50.
13. Kar, A., and Mazumder, J., "One-Dimensional Diffusion Model for Extended Solid Solution in Laser Cladding," J. Appl. Phys. Vol. 61, No. 7, pp. 2645-2655.

14. Mullins, W. W., and Sekerka, R. F., "Stability of a Planar Interface During Solidification of a Dilute Binary Alloy," J. Appl. Phys., Vol. 35, 1964, pp. 444-451.
15. Aziz, M. J., "Model for Solute Redistribution during Rapid Solidification," J. Appl. Phys., Vol. 53, 1982, pp. 1158-1168.
16. Grinberg, G. A., "A Method of Approach to Problems of the Theory of Heat Conduction, Diffusion and the Wave Theory and Other Similar Problems in Presence of Moving Boundaries and its Applications to Other Problems," J. Appl. Math. Mech., Vol. 31, No. 2, 1967, pp. 215-224.
17. Özisik, M. N., and Güçeri, S. I., "A Variable Eigenvalue Approach to the Solution of Phase-Change Problems," Can. J. Chem. Eng., Vol. 55, 1977, pp. 145-148.
18. Yener, Y., and Özisik, M. N., "On the Solution of Unsteady Heat Conduction in Multi-Region Finite Media with Time-Dependent Heat Transfer Coefficient," Proc., 5th Int. Heat Transfer Conf., Tokyo, Sept. 3-7, 1974, Vol. I, pp. 188-192.

APPENDIX

The elements of the matrices M and G and the column vectors H and N have been given below:

$$M_{11} = a_1 \lambda, M_{12} = -\frac{h_1}{k_1}, M_{13} = M_{14} = M_{15} = M_{16} = 0$$

$$M_{21} = \sin A_1, M_{22} = \cos A_1, M_{23} = -\sin A_2, M_{24} = -\cos A_2, M_{25} = M_{26} = 0$$

$$M_{31} = a_1 \cos A_1, M_{32} = -a_1 \sin A_1, M_{33} = -\frac{a_2 k_2 \cos A_2}{k_1}, M_{34} = \frac{a_2 k_2 \sin A_2}{k_1}, M_{35} = M_{36} = 0$$

$$M_{41} = M_{42} = 0, M_{43} = \sin S_2, M_{44} = \cos S_2, M_{45} = -\sin S_3, M_{46} = -\cos S_3$$

$$M_{51} = M_{52} = 0, M_{53} = a_2 \cos S_2, M_{54} = -a_2 \sin S_2, M_{55} = -\frac{a_3 k_3 \cos S_3}{k_2}, M_{56} = \frac{a_3 k_3 \sin S_3}{k_2}$$

$$M_{61} = M_{62} = M_{63} = M_{64} = 0, M_{65} = -a_3 \lambda \cos S_3 - \frac{h_3 \sin S_3}{k_3}, M_{66} = a_3 \lambda \sin S_3 - \frac{h_3 \cos S_3}{k_3}$$

where $a_i = 1/\sqrt{\alpha_i}$, $i = 1, 2, 3$, $A_i = a_i \lambda a$ for $i = 1, 2$,

$S_i = a_i \lambda s$ for $i = 2, 3$, and $B_3 = a_3 \lambda b$

The elements G_{jk} , $j = 1, \dots, 4$ and $k = 1, \dots, 4$ for the matrix [G] are given by

$$G_{11} = -\sin A_2, G_{12} = -\cos A_2, G_{13} = G_{14} = 0$$

$$G_{21} = -\frac{a_2 k_2 \cos A_2}{k_1}, G_{22} = \frac{a_2 k_2 \sin A_2}{k_1}, G_{23} = G_{24} = 0$$

$$G_{31} = \sin S_2, G_{32} = \cos S_2, G_{33} = -\sin S_3, G_{34} = -\cos S_3$$

$$G_{41} = G_{42} = 0, G_{43} = -a_3 \cos B_3 - \frac{h_3 \sin B_3}{\lambda k_3}, G_{44} = a_3 \sin B_3 - \frac{h_3 \cos B_3}{\lambda k_3}$$

The four elements of the column vector H are

$H_1 = E_2, H_2 = F_2, H_3 = E_3, H_4 = F_3$ and the elements of the column vector N are

$$N_1 = -\cos A_1 - \frac{h_1 \sin A_1}{a_1 \lambda k_1} \quad N_2 = a_1 \sin A_1 - \frac{h_1 \cos A_1}{\lambda k_1} \quad N_3 = N_4 = 0$$

LIST OF FIGURES

- Figure 1(a) Schematic diagram of laser surface cladding
(b) Three-dimensional view of the cladding and the substrate
(c) Geometric configuration used in the present model.
The model substrate and the solidification of the model cladding have been shown after rotating the pool ABCA (see Fig. 1a) by 90° clockwise
- Figure 2 Concentration of hafnium in the extended solid solution of nickel-hafnium versus cladding thickness per unit laser beam diameter
- Figure 3 Initial pool mean temperature of nickel-hafnium versus cladding thickness per unit laser beam diameter
- Figure 4 Concentration of hafnium in the extended solid solution of nickel-hafnium versus cladding powder feed rate
- Figure 5 Initial pool mean temperature of nickel-hafnium versus cladding powder feed rate
- Figure 6 Concentration of hafnium in the extended solid solution of nickel-hafnium versus specific laser energy
- Figure 7 Initial pool mean temperature of nickel-hafnium versus specific laser energy

Figure 8 Concentration of hafnium in the extended solid solution of nickel-hafnium versus initial pool mean temperature

Figure 9 Concentration of hafnium in the extended solid solution of nickel-hafnium versus laser-cladding interaction time

Figure 10 Initial pool mean temperature of nickel-hafnium versus laser-cladding interaction time

Figure 11 Variation of the temperature at the solid-liquid interface with the concentration of hafnium in nickel-hafnium alloy

Figure 12 Comparison of nonequilibrium phase diagram of the extended solid solution of nickel-hafnium with its equilibrium phase diagram

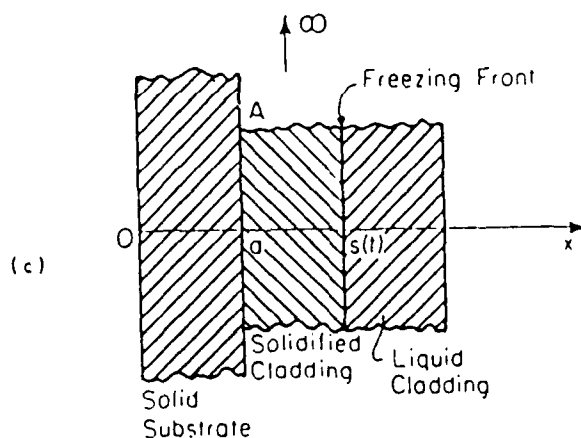
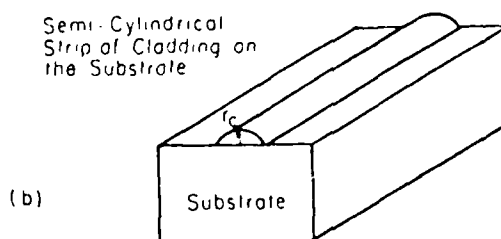
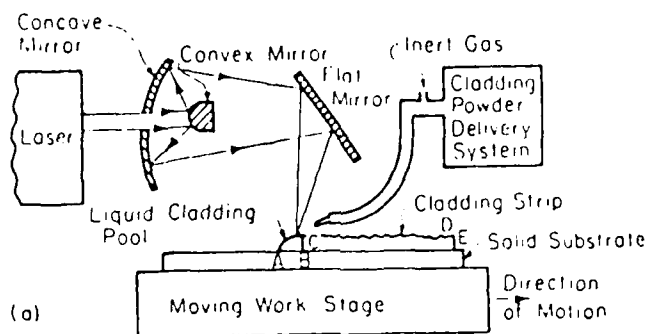


Figure 1(a) Schematic diagram of laser surface cladding
 (b) Three-dimensional view of the cladding and the substrate
 (c) Geometric configuration used in the present model.
 The model substrate and the solidification of the model cladding have been shown after rotating the pool ABCA (see Fig. 1a) by 90° clockwise

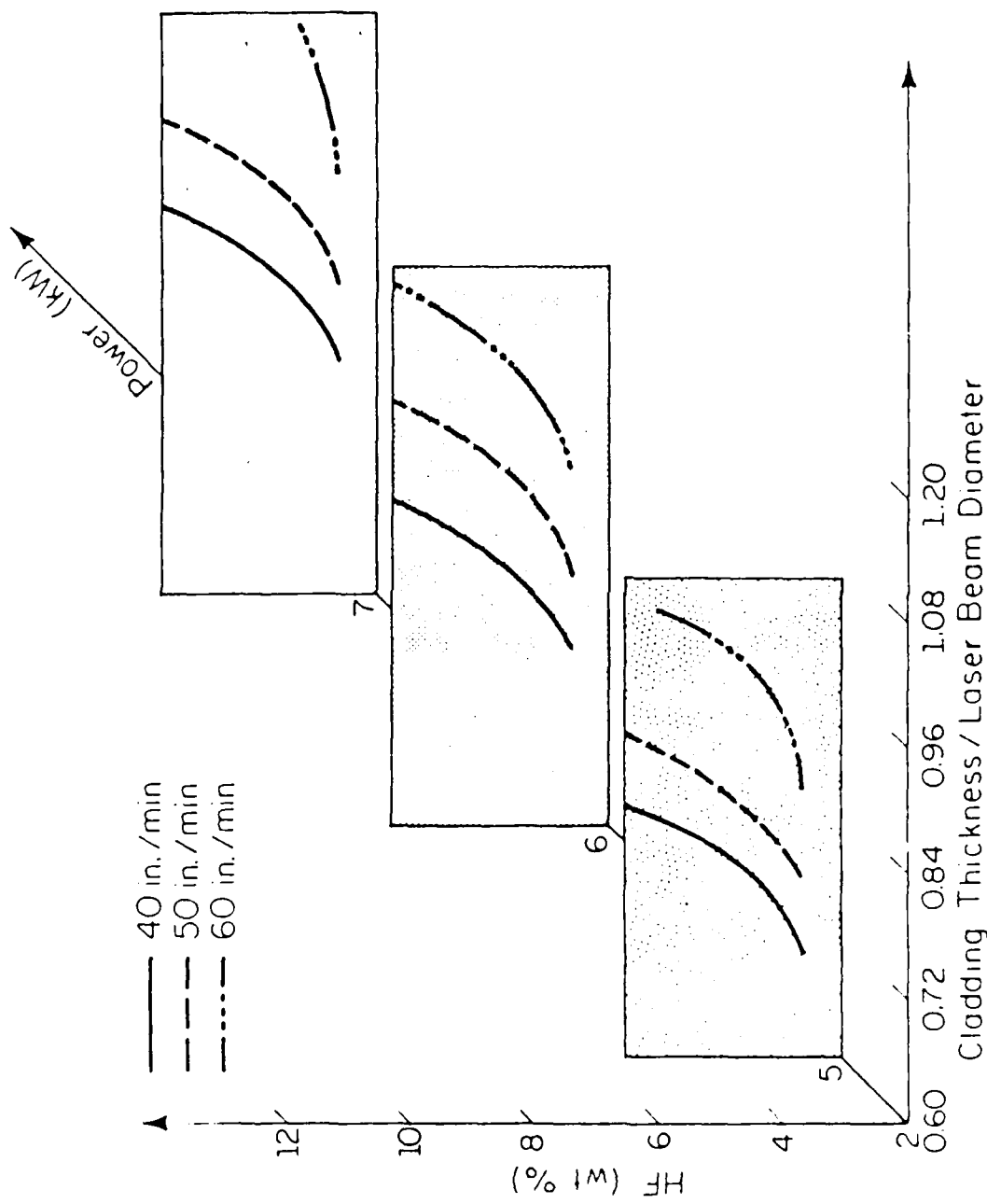


Figure 2 Concentration of hafnium in the extended solid solution of nickel-hafnium versus cladding thickness per unit laser beam diameter

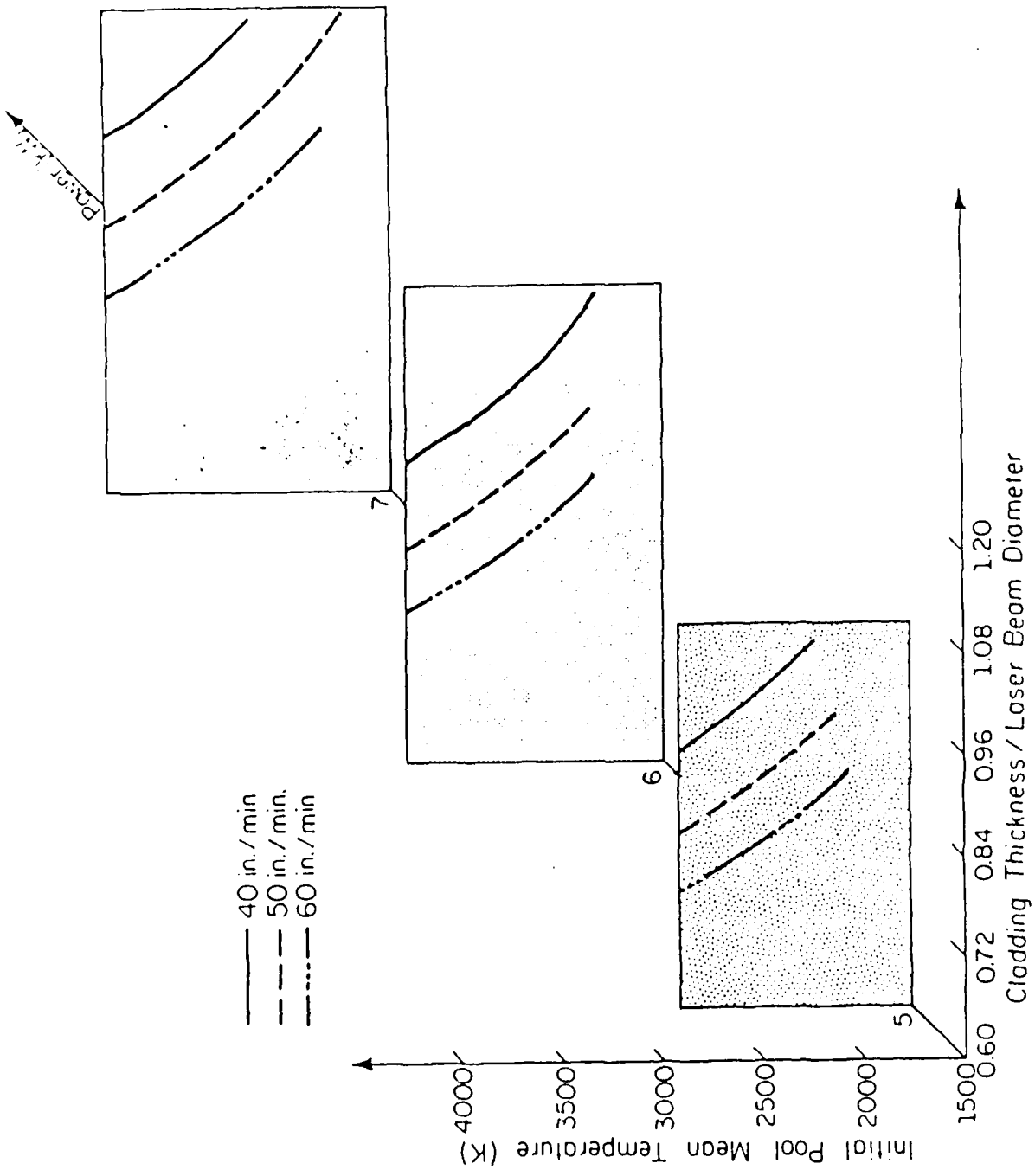


Figure 3 Initial pool mean temperature of nickel-hafnium versus cladding thickness per unit laser beam diameter

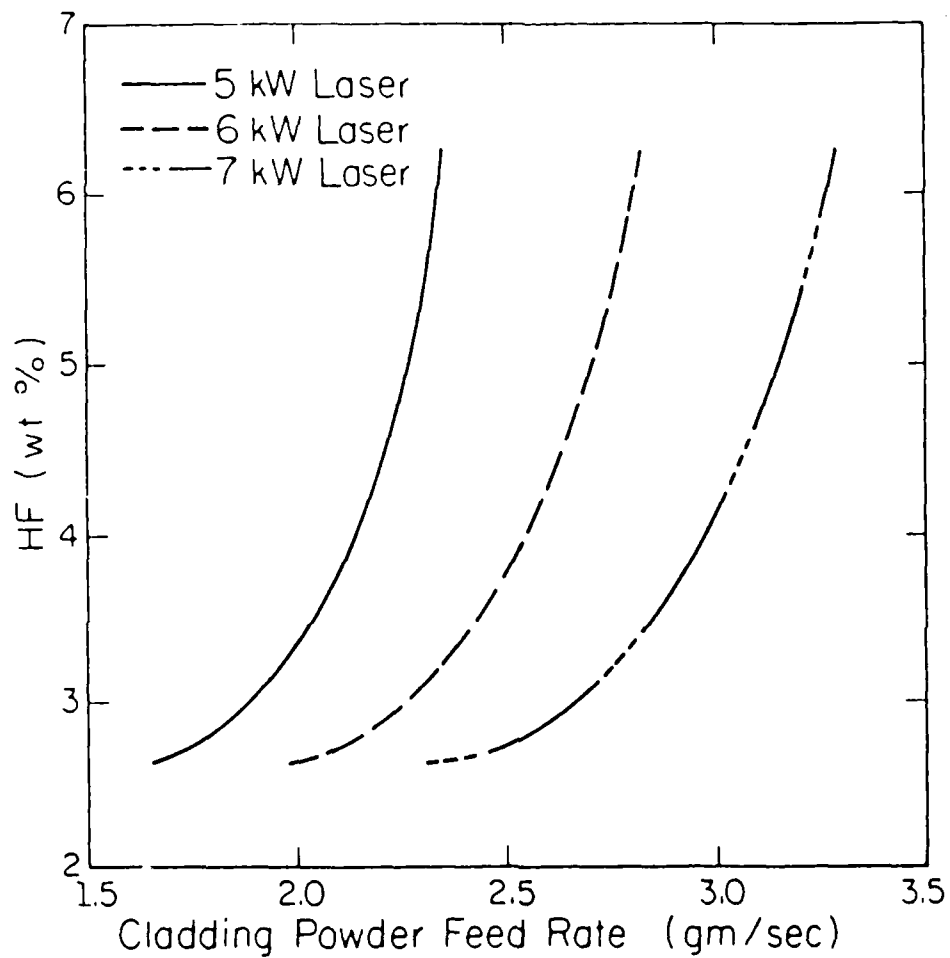


Figure 4 Concentration of hafnium in the extended solid solution of nickel-hafnium versus cladding powder feed rate

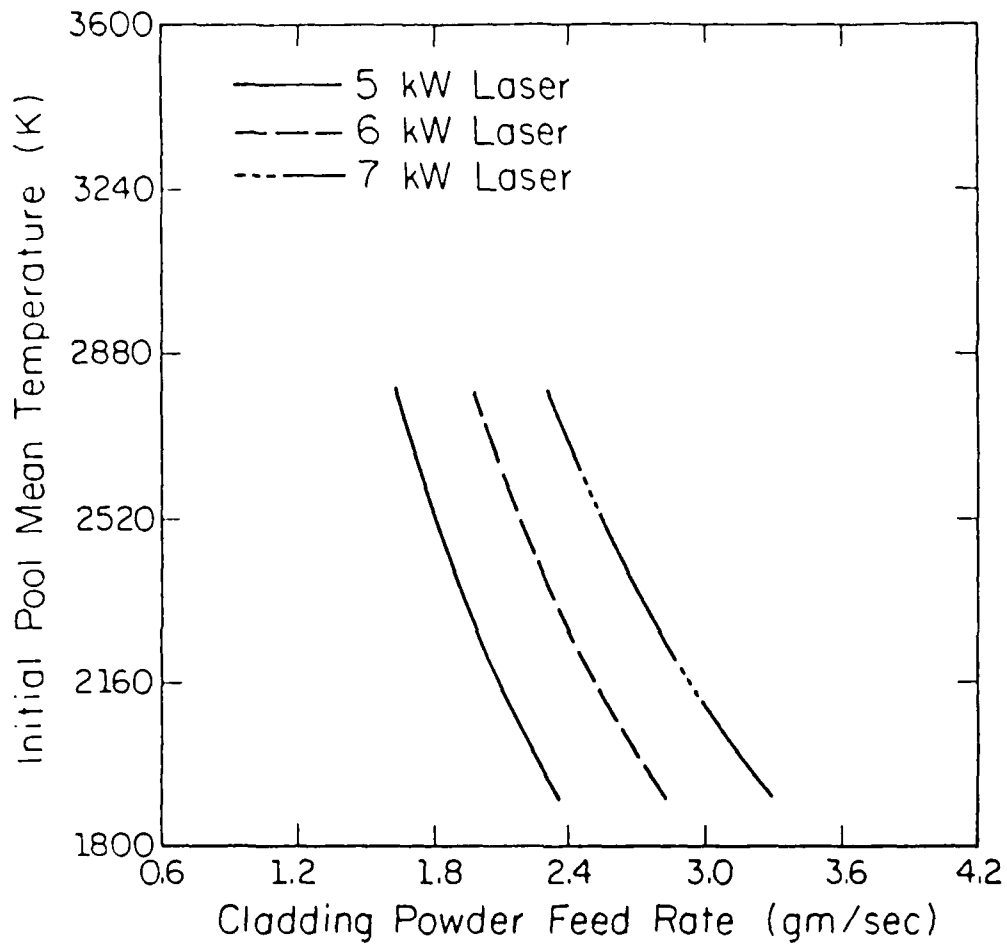


Figure 5 Initial pool mean temperature of nickel-hafnium versus cladding powder feed rate

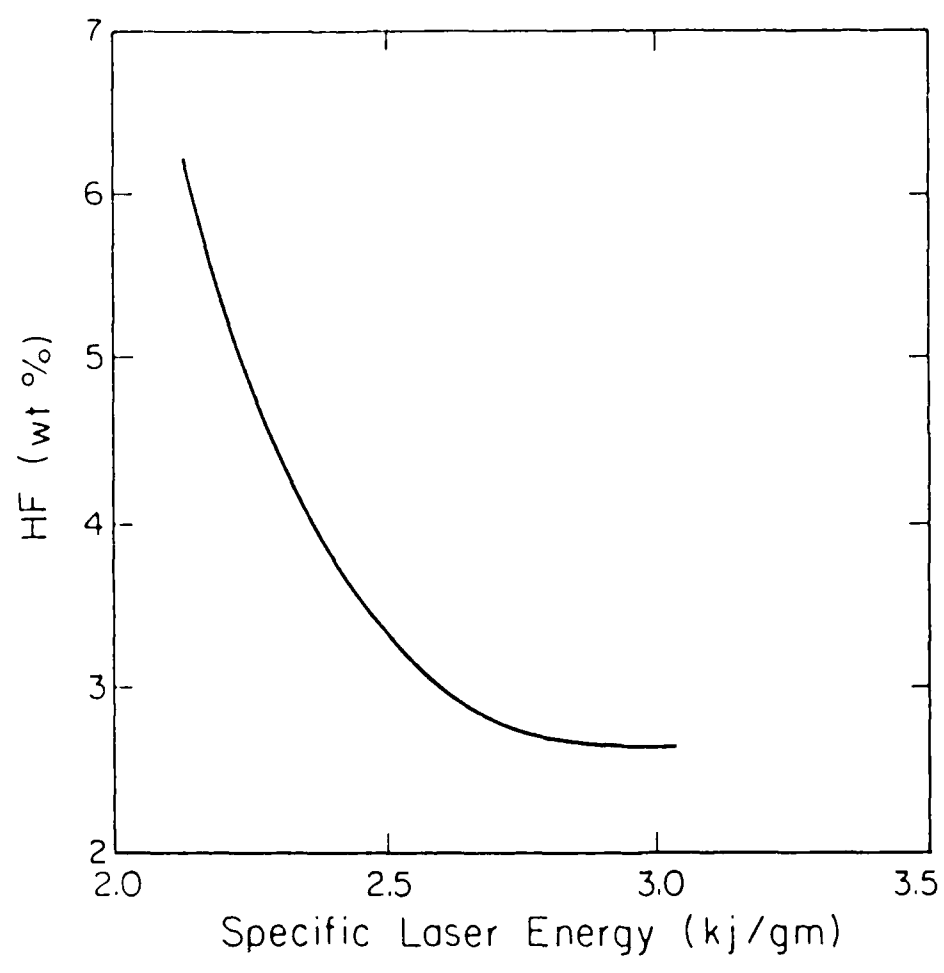


Figure 6 Concentration of hafnium in the extended solid solution of nickel-hafnium versus specific laser energy

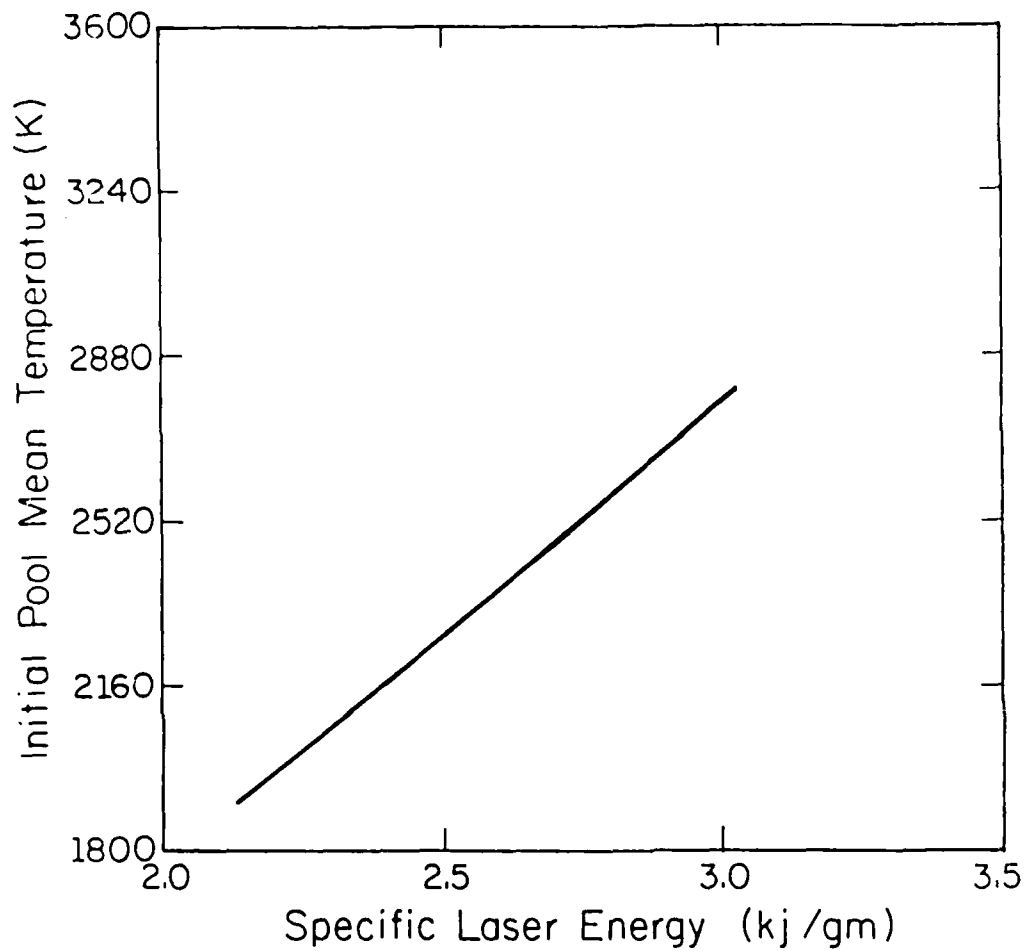


Figure 7 Initial pool mean temperature of nickel-hafnium versus specific laser energy

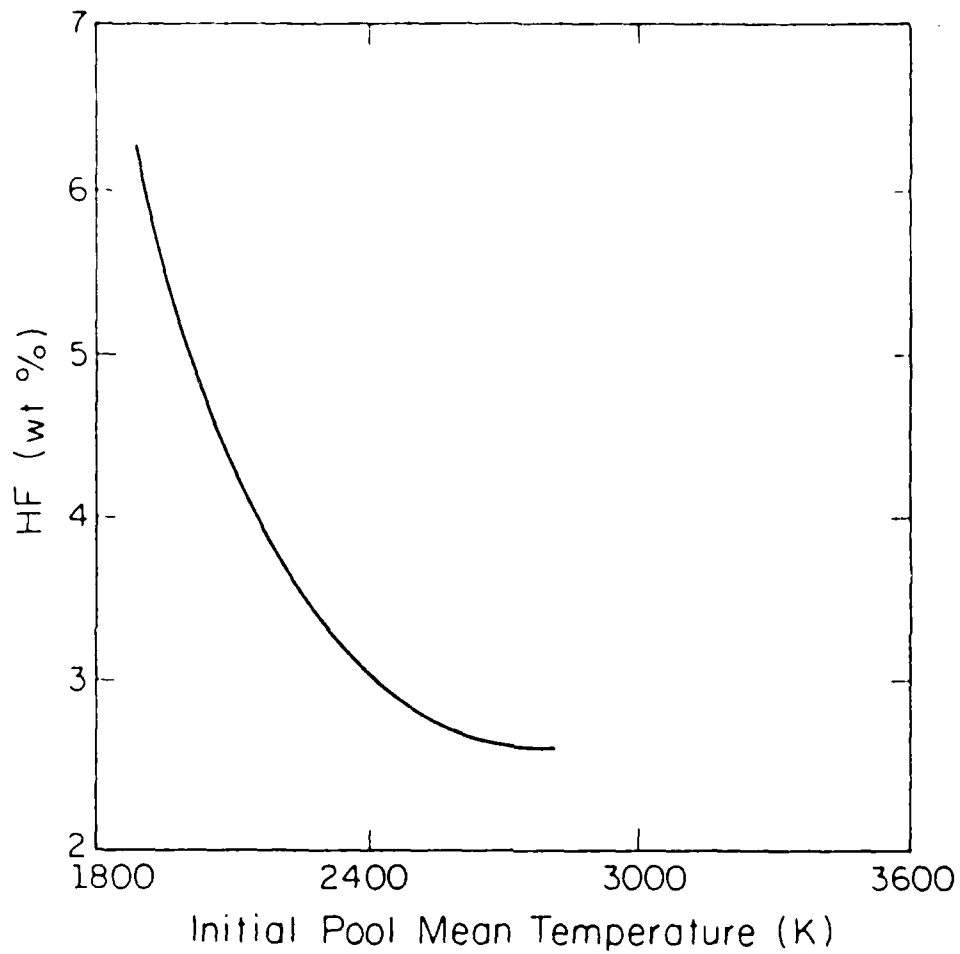


Figure 8 Concentration of hafnium in the extended solid solution of nickel-hafnium versus initial pool mean temperature

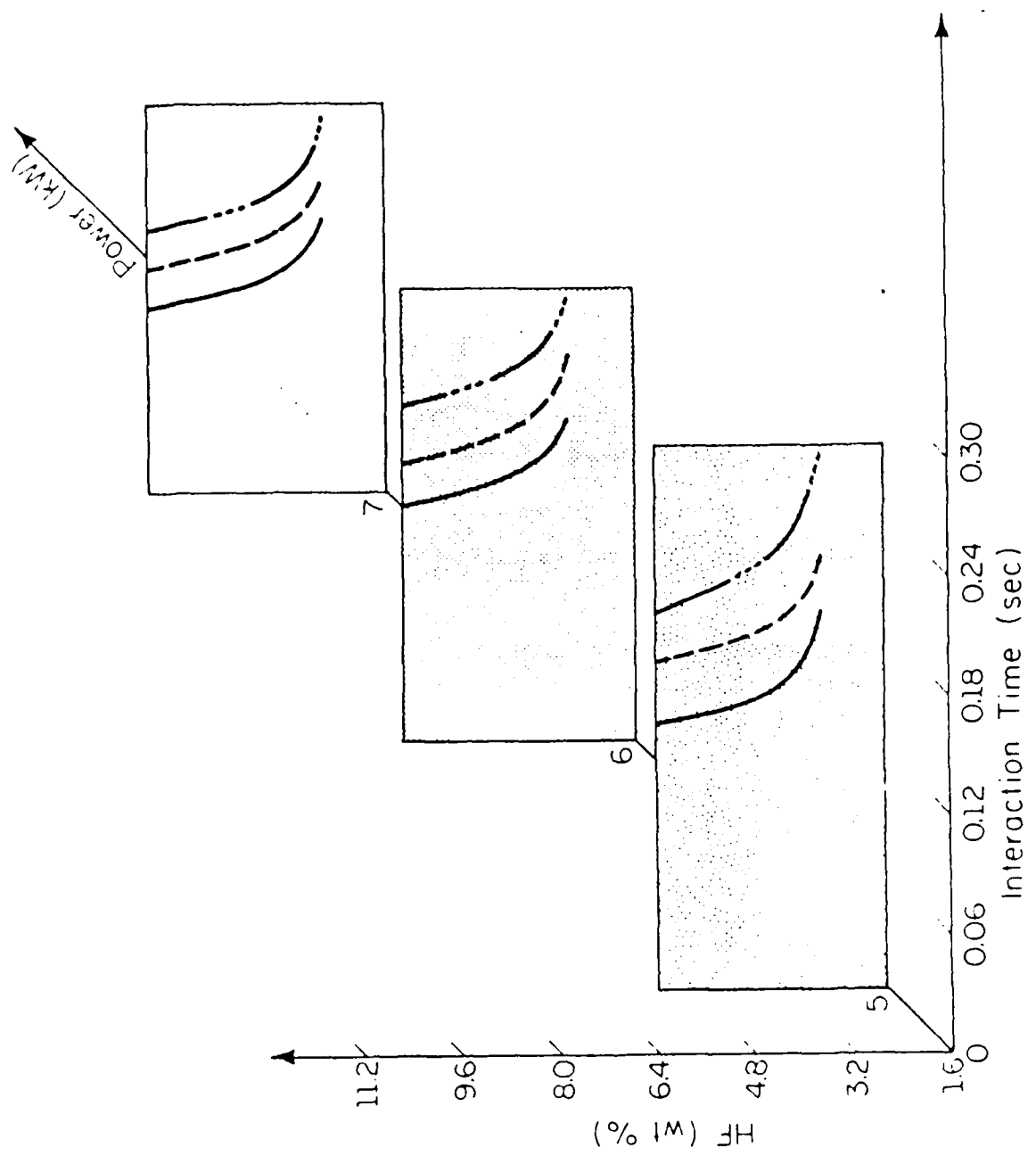


Figure 9 Concentration of hafnium in the extended solid solution of nickel-hafnium versus laser-cladding interaction time

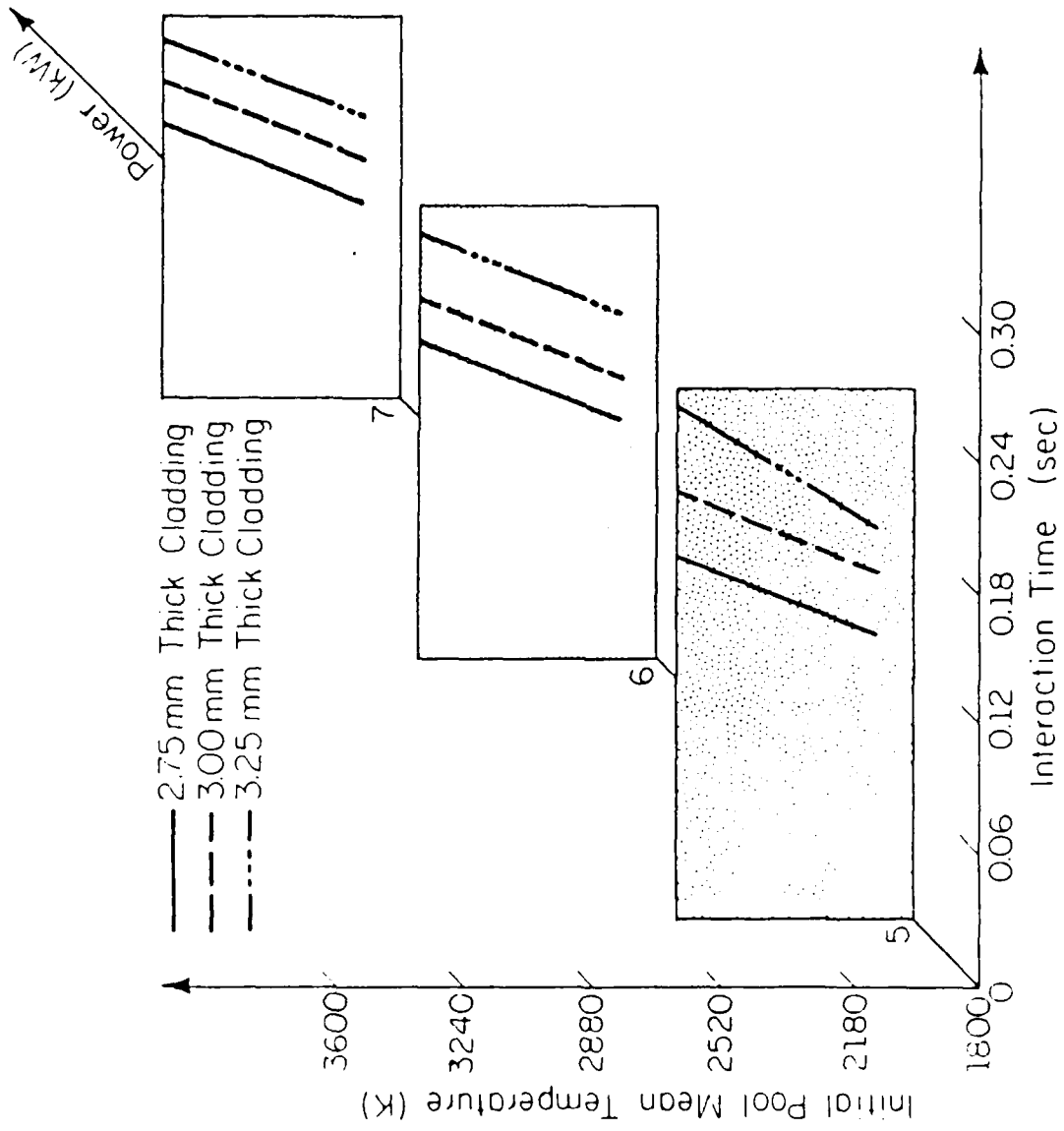


Figure 10 Initial pool mean temperature of nickel-hafnium versus laser-cladding interaction time

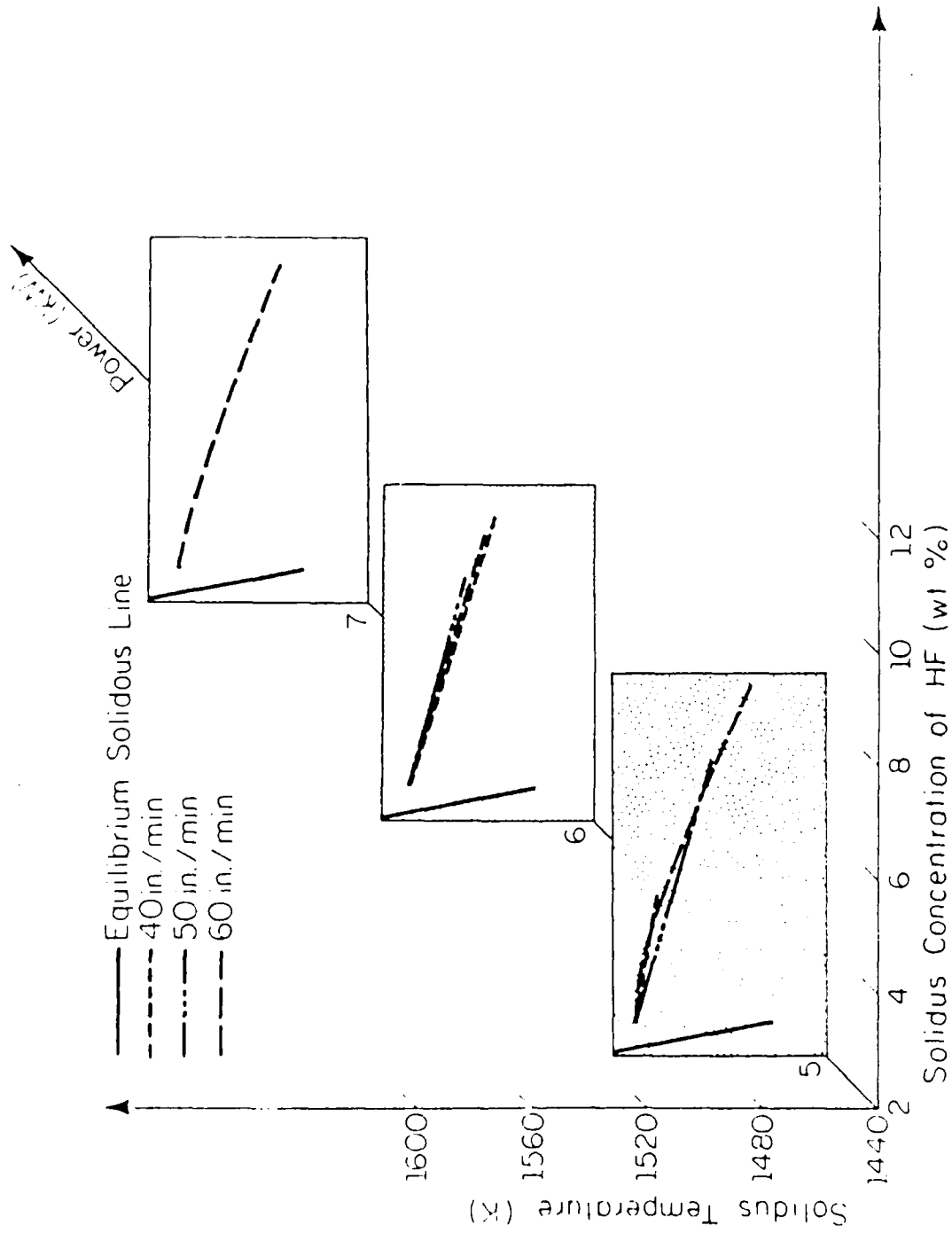


Figure 11 Variation of the temperature at the solid-liquid interface with the concentration of hafnium in nickel-hafnium alloy

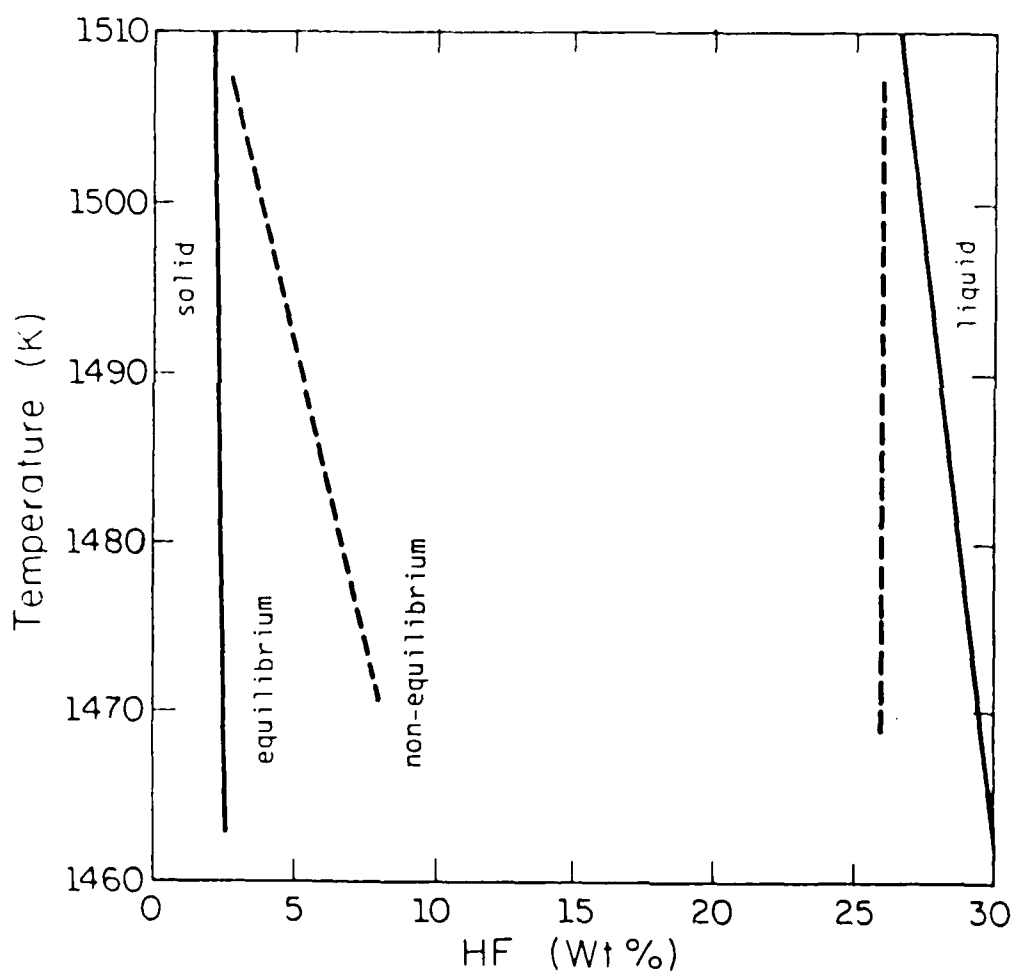


Figure 12 Comparison of nonequilibrium phase diagram of the extended solid solution of nickel-hafnium with its equilibrium phase diagram

APPENDIX B

Submitted to Metallurgical Transaction A

EXTENDED SOLID SOLUTION AND NONEQUILIBRIUM PHASE
DIAGRAM FOR Ni-Al ALLOY FORMED DURING LASER CLADDING

A. Kar and J. Mazumder
Laser Aided Materials Processing Laboratory
Department of Mechanical and Industrial Engineering
University of Illinois at Urbana-Champaign
1206 West Green Street
Urbana, IL 61801

ABSTRACT

Inherent rapid solidification in laser cladding leads to the formation of metastable alloys with extended solid solution. This has been experimentally observed for various binary, ternary and quaternary alloy systems. Composition of the alloys produced by laser cladding process often exceeds the solid solubility limit far beyond that expected from the equilibrium phase diagram. This paper is concerned with the determination of the composition of metastable alloys and the effects of various process parameters on the composition of extended solid solution for Ni-Hf binary alloy system. The cooling process of the molten cladding pool is studied by considering conduction of heat through the pool and the substrate. Both the pool and the substrate are taken to be one-dimensional and finite. Also the freezing point at the solid-liquid interface has been allowed to vary with concentration of the solute. The distribution of solute atoms in the cladding pool is obtained using diffusion theory with nonequilibrium partitioning of solute at the solid-liquid interface.

I. INTRODUCTION

Recent advances in laser technology have drawn considerable interest in using lasers for materials processing and manufacturing. Laser technology not only makes manufacturing processes simpler and more economical but also provides a unique way of modifying the surface chemistry of materials. Due to the inherent rapid heating and cooling rate in laser alloying and cladding processes, it is often possible to obtain novel materials without being restricted by equilibrium phase diagram. The high cooling rate results in extended solid solution to produce metastable alloys. Recently, laser cladding technique has been applied to increase the solid solubility of reactive elements such as Al in nickel superalloy [1] for improved high temperature properties. Thus understanding of basic mechanism of extended solid solution in laser cladding will be useful. The mechanism of extended solubility encompasses the energy, momentum, and mass transport of solute atoms. The heating and cooling rates are determined by the heat transfer equation while the extent of mixing and the redistribution of solute atoms in the molten cladding pool are obtained from the momentum and mass transport equations. This paper uses a mathematical model to predict the composition of solute in the extended solid solution of Ni-Al binary alloy which is usually formed during laser cladding. The model also allows us to construct non-equilibrium phase diagram of a given system from its equilibrium phase diagram.

There is very little information in the available literature on mathematical studies of laser cladding and surface alloying with rapid cooling rate. As mentioned earlier, the composition of a rapidly cooled metastable alloy depends greatly on the heat transfer rate during the solidification process. Three-dimensional heat transfer models for various material pro-

cessings with continuous wave laser were presented by several authors [2-5]. It was found experimentally that surface tension arising due to very high temperature gradient in laser melted pools causes convection. This aspect was modeled by Chan, et al. [6]. They studied the effects of surface tension on the cooling rate, surface velocity, surface temperature, and the pool shape. Chande and Mazumder [7] examined the distribution of solute by diffusion and convection in a laser melted pool after it was delivered to such a pool.

The problem of extended solid solution due to rapid cooling has been studied by various investigators using thermodynamic variables such as free energy and chemical potential. The thermodynamics of nonequilibrium solidification has been examined by Baker and Cahn [8]. Boettinger and Perepezko [9] discussed the process of rapid solidification from the thermodynamics point of view. Boettinger, et al. [10], also used the response function approach of Baker and Cahn [8] and stability analysis for microsegregation-free solidification. Further details on rapidly solidified materials can be found in Refs. [11,12]. In a recent paper [13], the authors have presented a model for extended solid solution during laser cladding by considering the cladding pool and the solid substrate semi-infinite and the freezing point of the cladding melt independent of the concentration of solute. Also, in [14] a mathematical model has been developed and applied to study the Ni-Hf cladding system by considering the width of the substrate and the cladding melt finite and by taking the variation of freezing point of the cladding melt with the concentration of solute into account. The purpose of the present paper is to use this model to study the composition of the extended solid solution of Ni-Al alloy formed during laser cladding and its dependence on various manufacturing parameters. The Ni-Al system differs from the Ni-Hf system in that the slope of the equilibrium phase diagram of the former alloy is positive at

its nominal composition, whereas it is negative for the latter case. We have also obtained nonequilibrium phase diagram for Ni-Al alloy by using this model.

II. MATHEMATICAL MODEL

Process Physics

In laser cladding processes the substrate material which is to be clad is moved at a constant rate while the cladding powder is poured onto it using a pneumatic powder delivery system and melted simultaneously by a laser beam (see Fig. 1a). The uniform speed of the substrate and the constant feed rate of the cladding powder ensure uniform cladding thickness. The molten pool of the cladding material which forms just below the laser beam solidifies by dissipating heat to the surrounding air, adjacent cladding, and the solid substrate as it moves away from the laser beam. The shape of the cladding melt pool and the solidified cladding on the substrate is influenced by laser power, laser beam diameter, thermo-physical properties of the cladding powder and the substrate, temperature of the substrate, relative motion between the cladding powder delivery system and the substrate, the cladding powder feed rate and the interaction time between the cladding and the laser beam. In the present model the strip of cladding BCDEB (see Fig. 1a) is assumed to be semi-cylindrical in shape (see Fig. 1b) and based on this the initial pool mean temperature is determined (see Eq. (5)). The liquid cladding pool and the substrate were taken to have finite thickness in the positive direction of the x-axis and they are considered infinitely large in the other two directions (see Fig. 1c).

The molten pool of the liquid cladding solidifies by conducting away heat through the substrate and the solid cladding across AB and BC, respectively. Also, it loses some energy to the ambient inert gas across the free surface CA. The cladding BCDEB is formed from the liquid cladding melt just solidified and hence its temperature distribution is almost uniform and equal to the temperature of the molten pool ABCA. So the heat loss across BC would be very

little. Therefore, we can consider that the pool of cladding melt (ABCA) loses energy through the surfaces at AB and CA. To carry out one-dimensional heat transfer calculations we assume that the pool extends up to infinity along AB. Due to this assumption the cladding melt solidifies along AB and this freezing front moves upward in the direction of BC. The solid substrate has been considered to have finite width, but it is infinitely large along AB. The geometric configuration of this pool has been shown in Fig. 1c by rotating the pool 90 degrees in the clockwise direction. In this figure the freezing front has been shown to be planar. This is true when a pure metal solidifies. For a cladding melt of an alloy system, the freezing front develops curvature due to surface tension. Also there could be dendrite and cellular growth at the solid-liquid interface. Moreover, rapid cooling may lead to nucleation in the bulk of the liquid phase. The stability criterion of Mullins and Sekerka [15] of a planar interface during solidification of a dilute binary alloy shows that the planar interface will be unstable for the nickel-aluminum system considered in this study. It was found [13] that there are dendrites which are very small in size. Nevertheless, the dendrites will affect the diffusion of solute atoms at the freezing front. However, to simplify the mass transfer analysis, the freezing front has been assumed to be planar due to the small size of dendrites. Moreover, the trend predicted by the model is more important than the exact numerical values due to the paucity of high temperature materials data and simplifying assumptions. Besides this the model used in this study is based on a few more assumptions listed below.

- (1) The thermal conductivity and the thermal diffusivity for a mixture is the sum of the volume-averaged value of the respective transport properties of each element of the mixture,

- (2) The mass diffusivity of each element in the liquid phase is the average value of self-diffusivity over the room temperature and the initial temperature with modified activation energy for the mixture,
- (3) The cladding pool and the substrate are in thermally perfect contact,
- (4) There is no mass diffusion in the solid phase,
- (5) The solute segregated at the solid-liquid interface moves into the liquid phase by diffusion only. This is because a boundary layer is formed near the interface where diffusion of solute atoms is dominant,
- (6) The cladding melt forms a uniform solution of composition equal to that of the cladding powder mixture before its solidification begins,
- (7) Only 50 percent of the laser energy is absorbed by the cladding material. Studies [12] show that the amount of laser energy absorbed by different materials is 37 to 60 percent.

With these assumptions, the one-dimensional heat conduction equations for the substrate, solidified cladding, and the liquid cladding regions are solved. The solutions of these heat transfer equations are used to obtain the velocity of the solid-liquid interface and then the mass transfer equation is solved to determine the distribution of solute atoms in the liquid phase. From this, the concentration of the solute atoms in the solid phase is computed by using an expression for nonequilibrium partition coefficient for dilute solution developed by Aziz [16].

Mathematical Formulations

In this section the governing heat conduction equations for energy transport in the substrate, solidified cladding, liquid cladding regions, and the mass transfer equation for diffusion of solute atoms in the liquid cladding pool are presented along with boundary and initial conditions. The problem is

solved by using a variable eigenvalue approach [17] for moving boundary problems. Özisik and Gruceri [18] followed a similar approach to obtain a solution to the phase change problem. Also Yener and Özisik [19] used the method of variable eigenvalues to solve for temperature distribution in multi-region finite media with time-varying heat transfer coefficient.

The governing equations for energy transport are

(i) Solid substrate region

$$\frac{\partial^2 T'_1}{\partial x^2} = \alpha_1 \frac{\partial T'_1}{\partial t}; \quad t \geq 0, \quad 0 \leq x \leq a; \quad (1)$$

(ii) Solidified cladding region

$$\frac{\partial^2 T'_2}{\partial x^2} = \alpha_2 \frac{\partial T'_2}{\partial t}; \quad t \geq 0, \quad 0 \leq x \leq S(t); \quad (2)$$

(iii) Liquid cladding region

$$\frac{\partial^2 T'_3}{\partial x^2} = \alpha_3 \frac{\partial T'_3}{\partial t}; \quad t \geq 0, \quad s(t) \leq x \leq b. \quad (3)$$

The auxiliary conditions are

$$k_1 \frac{\partial T'_1}{\partial x} = h_1 (T'_1 - T_r) \quad \text{at } x = 0 \text{ and } t \geq 0, \quad (4a)$$

$$T'_1(a, t) = T'_2(a, t), \quad (4b)$$

$$k_1 \frac{\partial T'_1}{\partial x} = k_2 \frac{\partial T'_2}{\partial x} \quad \text{at } x = a \text{ and } t \geq 0, \quad (4c)$$

$$T_2'(s(t), t) = T_3'(s(t), t) = T_I(C_p, \dot{s}(t)), \quad (4d)$$

$$-k_3 \frac{\partial T_3'}{\partial x} = h_3(T_3' - T_r) \text{ at } x = b \text{ and } t \geq 0, \quad (4e)$$

$$k_2 \frac{\partial T_2'}{\partial x} - k_3 \frac{\partial T_3'}{\partial x} = \rho L \frac{ds}{dt} \text{ at } x = s(t) \text{ and } t \geq 0, \quad (4f)$$

and

$$s(0) = a. \quad (4g)$$

The initial conditions for the above problems are obtained from the following considerations.

The cladding is assumed to melt almost instantaneously as soon as it is exposed to the laser beam to reach a uniform temperature \bar{T}_2 . \bar{T}_2 is calculated by taking a lumped-parameter energy balance of the laser energy imparted to the cladding and the energy required to melt the cladding powder and raise its temperature to T_2 . This yields the following expression for \bar{T}_2 :

$$\bar{T}_2 = T_r + \frac{1}{C_p} \left[\frac{2pf}{\pi r_c^2 v_0} - L \right]. \quad (5)$$

This expression is derived by considering the cladding to be formed in the shape of a semi-cylindrical strip (see Fig. 1b). To obtain the initial condition for the solid substrate, a linear temperature profile is constructed between the temperature \bar{T}_2 at $x = a$ and T_r at $x = 0$. Thus the initial conditions are

$$T_1'(x, 0) = (\bar{T}_2 - T_r) \frac{x}{a} + T_r \quad (6a)$$

and

$$T_3'(x,0) = \bar{T}_2. \quad (6b)$$

The procedure to solve this problem has been described in details in Ref. [14]. We will present only the final results in this paper. The temperature field is given by

$$T_i(x,t) = \sum_{n=1}^{\infty} \frac{1}{N_n} \bar{T}_n(t) K_{i,n}(x,t) \quad (7)$$

where the normalizing constant N_n is evaluated from

$$N_n = \sum_{i=1}^3 \int_{a_i}^{b_i} w_i \{K_{i,n}(x,t)\}^2 dx. \quad (8)$$

Here, $w_i = k_i/\alpha_i$ and

$$K_i(x,t) = E_i \sin\left(\frac{\lambda(t)x}{\sqrt{\alpha_i}}\right) + F_i \cos\left(\frac{\lambda(t)x}{\sqrt{\alpha_i}}\right). \quad (9)$$

The method of determining E_i 's, F_i 's and $\lambda(t)$'s will be discussed below. In Eq. (7) $\bar{T}_n(t)$ is obtained by solving the following set of first-order non-linear ordinary differential equations:

$$\begin{aligned} \frac{d}{dt} \bar{T}_n(t) + \lambda_n^2 \bar{T}_n(t) &= \sum_{i=1}^3 \int_{a_i}^{b_i} k_i T_i \frac{\partial K_{i,n}}{\partial t} dx \\ &- \int_{s(t)}^b k_3 K_{3,n}(x,t) \frac{1}{\alpha_3} \left(R \frac{x^2}{2} + Ax + B - \alpha_3 R \right) dx \end{aligned} \quad (10)$$

for $n = 1, 2, \dots, \infty$, and the initial conditions

$$\bar{T}_n(0) = \sum_{i=1}^3 \int_{a_i}^{b_i} w_i T_i(x,0) K_{i,n}(x,0) dx.$$

where

$$R(t) = \frac{\rho L}{k_3} \left(\frac{\dot{s}}{b-s} \right) \left(\frac{1 + 2\tau_1}{1 + \tau_1} \right), \quad A(t) = -Rs - \frac{\rho L \dot{s}}{k_3}$$

$$B(t) = -R \frac{s^2}{2} - As, \quad \text{and} \quad \tau_1 = \frac{h_3}{2k_3} (b-s).$$

The eigenvalues $\lambda(t)$'s are obtained from the following equation:

$$\det M = 0$$

where $\det M$ represents the determinant of a 6×6 matrix M . The elements of this matrix M_{jk} for $j = 1, 2, \dots, 6$ and $k = 1, 2, \dots, 6$ have been given in the Appendix. The constants of integration E_i and F_i 's are obtained from a set of algebraic equations given by

$$[G] [H] = [N]$$

where $[G]$ is a 4×4 matrix, $[H]$ and $[N]$ are column vectors of four elements each. These elements have been defined in the Appendix. To obtain the four algebraic equations given by the above matrix equation, F_1 has been set equal to unity and this implies

$$E_1 = \frac{h_1 \sqrt{a_1}}{\lambda k_1}$$

When the eigenvalues and the constants of integration E_i and F_i 's are determined, the kernel of integral transform $K_{i,n}(x,t)$ is completely known. $K_{i,n}(x,t)$ can be substituted into the Eq. (10) and then the resulting set of first-order ordinary nonlinear differential equations can be solved using the Runge-Kutta method. These equations are to be solved in conjunction with the equations for mass transfer since they are coupled by the condition at the solid-liquid interface given by

$$T_I - T_r = T_3(s(t), t) = \sum_{n=1}^{\infty} \frac{1}{N_n} \bar{T}_n(t) [E_3 \sin(\lambda_n s / \sqrt{\alpha_3}) + F_3 \cos(\lambda_n s / \sqrt{\alpha_3})] \quad (11)$$

This equation is solved to determine the location of the freezing front $s(t)$. In this equation the interface temperature T_I depends on concentration. The following expression for T_I as derived by Boettinger and Perepezko [9] has been used in this model

$$T_I = T_m^* + m_l C_l^* + \frac{m_l C_l^*}{1 - k_e} (k_e - k^* (1 - \ln \frac{k^*}{k_e})) + \frac{m_l}{1 - k_e} \frac{\dot{s}(t)}{v_0} \quad (12)$$

Here v_0 represents the velocity of sound in the liquid phase. The velocity of sound in a medium depends on its temperature and composition. In this study v_0 has been taken to be equal to the velocity of sound in the pure solvent. T_m^* and m_l are determined from the equilibrium phase diagram by taking a segment of the liquidus around the point of interest. This segment is considered linear whose slope and intercept with the temperature axis are m_l and T_m^* respectively. C_l^* is obtained by evaluating $C(x,t)$ at $x = s(t)$ and by expressing it in terms of mole fraction.

The concentration dependence of T_I couples the energy equations (10) with the mass transfer equation and hence they must be solved simultaneously. The

diffusion of solute atoms in the cladding melt pool is governed by the following mass transfer equation

$$\frac{\partial^2 C}{\partial x^2} = \frac{1}{D} \frac{\partial C}{\partial t} \quad (13)$$

subject to the following initial and boundary conditions

$$C(x,0) = C_0, \quad (14a)$$

$$-D \frac{\partial C}{\partial x} = 0 \text{ at } x = b, \quad (14b)$$

and

$$-D \frac{\partial C}{\partial x} = \dot{s}(t) [k^*(t) - 1] C(x,t) \text{ at } x = s(t). \quad (14c)$$

Here again the above partial differential equation (13) can be reduced to the following set of coupled and nonlinear first-order ordinary differential equations by using integral transform technique [14].

$$\frac{d\bar{C}_n(t)}{dt} + \bar{D}_n^2(t)\bar{C}_n(t) = H_{m,n}(t) - \phi_n(s(t),t) \dot{s}(t) \sum_{m=0}^{\infty} \frac{1}{N_m} \bar{C}_m(t) \phi_m(s(t),t)$$

$$\text{for } n = 1, 2, 3, \dots, \infty, \text{ and} \quad (15)$$

subject to the initial conditions

$$\bar{C}_n(0) = \int_a^b dx C_0 \cos(\mu(x-b))$$

where

$$H_{m,n}(t) = -\sum_{m=0}^{\infty} \frac{\bar{C}_m(t)}{N_m} \int_{s(t)}^b dx \phi_m(x,t) \sin(u_n(x-b)) \dot{u}_n(t)(x-b)$$

$$\bar{C}_n(t) = \int_{s(t)}^b dx \phi_n(x,t) C(x,t). \quad (16)$$

$$\phi(x,t) = \cos(u(t)(b-x))$$

and the eigenvalues $u(t)$'s are given by the following transcendental equation

$$u \{ u \sin(u(b-s)) - \frac{\dot{s}(k^*-1)}{\bar{D}} \cos(u(b-s)) \} = 0.$$

Finally, the concentration is given by

$$C(x,t) = \sum_{n=0}^{\infty} \frac{1}{N_n} \bar{C}_n(t) \phi_n(x,t) \quad (17)$$

with the normalizing constant obtained from

$$N_n = \int_{s(t)}^b \phi_n^2(x,t) dx.$$

The partition coefficient, normally defined as the ratio of the concentration of solute in the solid phase to that in the liquid phase at the solid-liquid interface is constant for equilibrium solidification. When solidification progresses rapidly, it is no longer constant. For rapid cooling rate, an expression for the partition coefficient $k^*(t)$ has been derived by Aziz [16] which is

$$k^*(t) = \frac{C_s}{C_l} = \frac{\beta + k_e}{\beta + 1} \quad (18)$$

where $\beta = \dot{s}(t)\lambda/D^*$. In the present model the interdiffusivity D^* is taken to be equal to the mass diffusivity \bar{D} and the interatomic distance λ is taken to be 4\AA , which is the average diameter of an atom. To use the expression (18) for determining the concentration of solute in the solid phase at the solid-liquid interface, we have to know $\dot{s}(t)$ and C_2 . For this, Eq. (11) and its time-derivative are solved for $s(t)$ and $\dot{s}(t)$ respectively. Similarly, C_2 is obtained from Eq. (17) by evaluating $C(x,t)$ at $x = s(t)$.

III. RESULTS AND DISCUSSION

Experimental Verification

The results of the above model were compared with experimental data. Two cladding samples were prepared on nickel substrate with a mixture of Ni-Al powder of nominal composition, 74% Ni and 26% Al by weight by using two different laser powers 5 kw and 6 kw. The laser beam diameter and the laser scanning speed were respectively, 3 mm, and 21.17 mm/sec. for both samples. The cladding takes the shape of an approximately semi-cylindrical strip of metal on the substrate (see Fig. 1b). Scanning Electron Microscope (SEM) data of the cladding samples show the concentration of Al in the matrix of Ni in excess of that predicted by the equilibrium phase diagram. These data show about 29 wt.% Al in the martensitic Ni-Al solid solution regions. The theoretical results predicted by this model is 30.76 wt.% Al in the Ni-Al alloy. There is a little discrepancy between the theoretical and experimental results which may be due to some of the assumptions of this model. For example, the present model utilizes an expression, Eq. (18), for the nonequilibrium partition coefficient which is applicable to dilute solution. Apart from this condition, the presence of a two-phase zone between the solidus and the liquidus lines and the surface tension driven flow causing convection in the liquid pool will affect the mixing of solute in the liquid phase and thus alter its composition in the solid phase. Paucity of high temperature liquid metal data also contributes to the numerical error. However, the objective of this study is to determine the trend of, and thus understand, the underlying process physics. The trend predicted agrees with what is observed experimentally.

Parametric Results

The above model was used to study the effect of various important process parameters such as laser power, laser-cladding interaction time, cladding thickness, cladding powder delivery rate on the composition of aluminum in nickel matrix. Results were obtained for ambient temperature $T_r = 293^\circ\text{K}$ and the heat transfer coefficients $h_1 = 1 \text{ Watt/cm}^2\text{-}^\circ\text{K}$ and $h_2 = 0.01 \text{ Watt/cm}^2\text{-}^\circ\text{K}$. Only convective heat loss from the cladding and the substrate to the ambient inert gas has been considered in this model because the heat loss due to conduction is usually very small and the radiative loss is usually about 5 percent (see Ref. [2]) of the total energy of the melt pool. The convection heat transfer coefficients are usually 25 to 250 $\text{watt/m}^2\text{-K}$ and 50 to $2 \times 10^4 \text{ watt/m}^2\text{-}^\circ\text{K}$ for the processes of forced convection by gases and liquids, respectively (see Ref. [20]). The heat conduction within the cladding melt is mainly unidirectional for reasons mentioned earlier and its heat loss to the ambient gas has been taken to be due to forced convection by the surrounding inert gas. For this reason, the above value of h_2 has been selected. The heat conduction within the substrate has been considered to be unidirectional even though there would be conduction in the other two directions. Consequently, the heat loss due to conduction in these two directions has not been accounted for in the one-dimensional model. This is why a rather high convective heat loss from the substrate has been considered by choosing the above value of h_1 . The laser power was fixed at 5, 6, and 7 kW. For each power of laser, the speed of the workpiece was varied as 40, 50, and 60 inches/min. Since the transport properties depend on temperature, average values, which are calculated according to formulas of Ref. [13], were used in this model.

Results obtained from this study have been presented in Figs. 2 through 12. Figure 2 shows the concentration of aluminum (in wt. %) in a nickel

matrix for different values of laser power and cladding thickness measured in units of laser beam diameter. The laser beam diameter used in this study is 3 mm. As can be seen from this figure, the concentration of aluminum decreases as cladding thickness increases for a given speed of the workpiece and laser power. This is due to the fact that the initial pool mean temperature, \bar{T}_2 , varies inversely with the cladding thickness as evident from Eq. (5) as well as Fig. 2. Therefore, an increase in the cladding thickness will result in decrease of the initial pool mean temperature. The effect of decrease in temperature (\bar{T}_2) on the concentration of aluminum in nickel matrix can be studied by observing that the slope of the equilibrium phase diagram of Ni-Al alloy is positive at the nominal composition of the cladding powder. This means that decrease in temperature (\bar{T}_2) or correspondingly increase in cladding thickness will cause reduction in the concentration of aluminum in the Ni-Al solid solution. This is why we find in Fig. 2 that the concentration of aluminum decreases as cladding thickness increases. On the contrary, the slope of the equilibrium phase diagram of Ni-Hf alloy is negative. Due to this, decrease in \bar{T}_2 or correspondingly increase in cladding thickness in Ni-Hf system causes rise in the concentration of Hf in Ni matrix [14] as opposed to Ni-Al system.

Figure 3 shows the variation of initial pool mean temperature with respect to the cladding thickness per unit laser beam diameter for different values of laser power. Figures 4 and 5 are concerned with the variation of initial pool mean temperature and the solute concentration in the solid phase with the cladding powder feed rate, respectively. The cladding powder feed rate is determined by using the expression $\frac{1}{2} \pi r_c^2 v_c$ which is obtained by assuming that the cladding takes the shape of a semi-cylindrical strip (see Fig. 1b). Cladding powder feed rate is a very important process parameter

since it is related to cladding thickness and velocity of the workpiece as well as the initial pool mean temperature. Thus if the powder delivery rate is known, then \bar{T}_2 can be obtained from the Fig. 4 and the concentration of solute can be obtained from the Fig. 5 and then the velocity of the workpiece can be selected for a desired cladding thickness. It can be seen in Fig. 4 that the initial pool mean temperature decreases as the cladding powder feed rate increases. This is because when the powder feed rate is increased keeping all other process parameters unchanged, more material is melted and heated up by the same amount of laser energy. The inverse relation between \bar{T}_2 and the cladding powder feed rate leads to the formation of Ni-Al alloy with aluminum decreasing with the increase in powder feed rate as shown in Fig. 5. The reason for this has been given above while discussing the results of Fig. 2. Figures 6 and 7 indicate the effect of specific laser energy on solute concentration in the solid phase and on the initial pool mean temperature. Specific laser energy is defined as laser energy required to produce a cladding of unit mass. It is determined by the relation $P/(\frac{1}{2}\pi r_c^2 v_0)$. The importance of selecting specific laser energy as a parameter is that it allows representation of the solute concentration data for any combination of laser power, workpiece speed, and cladding thickness parameters by a single graph. This is because the initial pool mean temperature is proportional to specific laser energy. Thus the initial pool mean temperature and hence the thermal characteristic of the cladding melt pool will not be different as long as the laser specific energy remains the same for any choice of the process parameters. The effect of initial pool mean temperature on the solute concentration in the solid phase is shown in Fig. 8. It can be seen from this figure that the the concentration decreases with an increase in temperature for reasons explained above.

The effect of another important process parameter, laser-materials interaction time, on the solute concentration and the initial pool mean temperature is shown in Figs. 9 and 10 for different values of laser power. Interaction time is defined as the ratio of laser beam diameter to the speed of the work-piece. It can be observed that the trends of the graphs with respect to laser-material interaction time are opposite to those observed with respect to cladding thickness. This is because thin cladding leads to higher initial pool mean temperature than what is obtained as interaction time decreases provided other process parameters are kept unchanged. We have also seen that the solute concentration in the solid phase is higher at a higher initial pool mean temperature. This explains why the solute concentration curves with respect to the interaction time should be opposite to those which are plotted with respect to the cladding thickness.

Finally, the solidus temperature versus the solidus concentration of Al has been plotted in Fig. 11 different laser powers. It is natural to expect that for a given solidus temperature, there should be a unique value of the solidus concentration of solute irrespective of how the process parameters are selected. This emphasizes the fact that the temperature versus concentration curves obtained for different process parameters must overlap. As can be seen from the Fig. 11, these curves indeed overlap. The Fig. 12 shows the non-equilibrium phase diagram computed by using this model. The characteristic parameters for this figure have been presented in Table 1. The deviation of nonequilibrium phase diagram from the equilibrium one shows the extension of solid solubility that can be obtained during laser cladding. The non-equilibrium phase diagram has been plotted in the neighborhood of the melting point of the cladding powder because the value of k_e used in the expression for nonequilibrium partition coefficient (Eq. (18)) corresponds to this

melting point. It can be seen from the Fig. 12 that the width of the solid-liquid region between the equilibrium solidus and liquidus has increased considerably. The nonequilibrium solidus line of this figure shows the extension of Al concentration in Ni that can be obtained due to the rapid cooling in laser cladding. This phenomenon can be understood from the fact that the equilibrium phase diagram of Ni-Al has a positive slope at the point which corresponds to the nominal composition of the cladding powder. Due to this, Al is retained in the Ni matrix whereas Nickel is rejected into the liquid phase as solidification proceeds. This causes an extension of Al concentration in the solid phase and lowers its weight fraction in the liquid phase and thus enlarges the solid-liquid region between the solidus and the liquidus lines. However, the equilibrium phase diagram of Ni-Hf alloy has a negative slope at the nominal composition of the cladding powder. As a result, Hf is rejected from the Ni matrix when the solution of Ni-Hf solidifies. This causes an increase of the concentration of Hf in the liquid phase. But since the solid phase retains more Hf than its equilibrium composition, the liquid phase will have less Hf than the equilibrium value and hence the extended solid solution (that is, the nonequilibrium) phase diagram will shrink [14] as opposed to Ni-Al alloy system.

Table 1 Solidus Composition of Al, Solidus/Liquidus Temperature at the Substrate-cladding Interface and the Speed of Solidification at this Interface

Composition of Al (wt%)	Solidus/Liquidus Temperature (K)	Interface Speed (cm/sec)
30.83	1864	6.1
30.74	1863	5.6
30.56	1862	4.5

IV. CONCLUSION

The present work examines the extension of solid solubility based on the transport of energy and mass. Solute transport has been considered to take place only in the liquid phase while the energy transport has been considered in both solid and liquid phases. The effect of nonequilibrium cooling rate on solute segregation at the freezing front has been taken into account by considering a nonequilibrium partition coefficient. Using this, the mass transfer problem has been solved for solute distribution in the liquid phase and the heat transfer problem has been solved to obtain the velocity of the solid-liquid interface, its location, and the freezing temperature of the interface. These mathematical solutions have been utilized to study the effect of various process parameters on the concentration of solute in an alloy.

It is found that the same composition of solute is obtained in the alloy for different cladding thicknesses by varying the laser power and the speed of the workpiece. This is because the initial pool mean temperature of the cladding material and hence the cooling rate are the same even though other parameters are different. Thus it can be concluded that the choice of the initial pool mean temperature determines the composition of the alloy. Since initial pool mean temperature is directly proportional to specific laser energy, when the initial temperature of the cladding melt is fixed or the specific laser energy is selected other process parameters can be determined by selecting any two of the three parameters, r_0 , v , and P and the third one will then have to be determined from Eq. (5). The composition of solute in the solid phase can be represented by a single curve for all possible values of the process parameters if it is plotted against the specific laser energy or the initial pool mean temperature. The effect of laser-cladding interaction time on solute concentration in the alloy and on the initial pool mean

temperature is found to be opposite to that of cladding thickness. Also, it has been found that if the equilibrium liquidus has a positive slope at the nominal composition of the cladding powder, then the nonequilibrium phase diagram has an enlarged solid-liquid region between the solidus and the liquidus compared to that of the equilibrium phase diagram.

ACKNOWLEDGMENT

This work was made possible by a grant (AFOSR:85-0333) from the U.S. Air Force Office of Scientific Research. Continued encouragement from the program managers Dr. A. Rosenstein and Major J. Hagar is also appreciated. The authors also like to acknowledge the help provided by Dr. S. Sircar for SEM data.

NOMENCLATURE

a	width of the substrate
b	width of the substrate and the cladding melt
B	Laser beam diameter
C	Concentration of solute in the liquid phase
C_l	Concentration of solute in the liquid phase at the solid-liquid interface
C_p	Average specific heat of the cladding material
C_s	Concentration of solute in the solid phase at the solid-liquid interface
C_l^*	Concentration (mole fraction) of solute in the liquid phase at the solid-liquid interface
\bar{D}	Average mass diffusivity of solute in the liquid phase
D^*	Interdiffusivity of solute at the interface
f	Fraction of laser energy absorbed by the cladding material
h_1	Heat transfer coefficient at the substrate boundary
h_2	Heat transfer coefficient at the cladding surface boundary
k_e	Equilibrium partition coefficient
k^*	Nonequilibrium partition coefficient
k_i	Thermal conductivity of the i -th region
L	Latent heat of fusion of the cladding material
m_l	Liquidus slope ($^{\circ}\text{K}/\text{mole fraction of solute}$)
P	Laser power
q	Rate of cladding powder delivery
r_c	Radius of the semi-cylindrical strip of cladding
s	Position of the solid-liquid interface
\bar{T}_2	Initial pool mean temperature

T_i	Temperature of the i-th region
T_I	Temperature at the solid-liquid interface
T_r	Ambient temperature
T_m^*	Intercept of liquidus line on temperature axis
v	Speed of the workpiece
v_0	Speed of sound in the cladding melt

Greek Symbols

α_i	Average thermal diffusivity in the i-th region
β	A non-dimensional parameter defined as $\dot{S}(t)\lambda/D^*$
λ	Interatomic distance
ρ	Average density of the cladding material

Subscripts

i	= 1 refers to the solid substrate
	= 2 refers to the solidified cladding
	= 3 refers to the liquid cladding

REFERENCES

1. Singh, J., and Mazumder, J., "Effect of Extended Solid Solution of Hf on the Microstructure of the Laser Clad Ni-Fe-Cr-Al-Hf Alloys," *Acta Metallurgica* (accepted for publication).
2. Mazumder, J., and Steen, W. M., "Heat Transfer Model for CW Laser Material Processing," *J. Appl. Phys.*, Vol. 51, 1980, pp. 941-947.
3. Cline, E., and Anthony, T. R., "Heat Treating and Melting Material with a Scanning Laser or Electron Beam," *J. Appl. Phys.*, Vol. 48, 1977, pp. 3895-3900.
4. Kou, S., Hsu, S. C., and Mehrabian, R., "Rapid Melting and Solidification of a Surface Due to a Moving Heat Flux," *Met. Trans. B.*, Vol. 12B, 1981, pp. 33-45.
5. Ashby, M. F., and Easterling, K. E., "The Transformation Hardening of Steel Surfaces by Laser Beams-I. Hypo-eutectoid Steels," *Acta Met.*, Vol. 32, 1984, pp. 1935-1948.
6. Chan, C., Mazumder, J., and Chen, M. M., "A Two-Dimensional Transient Model for Convection in Laser Melted Pool," *Met. Trans. A*, Vol. 15A, 1984, pp. 2175-2183.
7. Chande, T., and Mazumder, J., "Two-Dimensional, Transient Model for Mass Transport in Laser Surface Alloying," *J. Appl. Phys.*, Vol. 57, 1985, pp. 2226-2232.
8. Baker, J. C., and Cahn, J. W., "Thermodynamics of Solidification," in *Solidification*, ASM, Metals Park, OH, 1971, pp. 23-58.
9. Boettinger, W. J., and Perepezko, J. H., "Fundamentals of Rapid Solidification," *Proc., Rapidly Solidified Crystalline Alloys*, TMS-AIME, NJ, May 2-3, 1985.
10. Boettinger, W. J., Coriell, S. R., and Sekerka, R. F., "Mechanism of Microsegregation-free Solidification," *Mat. Sci., Eng.*, Vol. 65, 1984, pp. 27-36.
11. Kear, B. H., Giessen, B. C., and Ghen, M. (eds.), "Rapidly Solidified Amorphous and Crystalline Alloys," *Proc. MRS*, Vol. 8, Boston, MA, Nov. 1981.
12. Li, L. J., and Mazumder, J., "A Study of the Mechanism of Laser Cladding Processes," *Laser Processing of Materials* (eds., K. Mukherjee, and J. Mazumder), *Proc. Metal. Soc. AIME*, Los Angeles, CA, 1984, pp. 35-50.
13. Kar, A., and Mazumder, J., "One-Dimensional Diffusion Model for Extended Solid Solution in Laser Cladding," *J. Appl. Phys.* Vol. 61, No. 7, 1987, pp. 2645-2655.

14. Kar, A., and Mazumder, J., "One-Dimensional Finite-Medium Diffusion Model for Extended Solid Solution in Laser Cladding of Hf on Nickel," *Acta Metallurgica* (accepted).
15. Mullins, W. W., and Sekerka, R. F., "Stability of a Planar Interface During Solidification of a Dilute Binary Alloy," *J. Appl. Phys.*, Vol. 35, 1964, pp. 444-451.
16. Aziz, M. J., "Model for Solute Redistribution during Rapid Solidification," *J. Appl. Phys.*, Vol. 53, 1982, pp. 1158-1168.
17. Grinberg, G. A., "A Method of Approach to Problems of the Theory of Heat Conduction, Diffusion and the Wave Theory and Other Similar Problems in Presence of Moving Boundaries and its Applications to Other Problems," *J. Appl. Math. Mech.*, Vol. 31, No. 2, 1967, pp. 215-224.
18. Ozisik, M. N., and Guceri, S. I., "A Variable Eigenvalue Approach to the Solution of Phase-Change Problems," *Can. J. Chem. Eng.*, vol. 55, 1977, pp. 145-148.
19. Yener, Y., and Ozisik, M. N., "On the Solution of Unsteady Heat Conduction in Multi-Region Finite Media with Time-Dependent Heat Transfer Coefficient," *Proc., 5th Int. Heat Transfer Conf., Tokyo, Sept. 3-7, 1974*, Vol. I, pp. 188-192.
20. Incropera, F. P., and Dewitt, D. P., *Fundamentals of Heat and Mass Transfer*, 2nd. Ed., John Wiley and Sons, New York, 1985, p. 9.

NO-A191 274

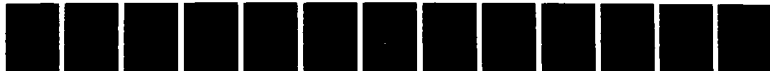
LASER CLADDING OF NI ND AND NG ALLOYS FOR IMPROVED
ENVIRONMENTAL RESISTAN. (U) ILLINOIS UNIV AT URBANA
LASER AIDED MATERIALS PROCESSING LAB. J MAZUNDER

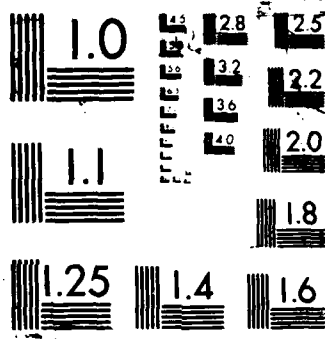
3/3

UNCLASSIFIED

OCT 87 AFOSR-TR-87-1856 AFOSR-85-8333

F/G 11/6.1 NL





The elements G_{jk} , $j = 1, \dots, 4$ and $k = 1, \dots, 4$ for the matrix $[G]$ are given by

$$G_{11} = -\sin A_2, G_{12} = -\cos A_2, G_{13} = G_{14} = 0$$

$$G_{21} = -\frac{a_2 k_2 \cos A_2}{k_1}, G_{22} = \frac{a_2 k_2 \sin A_2}{k_1}, G_{23} = G_{24} = 0$$

$$G_{31} = \sin S_2, G_{32} = \cos S_2, G_{33} = -\sin S_3, G_{34} = -\cos S_3$$

$$G_{41} = G_{42} = 0, G_{43} = -a_3 \cos B_3 - \frac{h_3 \sin B_3}{\lambda k_3}, G_{44} = a_3 \sin B_3 - \frac{h_3 \cos B_3}{\lambda k_3}$$

The four elements of the column vector H are

$$H_1 = E_2, H_2 = F_2, H_3 = E_3, H_4 = F_3$$

and the elements of the column vector N are

$$N_1 = -\cos A_1 - \frac{h_1 \sin A_1}{a_1 \lambda k_1}$$

$$N_2 = a_1 \sin A_1 - \frac{h_1 \cos A_1}{\lambda k_1}$$

$$N_3 = N_4 = 0$$

LIST OF FIGURES

- Figure 1(a) Schematic diagram of laser surface cladding
(b) Three-dimensional view of the cladding and the substrate
(c) Geometric configuration used in the present model.
The model substrate and the solidification of the model cladding have been shown after rotating the pool ABCA (see Fig. 1a) by 90° clockwise
- Figure 2 Concentration of aluminum in the extended solid solution of nickel-aluminum versus cladding thickness per unit laser beam diameter
- Figure 3 Initial pool mean temperature of nickel-aluminum versus cladding thickness per unit laser beam diameter
- Figure 4 Initial pool mean temperature of nickel-aluminum versus cladding powder feed rate
- Figure 5 Concentration of aluminum in the extended solid solution of nickel-aluminum versus cladding powder feed rate
- Figure 6 Concentration of aluminum in the extended solid solution of nickel-aluminum versus specific laser energy
- Figure 7 Initial pool mean temperature of nickel-aluminum versus specific laser energy

Figure 8 Concentration of aluminum in the extended solid solution of nickel-aluminum versus initial pool mean temperature

Figure 9 Concentration of aluminum in the extended solid solution of nickel-aluminum versus laser-cladding interaction time

Figure 10 Initial pool mean temperature of nickel-aluminum versus laser-cladding interaction time

Figure 11 Variation of the temperature at the solid-liquid interface with the concentration of aluminum in nickel-aluminum alloy

Figure 12 Comparison of nonequilibrium phase diagram of the extended solid solution of nickel-aluminum with its equilibrium phase diagram

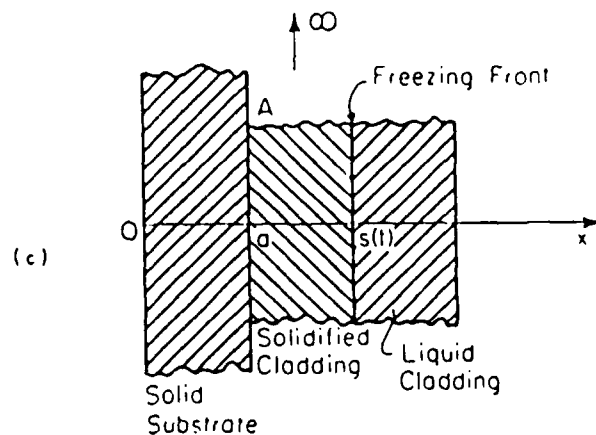
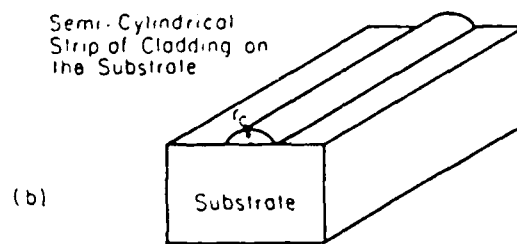
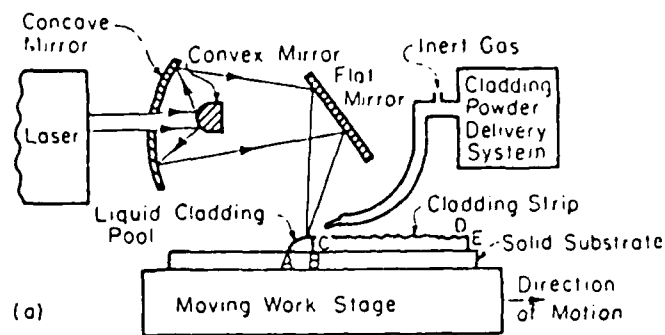


Figure 1(a) Schematic diagram of laser surface cladding
 (b) Three-dimensional view of the cladding and the substrate
 (c) Geometric configuration used in the present model.
 The model substrate and the solidification of the model cladding have been shown after rotating the pool ABCA (see Fig. 1a) by 90° clockwise

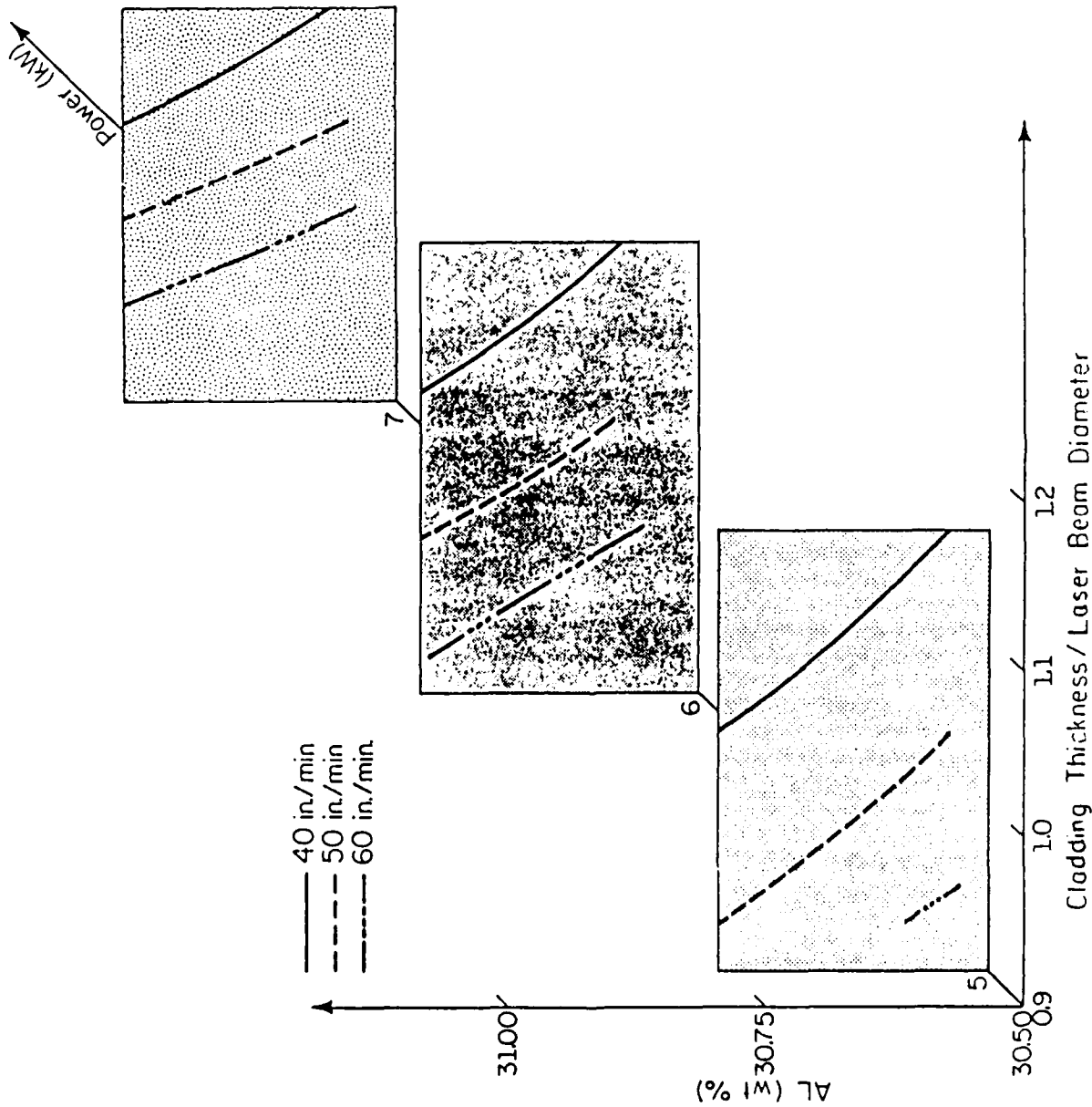


Figure 2 Concentration of aluminum in the extended solid solution of nickel-aluminum versus cladding thickness per unit laser beam diameter

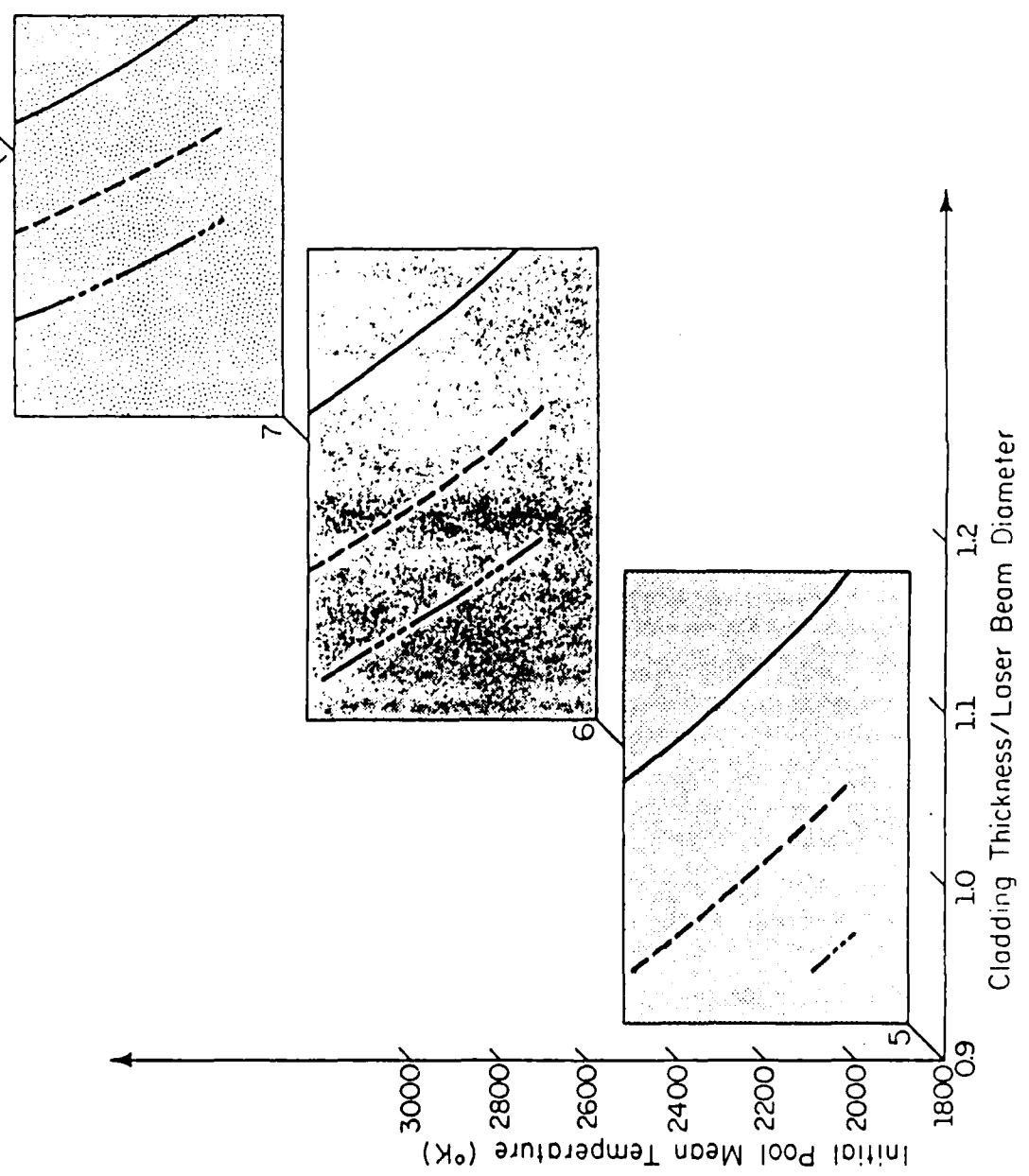


Figure 3 Initial pool mean temperature of nickel-aluminum versus cladding thickness per unit laser beam diameter

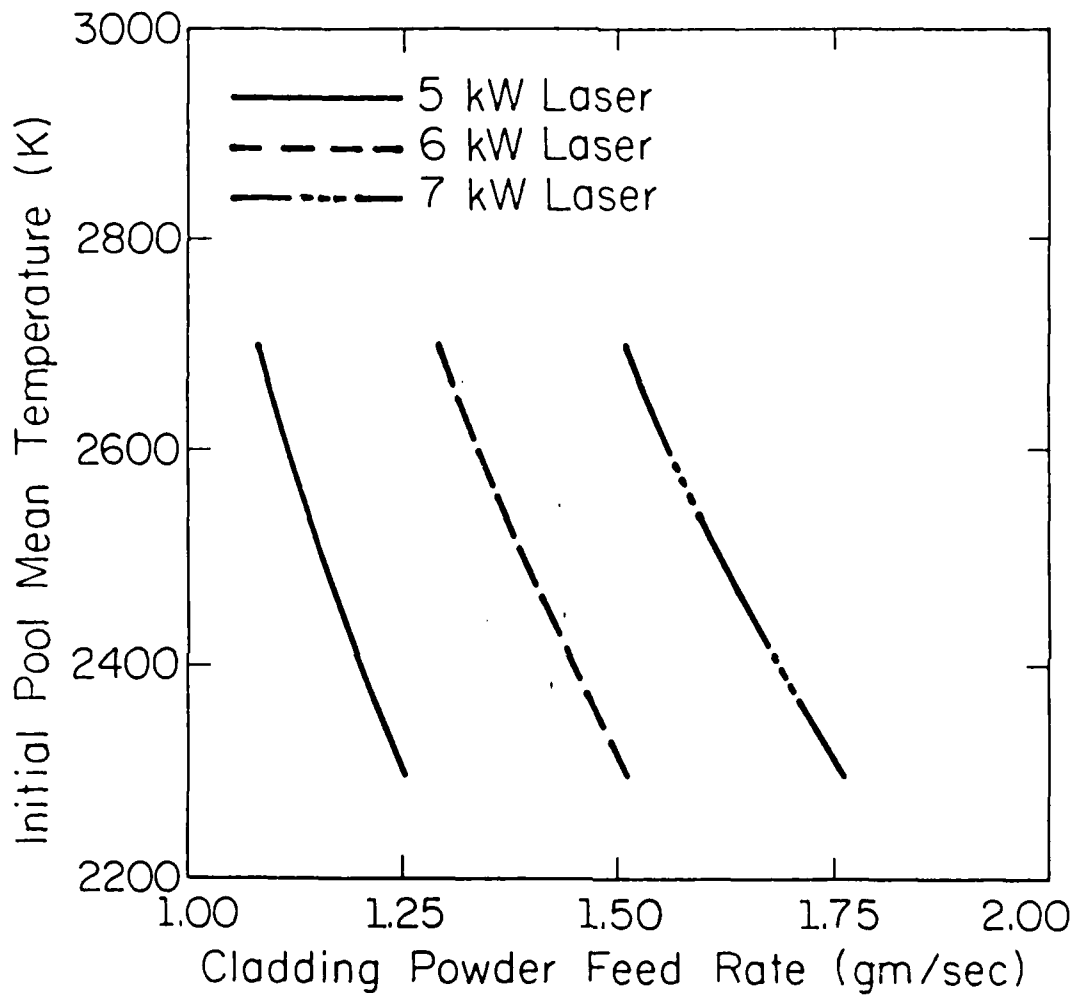


Figure 4 Initial pool mean temperature of nickel-aluminum versus cladding powder feed rate

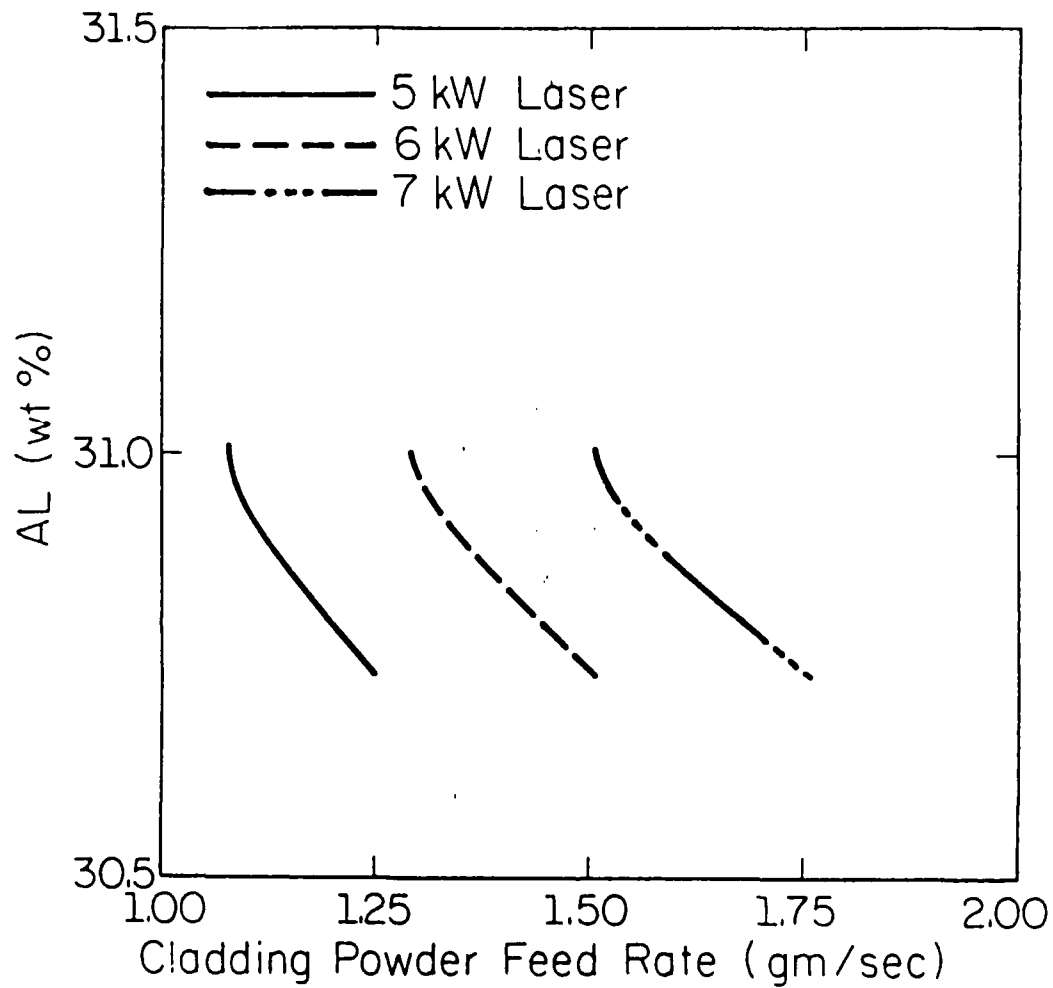


Figure 5 Concentration of aluminum in the extended solid solution of nickel-aluminum versus cladding powder feed rate

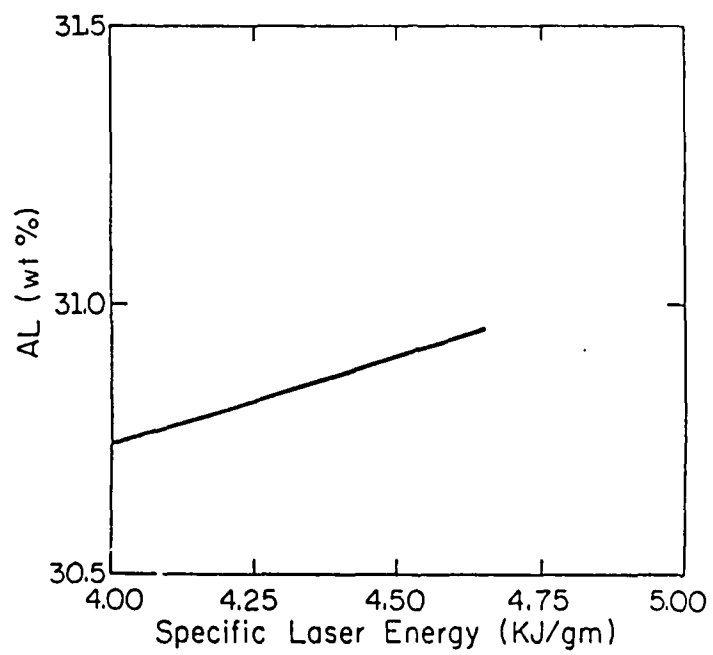


Figure 6 Concentration of aluminum in the extended solid solution of nickel-aluminum versus specific laser energy

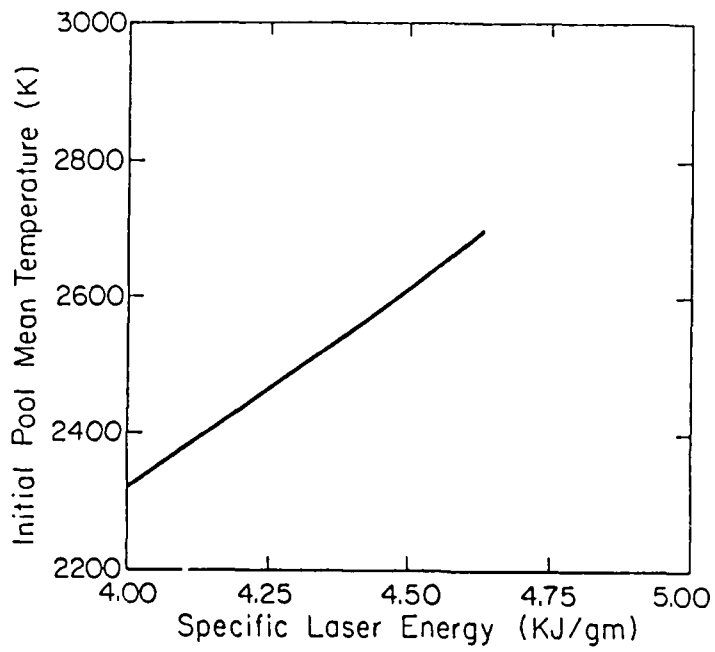


Figure 7 Initial pool mean temperature of nickel-aluminum versus specific laser energy

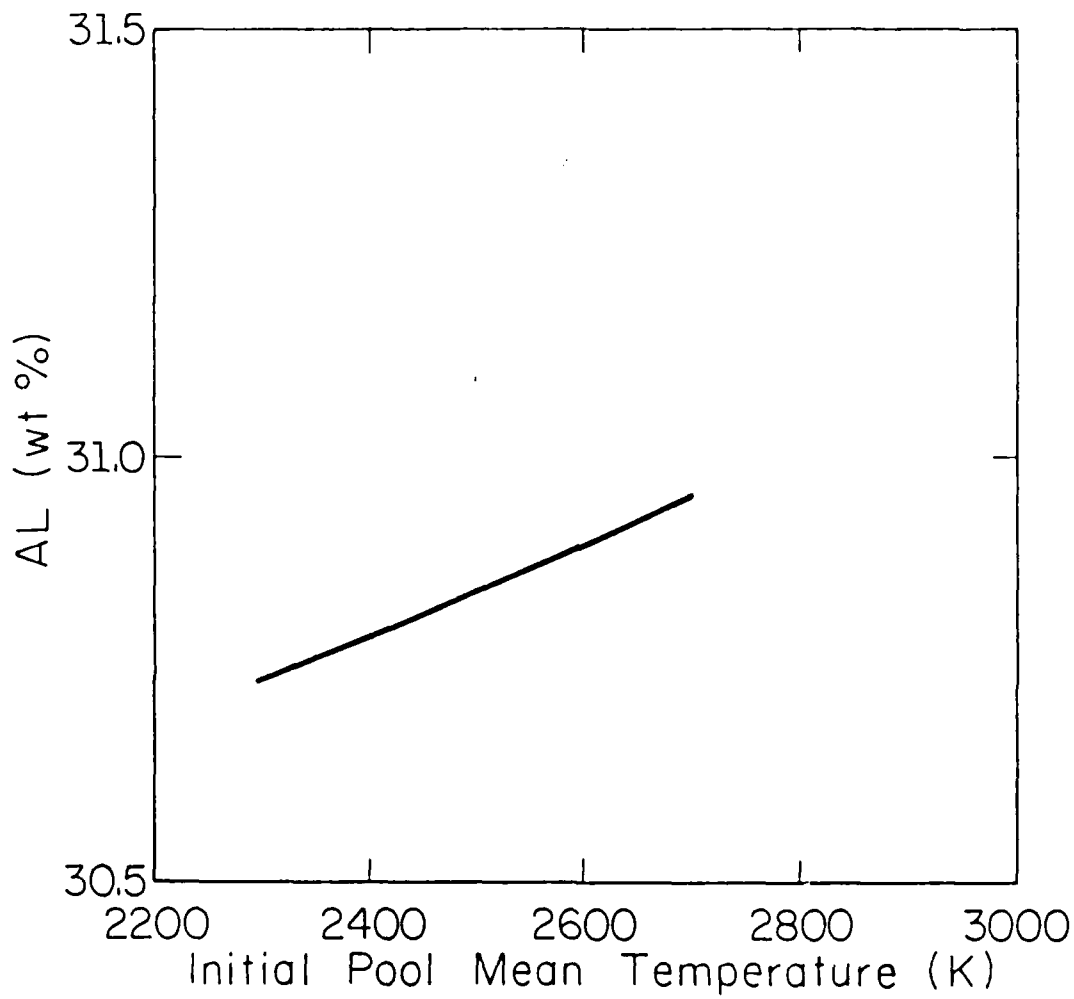


Figure 8 Concentration of aluminum in the extended solid solution of nickel-aluminum versus initial pool mean temperature

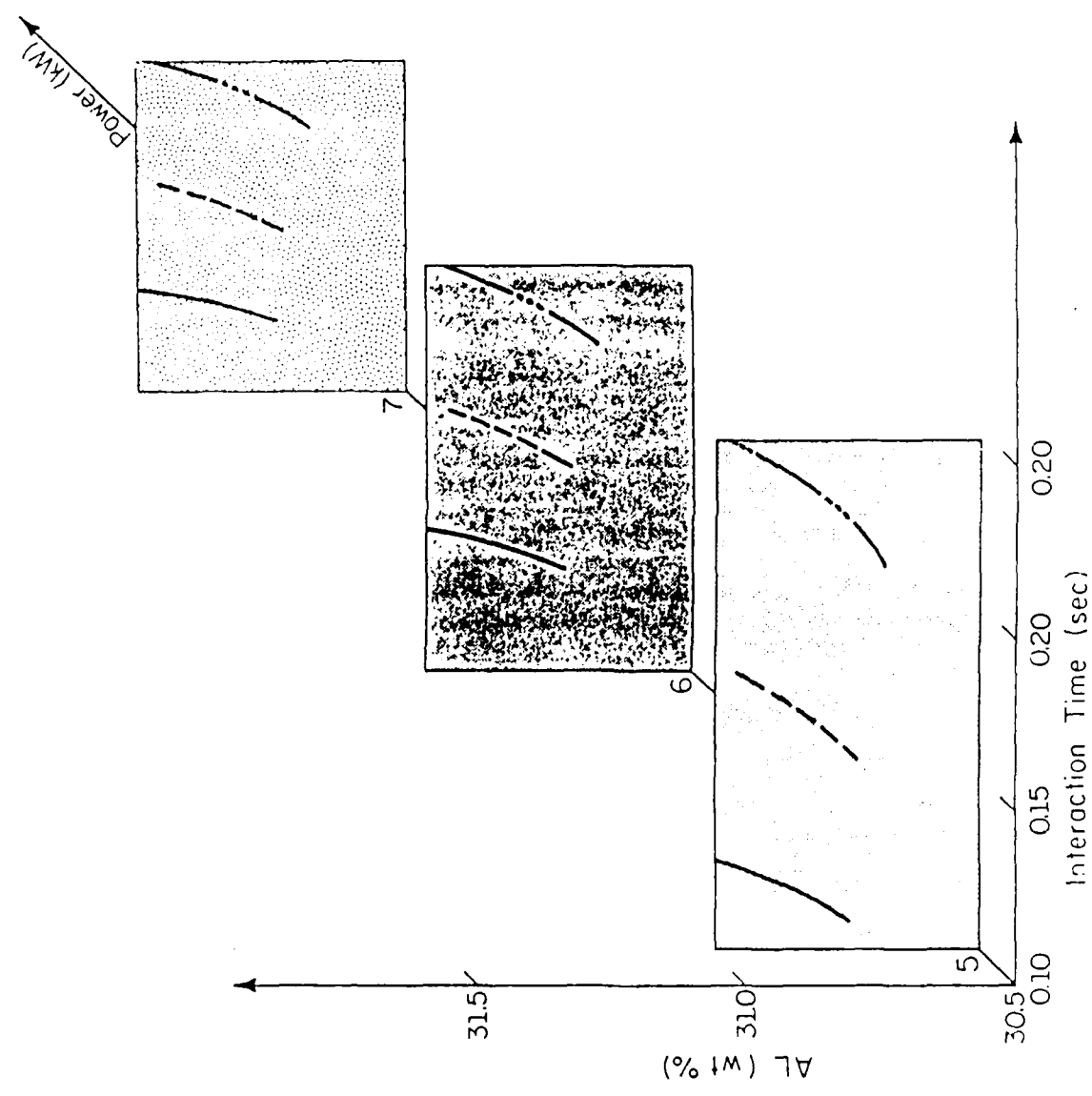


Figure 9 Concentration of aluminum in the extended solid solution of nickel-aluminum versus laser-cladding interaction time

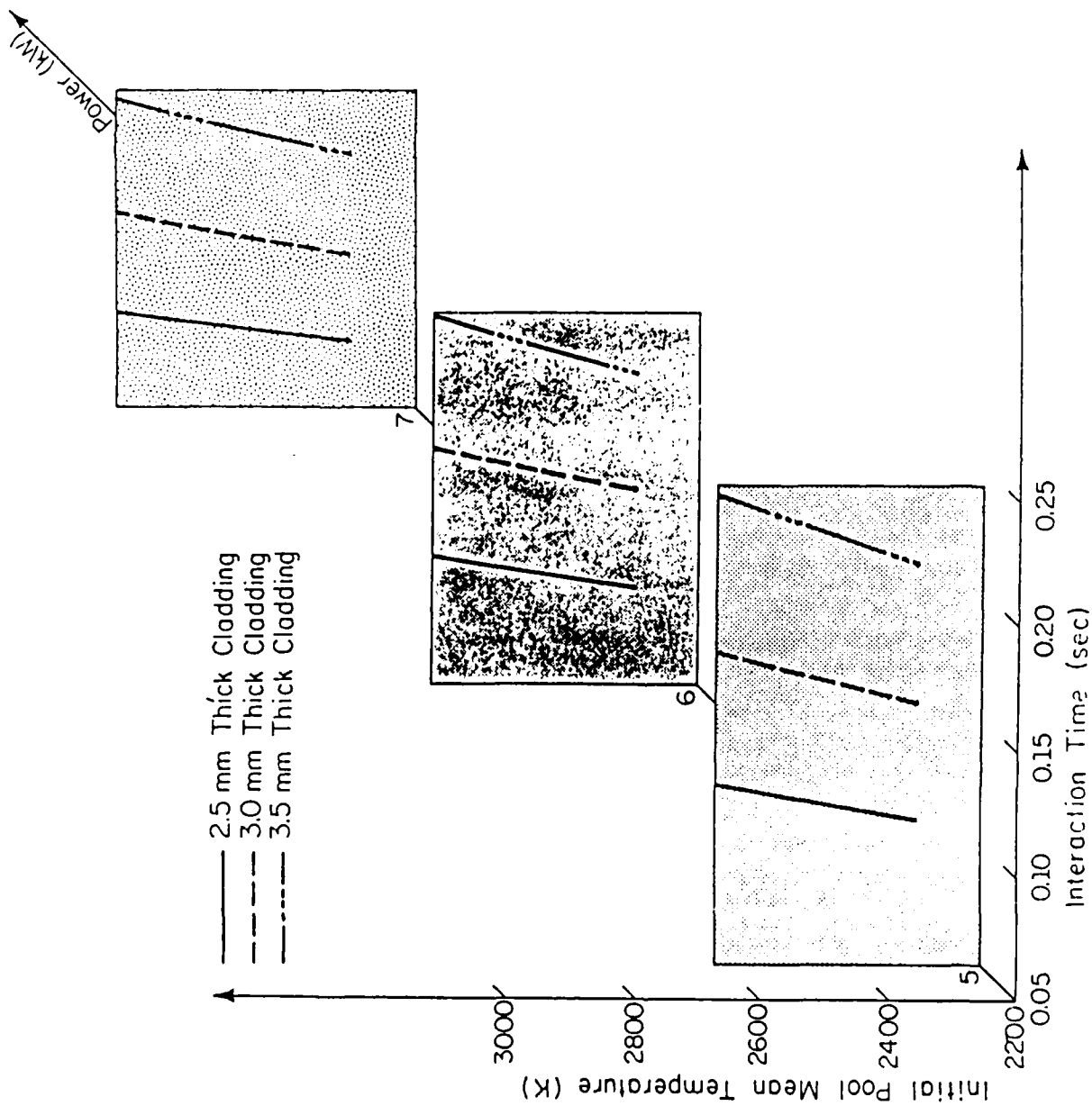


Figure 10 Initial pool mean temperature of nickel-aluminum versus laser-cladding interaction time

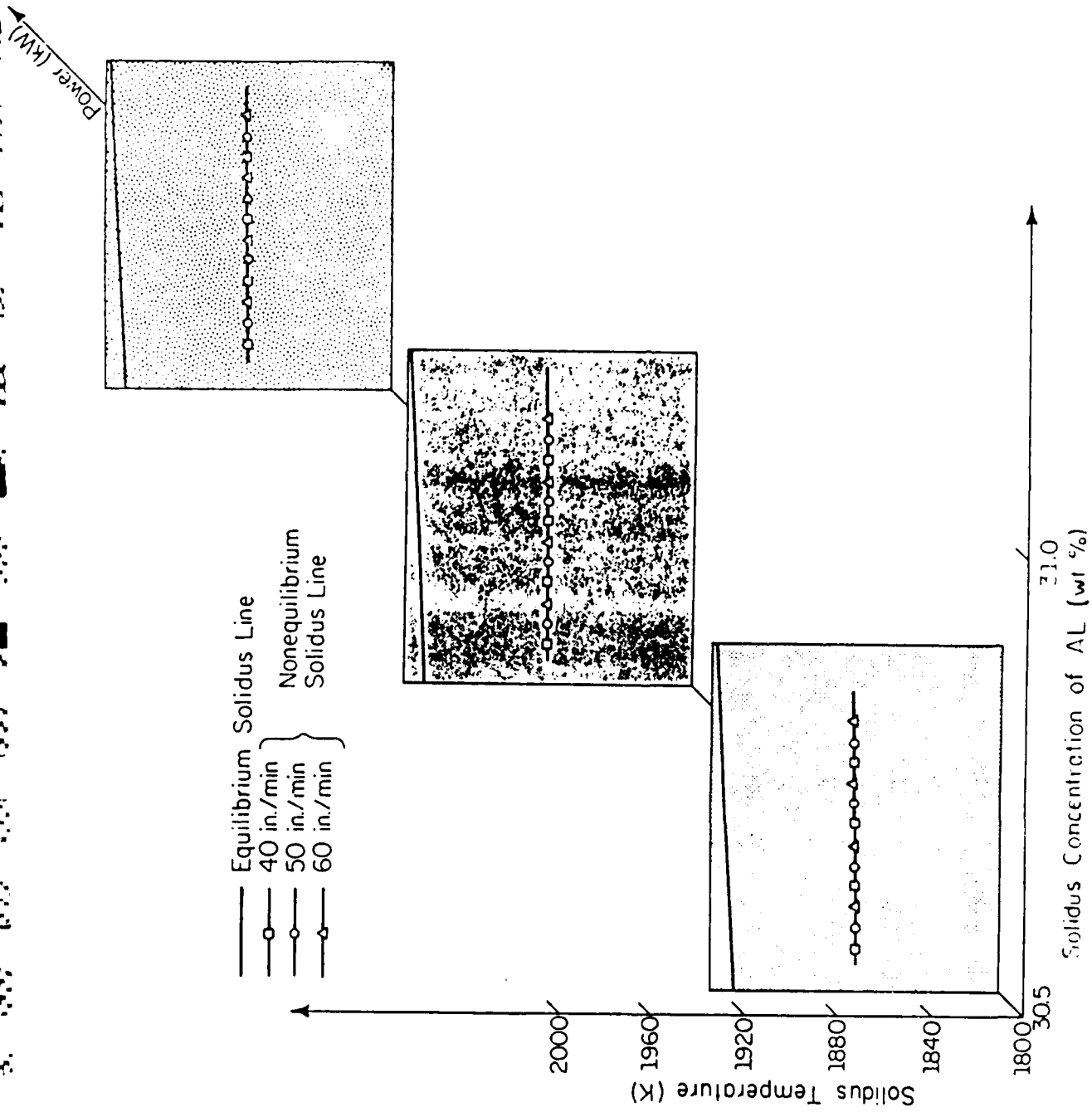


Figure 11 Variation of the temperature at the solid-liquid interface with the concentration of aluminum in nickel-aluminum alloy

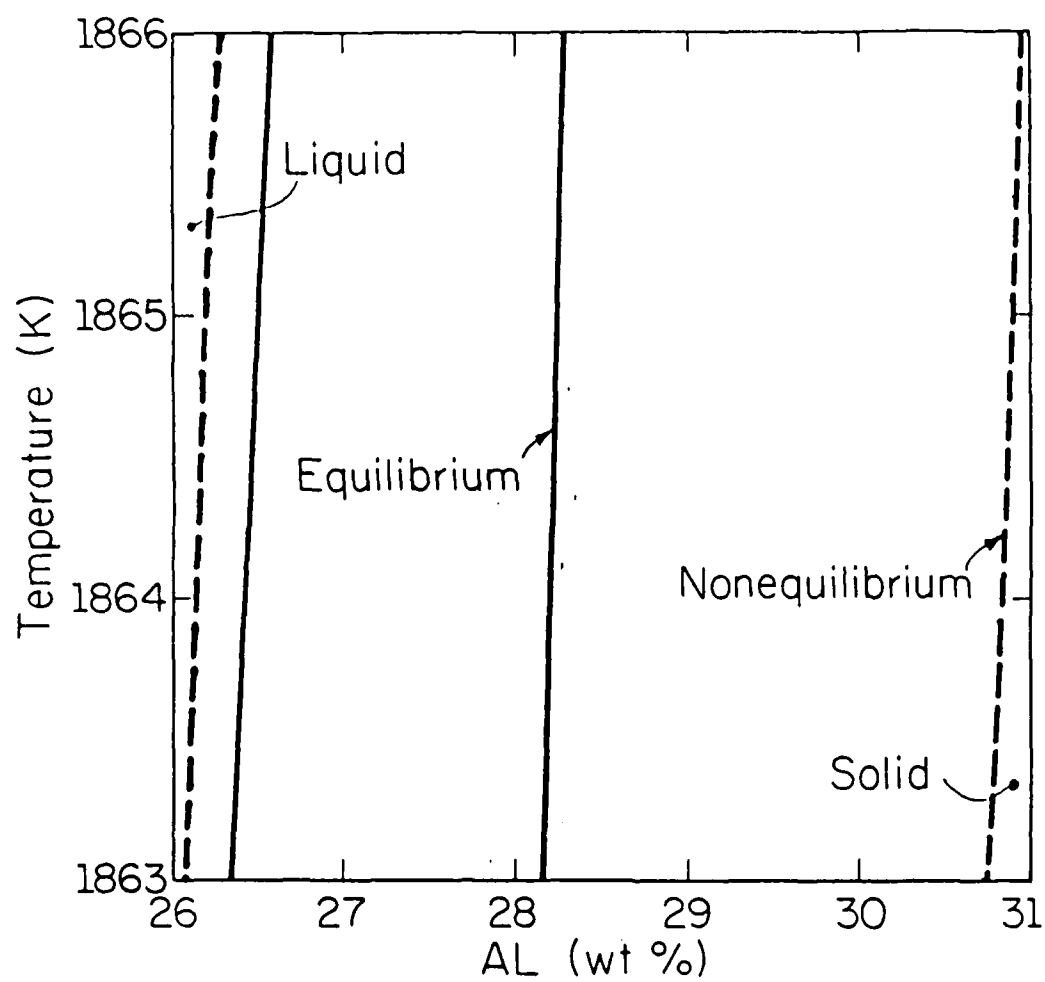


Figure 12 Comparison of nonequilibrium phase diagram of the extended solid solution of nickel-aluminum with its equilibrium phase diagram

END
DATE
FILMED
5-88
DTIC